

**GEOFORSCHUNGSZENTRUM POTSDAM**  
STIFTUNG DES ÖFFENTLICHEN RECHTS

---

# Scientific Technical Report

ISSN 1610-0956

# ANGEL

## Airborne Navigation and Gravimetry Ensemble & Laboratory Introduction and First Airborne Tests

**U. Meyer<sup>1</sup>, G. Boedecker<sup>2</sup>, H. Pflug<sup>1</sup>**

<sup>1</sup> GeoForschungsZentrum Potsdam (GFZ)  
Department 1 „Geodesy and Remote Sensing“  
Section 1.3 ”Gravity Field and Earth Models”  
D-14473 Potsdam, Telegrafenberg A17, Germany  
umeyer@gfz-potsdam.de, pflug@gfz-potsdam.de

<sup>2</sup> Bayerische Akademie der Wissenschaften (BADW)  
Bayerische Kommission für die Internationale Erdmessung (BEK)  
D-80539 München, Marstallplatz 8, Germany  
boe@bek.badw-muenchen.de

**Summary:** The LaCoste & Romberg gravity meter S124b and its associated system environment were installed and tested in conjunction with a strap-down gravity meter system (SAGS) of the Bayerische Akademie der Wissenschaften in Munich on a Cessna Grand Caravan of the DLR in Oberpfaffenhofen. This report describes the design and instrumentation of the aerogravimetry system, it documents the installation on the aircraft and it discusses some of the results of the test flights performed within AGFA (Airborne Gravity Flight Approach).

Beyond the documentation of the system this report gives a short introduction to the basics of the instruments including a short theory of their operation and data processing. The intention is to give readers from disciplines other than aero-gravimetry and aero-altimetry a technical insight into how the system works and what it is capable of. This should help the reader to evaluate the systems usefulness in other geo-scientific projects. The experiences from the test flights are briefly summarized and an update of the current status and future plans for the individual instruments is given.

The aerogravimetry system consists of two major instrument blocks: the gravimetry sensing system and the positioning system. The gravimetry sensors are the LaCoste & Romberg S124b and the SAGS-2.2 systems. The navigation block holds GPS receivers, an inertial navigation system and a laser altimeter.

The aircraft used for the primary tests was a Cessna Grand Caravan of the DLR in Oberpfaffenhofen. It offers superb conditions for scientific installations and is widely used in geophysical exploration all over the world.

The test flights were flown from Oberpfaffenhofen airport. One profile covers the Bavarian Alps to map short wavelength, topography induced gravity disturbances, and another flight crosses the Rhine Graben to map long wavelength structures of the deeper crust.

The software for data processing for navigation, gravimetry and geoid calculations is briefly summarized.

## Contents

<b>1</b>	<b>Introduction</b>	<b>3</b>
<b>2</b>	<b>The aerogravimetry system: ANGEL</b>	<b>4</b>
2.1	Angel: A general overview	4
2.2	Airborne gravimetry	4
2.3	Airborne altimetry	5
<b>3</b>	<b>LaCoste &amp; Romberg S124b gravity meter</b>	<b>6</b>
3.1	Theory of operation	7
3.1.1	Summarized practical theory of operation	7
3.1.2	Brief mathematical theory of operation	9
3.2	Platform controller	18
3.3	Fiber optic gyros	18
<b>4</b>	<b>Navigation equipment</b>	<b>20</b>
4.1	IGI inertial navigation system	20
4.1.1	Theory of operation	20
4.1.2	Technical specifications	21
4.2	GPS receivers	21
4.2.1	Theory of operation	22
4.2.2	Deriving accelerations from GPS	28
4.3	Laser altimeter	29
4.3.1	Theory of operation	29
<b>5</b>	<b>Central timing</b>	<b>31</b>
5.1	Theory of operation	31
<b>6</b>	<b>Strap-down gravimetry system SAGS-2.2</b>	<b>32</b>
6.1	Theory of operation	32
6.1.1	Introduction	32
6.1.2	Accelerometer triad calibration	32
6.1.3	Attitude alignment and calibration	33
6.2	Technical description	37
6.2.1	Introduction	37
6.2.2	Q-Flex accelerometer technique	37
6.2.3	Temperature and other effects on SAGS	38
6.2.4	Sensor configuration	39
6.2.5	Vibration damping	39
6.2.6	Signal processing	39
<b>7</b>	<b>The aircraft: DLR Cessna Grand Caravan</b>	<b>40</b>
7.1	General description	40
7.2	Special DLR modifications	40
<b>8</b>	<b>The software: GPS, aerogravimetry and geoid</b>	<b>41</b>
8.1	Kinematic DGPS-software	41
8.1.1	Kinematic GPS software for AGFA	41
8.1.2	Kinematic GPS software for ANGEL	41
8.2	Aerogravimetry software	42
8.2.1	General overview	42
8.2.2	Synchronization of time series	43
8.2.3	Eötvös correction	43
8.2.4	Vertical accelerations	44
8.3	Geoid modeling software	44
<b>9</b>	<b>The test flights: First results</b>	<b>45</b>
9.1	Introduction	45
9.2	Ground truth data: southern Bavaria and German Alps	46
9.3	Airborne data: Bavarian Alps	48
9.4	Ground truth data: Rhine Graben	50
9.5	Airborne data: Rhine Graben	52
<b>10</b>	<b>Conclusions</b>	<b>54</b>
10.1	Hardware	54
10.2	Software	54
10.3	SAGS	54
<b>11</b>	<b>Technical specifications of the instruments</b>	<b>55</b>
11.1	LaCoste & Romberg S124b	55
11.2	IGI Inertial Navigation System	58
11.3	Ashtech Z-Surveyor GPS receiver	59
11.4	Trimble 4000 SSE GPS receiver	62
11.5	Novatel OEM4 GPS receiver	63
11.6	Riegl laser altimeter	64
11.7	Meinberg clock and central trigger	67
11.8	SAGS 2.2	68
11.9	DLR Cessna Grand Caravan	70
<b>11</b>	<b>References</b>	<b>73</b>
<b>12</b>	<b>Acknowledgements</b>	<b>74</b>

# 1 Introduction

In late 1999, the GFZ purchased a new gravity meter system for marine and airborne applications from LaCoste & Romberg Inc. This instrument is the nucleus of an airborne gravimetry and altimetry system managed and developed by the GFZ Potsdam, with contributions from the Bayerische Akademie der Wissenschaften. After some laboratory work on the new gravimeter in Potsdam a small survey named AGFA (Airborne Gravity Flight Approach) was planned to test the sensor in an airborne environment.

Two test areas were chosen for the project. The first is the Bavarian Alps where short wavelength anomalies are generated to a high degree by topographic effects. The second area is the Rhine Graben. Initially, it was planned to cross the Rhine Graben south of Strasbourg and Freiburg. Unfortunately, due to a cluster of restricted flight areas in France, this was not possible. Alternatively, two profiles crossing the Rhine around Karlsruhe were chosen.

The installation was prepared well ahead of the actual survey. All necessary documentation had to be presented for pre-checks to get temporary permission to fly the aerogravimetry equipment on a Cessna Grand Caravan of the DLR Oberpfaffenhofen.

The installation went smoothly. The aircraft technicians of the DLR Oberpfaffenhofen offered help whenever needed. Due to the late technical flight permit and the limited weather windows for the gravimetry flight operation, only two survey flights could be performed. The flight conditions during both operations were calm to modestly windy. The aircraft was flown by autopilot to ensure a minimum of aircraft disturbances. The course was computed from GPS, the altitude from barometric sensors. The autopilot system has a regular sinusoidal shaped correction pattern to control the aircraft. This has a more or less stable frequency content that does not conflict with the gravimetry measurements.

The main instrument was a LaCoste & Romberg gravity meter. It was installed underneath the wings, as close to the center of gravity of the aircraft as possible. Two GPS antennae were installed on top of the aircraft cabin. A strap-down airborne gravimetry system developed by Dr.-Ing. Gerd Boedecker of the Bayerische Akademie der Wissenschaften in Munich was installed parallel to the LaCoste & Romberg sensor together with an IGI<sup>®</sup> inertial navigation system. For some tests over lakes and rivers, a laser altimeter from Riegl<sup>®</sup>, Austria, was also installed.

The software used to calculate free-air gravity profiles from the flights was KSG-Soft, GeoGenius<sup>®</sup> and later Trimble Total Control<sup>®</sup> for kinematic DGPS and AGS-124 for gravity filtering and reduction. AGS-124 was derived from the AGP-software (aero-gravity processing) developed by Arne Olesen from the KMS in Copenhagen. The version used was especially adapted to fit the GFZ operating environment.

For quality control and data storage two personal computers were set-up at DLR Oberpfaffenhofen. Now, these computers are replaced by laptops.

The test flights were not only important to prove the instruments were working properly in the air and to get the flight certification, but also as a test for the application of the system over the Chicxulub crater in Mexico.

The following pages introduce the concept of the aerogravimetry system, the basics of how the individual instruments work, plus the results and experiences of the field work.

## 2 The aerogravimetry system ANGEL

### 2.1 ANGEL: A general overview

ANGEL is an acronym for “Airborne Navigation and Gravimetry Ensemble & Laboratory”. It represents an airborne gravimetry and altimetry system that is constantly being updated by either upgrades to the existent equipment and software or by integrating new sensors. New combinations of the equipment are tested on different carriers, either to map geologic features, or to experiment with navigation data, new sensing systems and alternative platforms.

### 2.2 Airborne gravimetry

Gravimetry measurements on a moving platform respond to two major effects: the motion of the aircraft and the mass attraction of the Earth. The effect of the aircraft’s motion can be split into the aircraft’s acceleration and its movement against the centrifugal force due to the Earth’s rotation. In general, all three effects are represented in dimensions of acceleration. When the Earth’s gravity field is measured from an aircraft, the aircraft’s acceleration and vibration due to it’s kinematics and the response of its physical structure is much larger than the changes in the gravity field. Special devices such as air-dampers and elastic cords are used to damp the vibration. The aircrafts kinematics must be determined by a system that is unaffected by the Earths attraction and rotation (it must be non-inertial). This is realized by GPS measurements that give the position of the aircraft in space for an exact moment of time. All these positions merged in a time series make it possible to calculate the course, the speed and the acceleration of the aircraft in three dimensions. The gravimetry sensor on board the aircraft measures the total of all accelerations including those of the aircraft (Fig.2.1.1).

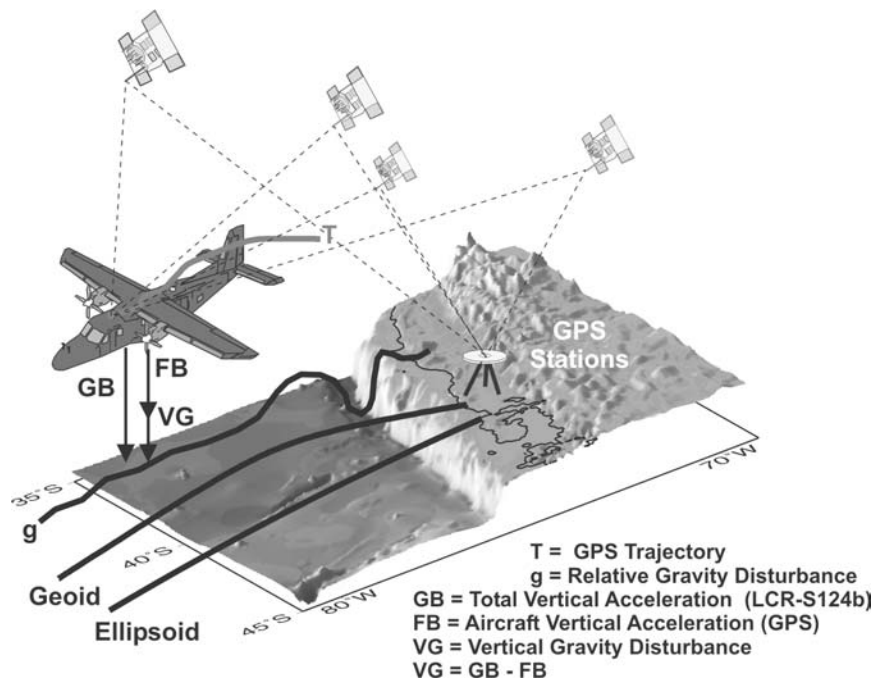


Figure 2.1.1: Airborne gravimetry

herefore, the second derivative of the height over a given ellipsoid is computed and used for reduction. Alternatively, a high resolution and high precision barometric sensor can be used to determine the aircrafts vertical acceleration. When the aircraft’s vertical acceleration is

subtracted from the gravity meter readings, only the effects of the centrifugal forces and the mass attraction will remain. The aircrafts speed and direction against the rotation of the Earth results in the Eötvös effect. This effect adds or subtracts a significant acceleration value to the gravity meter observations depending on course and velocity. When this effect is corrected for, only the contribution of the mass attraction remains. This resulting measurement is the gravity disturbance at the flight level. When the disturbances at the observation level are downward continued to the mean sea surface (or the geoid), the result is a free-air gravity anomaly profile. Valuable details about the definition of the gravity anomaly are given in Hackney and Featherstone [2003].

### 2.3 Airborne altimetry

If an airborne gravimetry system is available, it is relatively easy to upgrade it to an airborne altimetry system for monitoring water surfaces. All that is additionally needed is precise control of the aircrafts attitude and an altimeter system. In our case, the inertial navigation system is already part of the gravimetry equipment and supplies all attitude data at high rate. For high precision, low altitude range altimetry, a laser altimeter system is available. From the airborne gravity data a regional geoid can be determined or an existing one can be significantly improved. The aircraft’s position is measured with respect to a given ellipsoid. When the laser beam is corrected for the deviations from the vertical induced by the aircrafts movements, it gives the height of the aircraft above the sea level (Fig. 2.2.1). If the geoid undulation is related to the same ellipsoid and the water surface were undisturbed by waves and tides, then the geoid surface and water surface should be approximately the same. So when the geoid surface is subtracted from the water surface, only the “sea surface topography” remains. This topography is mainly caused by current systems. Information about the sea surface topography is a highly valuable input for oceanographic modeling and essential for reduction of satellite altimetry derived gravity.

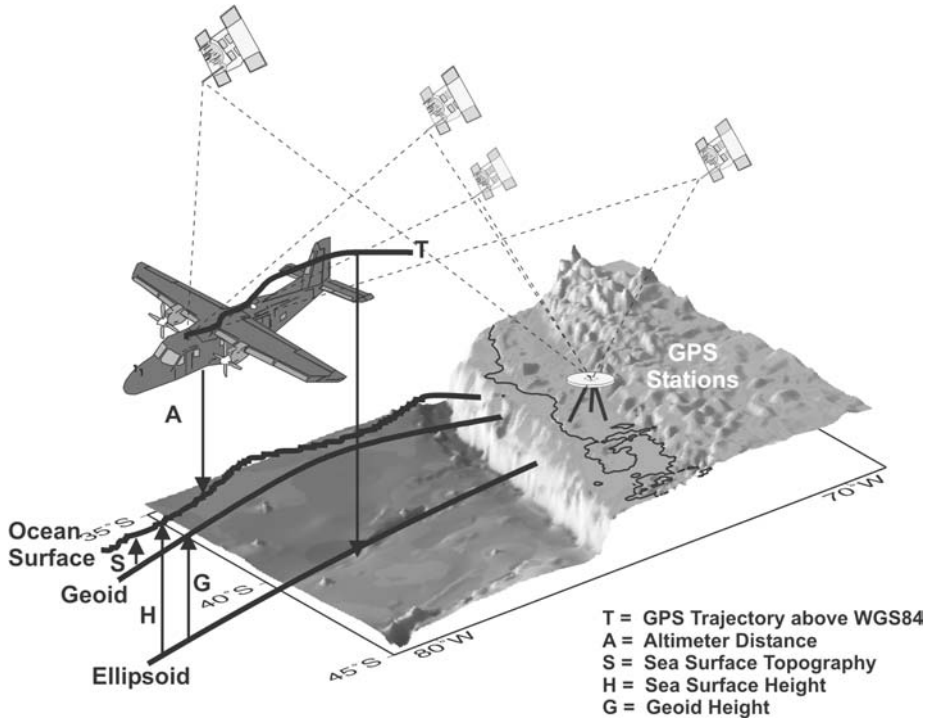


Figure 2.2.1: Airborne altimetry

### 3 LaCoste & Romberg S124b gravity meter

The LaCoste & Romberg S124b gravity meter (see Fig. 3.1) showed a good overall performance before, during and after all AGFA (Airborne Gravity Flight Approaches) test flights. It dumped twice when the lower rubber cords loosened and the platform experienced a large tilt angle. This problem was soon solved. All rubber strings will be checked annually and replaced if necessary. An installation problem was the housing of the exterior computer and control units mounted in an extra rack. Both units are now integrated in a newly designed housing, saving space and weight and being much safer and easier to install. After one dump some data were lost because of a wrong re-initialization of the system. This problem is due to the LaCoste & Romberg software that controls the hardware. Unfortunately, this apparent bug still exists. In the future, we plan to integrate an absolute decoder to ensure that the spring tension is read without slips. Moreover, better temperature control of the sensor within the data stream is desirable.

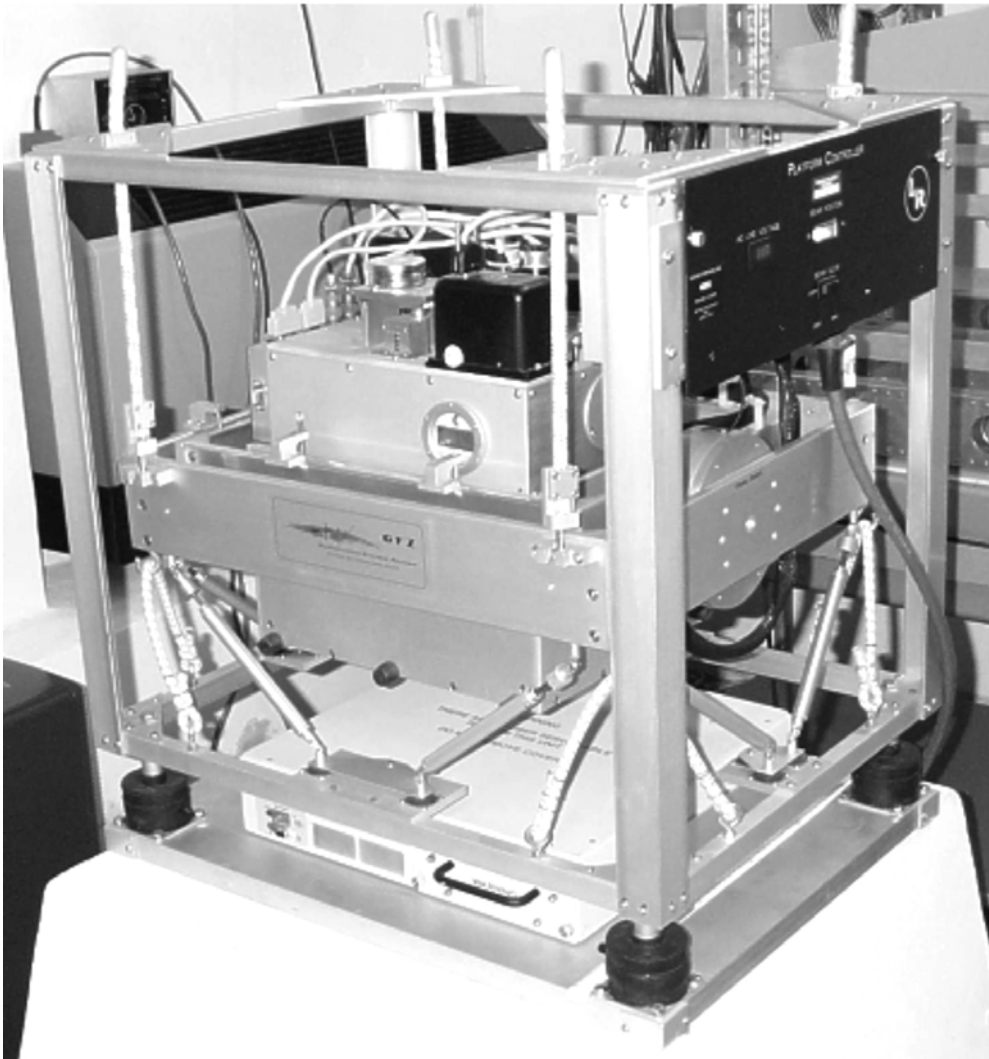
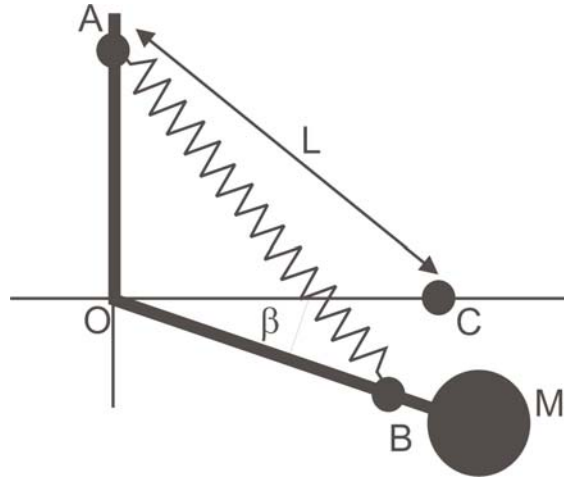


Figure 3.1: LaCoste & Romberg airborne gravity meter S124b

### 3.1 Theory of operation

The LaCoste & Romberg air/sea gravity meter Model S124b consists of a highly damped, spring-type gravity sensor mounted on a gyro-stabilized platform with associated electronics. The original theory behind the LaCoste & Romberg Air/Sea gravity meter is given in LaCoste [1967].



**Figure 3.1.1:** Simplified principle of a zero-length suspension system: The mass  $M$  is attached to the moveable beam  $OB$  that is free to rotate about  $O$ . The beam is supported by a zero-length spring attached at the points  $A$  and  $B$ . Point  $A$  can be vertically adjusted to drive the beam back towards the horizontal. In practice, the total travel distance of the beam between the top stop and the bottom stop is about a couple of millimeters in the Model S meter. Point  $C$  marks the position of  $B$  the in case of equilibrium.  $L$  then would then describe the “zero-length” spring.

#### 3.1.1 Summarized practical theory of operation

The Model S sensor incorporates a hinged beam and test mass supported by a spring (see Fig. 3.1.1). For later use, we define the spring tension  $ST = k_{ST}(L - L_0)$  with  $(L - L_0)$  being the spring elongation and  $k_{ST}$  being an instrument constant. Valliant [1992] has shown that the restoring moment for such a spring system tuned to infinite periods is (ignoring damping and  $\beta$  being the distortion angle in Fig. 3.1.1):

$$M_{restore} = \frac{k_{ST}L_0}{\sqrt{2}} \left( \frac{1}{2}\beta - \frac{3}{8}\beta^3 + \dots \right) \quad (3.1.0)$$

For  $L_0 = 0$  the system exerts no restoring moment. Thus, the system is in a state of neutral equilibrium (infinite period). The condition  $L_0 = 0$  implies that the spring's elongation equals its length. In other words, the spring behaves as if its unstretched length would be zero. It is therefore called a “zero-length” spring. This “zero-length spring” principle has been applied to almost all of the gravity meters manufactured by LaCoste & Romberg.

The damping of the large vertical accelerations due to the aircraft's motion is achieved by the use of two air dampers (see Fig. 3.1.2). Nevertheless, the vertical accelerations of the aircraft make it impossible to keep the beam constantly nulled. Therefore, it is necessary to read the gravity sensor when the beam is in motion. A mathematical analysis of the spring-type gravity sensor shows that this is possible through observations of the beam position, the beam velocity and the beam acceleration at any given time. If the beam motion is highly damped, the beam acceleration term can also be neglected. If the gravity sensor has a very

high sensitivity over a high range, the beam position can be neglected as well. The LaCoste & Romberg S-meter fulfils both of the requirements (mainly because in a simplified explanation, any constant exterior acceleration is translated to a constant beam velocity by suitable damping). Accordingly, it can be read without nulling via the measurement of the beam position parallel to the adjusted spring tension. Utilizing the zero-length spring principle in a particular geometry results in a vertical suspension that can have infinite periods [LaCoste et al., 1988]. When the period is infinite and the torque exerted by the spring tension exactly balances the torque exerted by gravity, the beam will remain stationary at any position. When this position is achieved, the smallest change in gravity will cause the beam to rotate to one stop or the other. Thus, infinite period corresponds to infinite sensitivity [Valliant et al., 1992]. If the period is less than infinite and the beam is displaced from its equilibrium position, a restoring torque will return it back to the equilibrium position – this is the case for land gravity meters (see Fig. 3.1.3).

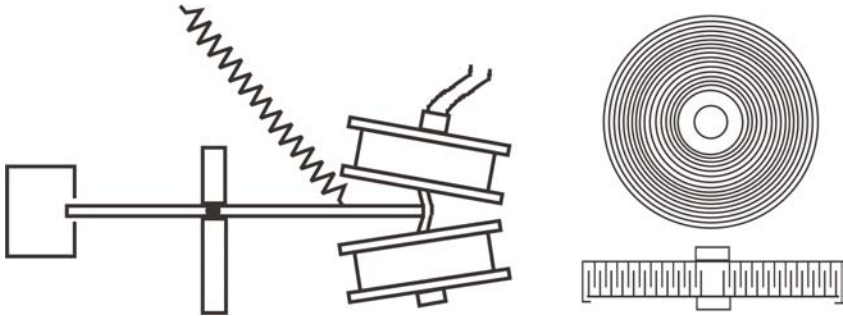


**Figure 3.1.2:** Schematic sketch on beam damping (right end of beam with hose for air pump) and box for capacitive beam position measurement (left end of beam) plus top and side cut view of an air damper.

So finally, for the Model S meter the basic equation to gain the relative gravity at a given time and thus at a given location is:

$$g_{Meter} = SM = S(SpringTension + kBeamVelocity + CrossCouplingCorrection) . \quad (3.1.1)$$

Here,  $k$  is assumed a constant depending on the adjustment of the physical damping which is mainly dependent on the quality of the air dampers implemented in the system (see Fig. 3.1.3).  $M$  is the actual measurement in scale units;  $S$  is the scale factor to convert the readings into mGal. In our case  $g_{Meter}$  only represents a relative measurement, meaning that changes in the gravity field are detected.

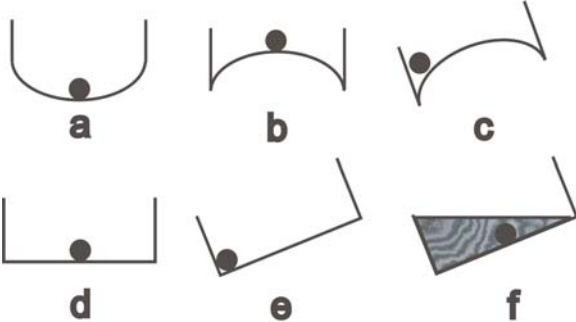


**Figure 3.1.3:** Effect of tilting the vertical axis of a gravity meter to adjust its natural period: a) finite positive period (land gravity meters), b), c) negative periods, unstable conditions, d), e), infinite periods, f) infinite period with high damping (air/sea gravity meters). a to e utilize air damping, f fluid damping in this analog model.

### 3.1.2 Brief mathematical theory of operation

At first, we will neglect any horizontal acceleration. The characteristic of a “zero-length” spring dynamic gravity meter is described by the differential equation

$$g + \ddot{z} + b\ddot{B} + f\dot{B} + kB - cS = 0 \quad (3.1.2)$$

with

$g$  = gravity variation,

$\ddot{z}$  = vertical acceleration of gravity meter case,

$B$  = displacement of gravity meter test mass relative to a null position in the meter case,

$S$  = spring tension and

$b, f, k, c$  = constants, assuming linear meter characteristics.

The first three terms  $g$ ,  $\ddot{z}$  and  $b\ddot{B}$  of equation (3.1.2) result from gravitation and acceleration forces acting on the mass. Only if the mass is assumed to move along a straight (vertical) line  $b$  is constant. For further analysis, we assume this is the case for our meter. The term  $f\dot{B}$  results from damping and  $kB$  from the restoring force of the spring tension.  $cS$  represents the vertical force per unit mass exerted at the center of the test mass defined by the mechanical link(s) when the mass is nulled (i.e. shifting point A by a micrometer screw in Fig. 3.1.1).

In the next step, non-linearities of the meter characteristics are discussed.  $f, k$  and  $c$  then become variable coefficients that can be written as

$$g + \ddot{z} + b\ddot{B} + (f_0 + f_v)\dot{B} + (k_0 + k_v)B - (c_0 + c_v)S = 0 \quad (3.1.3)$$

with

$f_0, k_0, c_0$  = constants and

$f_v, k_v, c_v$  = variables.

If the variable part of equation (3.1.3) is neglected, the error for non-linear effects is

$$e = f_v\dot{B} + k_vB - c_vS. \quad (3.1.4)$$

All coefficients of equation (3.1.4) are proportionally dependent on  $\ddot{z}$  because any vertical acceleration will affect the geometry of the sensor (spring, test mass, hinges, etc.). More specifically, the coefficient  $f_v$  is also proportional to  $B$  and  $\dot{B}$  because the damping depends firstly on the relative position of the dampers to the test mass and secondly on the velocity relative to the meter case. The coefficient  $k_v$  should be only proportional to  $B$ . The same accounts for  $c_v$  and  $S$ , they also should have a simple proportional relationship. For further considerations,  $S$  will be expressed as  $S_0 + S_v$ . Herein,  $S_0$  is the average of  $S$  and  $S_v$  is the variable part with an average of zero. Following these assumptions, equation (3.1.4) can be re-written as

$$e = (f_1\ddot{z} + f_2B + f_3\dot{B})\dot{B} + (k_1\ddot{z} + k_2B)B - (c_1\ddot{z} + c_2S_0 + c_2S_v)(S_0 + S_v) = 0. \quad (3.1.5)$$

It can be shown that  $f_2B\dot{B}$  is neglectable [LaCoste, 1968]. For slow altitude variations and for marine surveys the term  $S_0\ddot{z}$  will be neglectable because  $S_0$  is a constant and the average

of  $\ddot{z}$  will be close to zero. The average value of  $S_0 S_v$  is zero because the average of  $S_v$  is zero. The term  $c_2 S_0^2$  has no dependency on  $\ddot{z}$  and presumably is taken care of in the static calibration of the sensor. These new assumptions lead to a simplified expression of equation (3.1.5) representing an average error

$$\langle e \rangle = \langle (f_1 \ddot{z} + f_3 \dot{B}) \dot{B} \rangle + \langle (k_1 \ddot{z} + k_2 B) B \rangle - \langle (c_1 \ddot{z} + c_2 S_v) S_v \rangle = 0. \quad (3.1.6)$$

Taking into account a special meter design, equation (3.1.6) can be further simplified. If  $S$  is not varied when a reading is taken,  $S_0$  will be zero. In our meter  $S$  is varied by means of a gyro, so  $S_v$  will be proportional to  $\ddot{z}$ :

$$S_v = S_2 \ddot{z}. \quad (3.1.7)$$

Furthermore, our meter is highly damped, meaning that  $\dot{B}$  is proportional to  $\ddot{z}$ :

$$\dot{B} = K \ddot{z}. \quad (3.1.8)$$

Finally, LaCoste [1967] has shown that  $\ddot{z}$  and  $\dot{z}$  are  $90^\circ$  out of phase, so their product is zero. Applying this result and equations (3.3.7) and (3.3.8) in equation (3.3.6) we get

$$\langle e \rangle = (f_1 K + f_3 K^2 - c_1 S_2 - c_2 S_2^2) \langle \ddot{z}^2 \rangle + k_2 K^2 \langle \dot{z}^2 \rangle = 0. \quad (3.1.9)$$

Equation (3.1.9) describes the error contribution expected for smooth aero-gravimetric flights. In a last simplification, LaCoste [1967] analyzes the error contribution from equation (3.1.9) for a shipboard (not airborne!) gravity meter and comes to the following conclusions:

- The coefficients of the damping term  $(f_0 + f_v) \dot{B}$  can vary only approximately 1% in a vertical acceleration range from 0 to 0.1 g. This variation comes down to 0.5% for a range of 0 to 0.2g and 0.25% for 0 – 0.4g. It therefore can be regarded as linear.
- The variability of the term  $(k_0 + k_v) B$  on the beam displacement is only 1 mGal over the full range of B. Therefore, we can neglect it.
- The variation in S is so slow compared to all other changes, which means that it can be treated as a linear feature of the meter.

So for the marine (not the airborne!) environment equation (3.1.9) simplifies to

$$\langle e \rangle = (f_1 K + f_3 K^2) \langle \ddot{z}^2 \rangle = 0. \quad (3.1.10)$$

Until now, horizontal accelerations were not accounted for. There are two ways to handle the effects of horizontal accelerations: a gimbal suspension or a stabilized platform. In our case we only deal with the stabilized platform (see figure 3.2.1). On a perfectly horizontal platform any horizontal acceleration would have no effect on the gravity reading. The gravity error that is induced by a platform with an offset angle  $\varepsilon$  towards the horizontal is given by

$$e_g = g \cos \varepsilon - \ddot{x} \sin \varepsilon - g. \quad (3.1.11)$$

For small angles  $\varepsilon$  equation (3.1.11) can be simplified to

$$e_g \cong -\ddot{x} \varepsilon - \frac{g \varepsilon^2}{2}. \quad (3.1.12)$$

The term  $\ddot{x}\varepsilon$  in equation (3.1.12) is caused by the horizontal acceleration; the term  $g\varepsilon^2/2$  is the static error. With reference to equation (3.1.12), in order to achieve a gravity reading accuracy of 1 mGal, gyros with accuracy of about 0.1 mGal for a negative feedback loop are required. However, a gyro alone cannot control the verticality of a platform because

- the reference line the gyro was tuned on might not be vertical,
- the drift of a gyro and
- a gyro tends to remain fixed in space also over a rotating earth, i.e. a space-fixed platform would tend to rotate 180° per day

In short, a gyro has good control of relative angular changes, but has bad control of verticality. Therefore, it is necessary to add an accelerometer for each axis in a secondary negative feedback loop. The simplest function of the accelerometer signal to feed back for gyro stabilization is the gyro precession rate in space

$$\dot{\phi} = -k_{acc} \left( \phi + \frac{\ddot{x}}{g} \right) \quad (3.1.13)$$

with

$k_{acc}$  = constant and  $\phi + \frac{\ddot{x}}{g}$  = error signal.

Unfortunately, this negative feedback function, as described in equation (3.1.13), does not lead to satisfactory results in practical applications. One of several reasons for this is that the error signal has to be adjusted for each rotation of the meter about the vertical. Moreover, the drift of the gyro is not corrected for. A significantly more stable solution is achieved with the negative feedback function

$$\dot{\phi} + 2f\omega_0 \left( \phi + \frac{\ddot{x}}{g} \right) + \omega_0^2 \int \left( \phi + \frac{\ddot{x}}{g} \right) dt = 0, \quad (3.1.14)$$

or

$$\ddot{\phi} + 2f\omega_0 \left( \dot{\phi} + \frac{\ddot{x}}{g} \right) + \omega_0^2 \left( \phi + \frac{\ddot{x}}{g} \right) = 0 \quad (3.1.15)$$

with

$\omega_0$  = circular natural frequency or  $2\pi/\omega_0$  = natural period .

The integral term in equation (3.1.14) eliminates errors in  $\phi$  due to the rotation of the earth. A closer look at equation (3.1.15) will reveal it as the differential equation of a pendulum. Both equations, (3.1.14) and (3.1.15), can be regarded as the transfer function of the meter. The period of the platform (or pendulum) is determined by the amount of integral feedback. For our meter, a 2-, 4-, and 12 minute period can be chosen. Boebel [2000] gives a comparison between the theoretical and measured transfer function for the S-56 meter on a Dornier-228 aircraft. Horizontal accelerations with a longer period than the platform period (as in long turns) are regarded by the platform as apparent changes of the vertical; the platform then loses its real vertical alignment. The damping of the platform (or pendulum) is controlled by the amount of the ordinary (or residual to integral) feedback. This damping acts as a high-pass filter of the horizontal accelerations. In order to determine the permissible accelerometer feedback constants for a stabilized platform, we combine the equations (3.1.15) and (3.1.12). We will consider a sinusoidal horizontal acceleration and will examine the steady-state solution [LaCoste, 1968].

Substituting

$$\phi = e^{i\omega t} \quad (3.1.16)$$

in equation (3.1.15), we get

$$\phi = -\frac{\omega_0^2 + 2if\omega_0\omega}{\omega_0^2 - \omega^2 + 2if\omega_0\omega} \left( \frac{\ddot{x}}{g} \right) \quad (3.1.17)$$

with

$f$  = damping factor.

During perfect operation  $\phi$  would be zero, otherwise it would equal equation (3.1.12), becoming  $\phi = \varepsilon$ . The second term of equation (3.1.12) then becomes

$$\frac{-g\langle e^2 \rangle}{2} = -\frac{\omega_0^2 + 2if\omega_0\omega}{\omega_0^2 - \omega^2 + 2if\omega_0\omega} \left( \frac{\langle \ddot{x}^2 \rangle}{2g} \right) \quad (3.1.18)$$

$$= -\frac{\omega_0^4 + 4f^2\omega_0^2\omega^2}{\omega_0^4 + 2\omega_0^2\omega^2(2f^2 - 1) + \omega^4} \left( \frac{\langle \ddot{x}^2 \rangle}{2g} \right) \quad (3.1.19)$$

In the first term of equation (3.1.12) only the component in phase with  $\ddot{x}$  is significant. This is the real part of equation (3.1.17):

$$\langle \ddot{x}e \rangle = -\frac{\omega_0^4 + \omega_0^2\omega^2(4f - 1)}{\omega_0^4 + 2\omega_0^2\omega^2(2f^2 - 1) + \omega^4} \left( \frac{\langle \ddot{x}^2 \rangle}{g} \right). \quad (3.1.20)$$

Adding equations (3.1.19) and (2.2.20) now gives

$$\langle e_g \rangle = -\frac{(\omega_0/\omega)^4 + 2(2f^2 - 1)(\omega_0/\omega)^2}{(\omega_0/\omega)^4 + 2(2f^2 - 1)(\omega_0/\omega)^2 + 1} \left( \frac{\langle \ddot{x}^2 \rangle}{2g} \right). \quad (3.1.21)$$

Equation (3.1.21) shows that the error is small when  $(\omega_0/\omega)$  is small or when the wave frequency is considerably greater than the natural frequency of the stabilized platform (eigen frequency of the pendulum). Another important step to decrease the error of the platform is inherent in the term  $(2f^2 - 1)$ . If this term becomes zero, the error is minimized. This corresponds to making the damping  $f^2 = 1/\sqrt{2} = 0.707$  times the critical damping. If this sort of damping is utilized, equation (3.1.21) becomes

$$\langle e_g \rangle = -\frac{(\omega_0/\omega)^4}{(\omega_0/\omega)^4 + 1} \left( \frac{\langle \ddot{x}^2 \rangle}{2g} \right). \quad (3.1.22)$$

When the natural platform period is set to 4 minutes (as in most cases for airborne gravity flights) the error is still smaller than 1 mGal for periods less than 35 seconds. Some more test calculations show that track deviations of less than 30 meters still result in errors less than 1 mGal for a 4 minute period [LaCoste, 1967]. To minimize this type of error, well-tuned autopilot systems are strongly suggested. Brozena and Peters [1988] estimate a platform error in airborne applications of 2.1 mGal for a 4-minute natural period, the period used in most of our flights.

Swain [1996] took equation (3.1.12) and (3.1.15) to develop another estimation of the tilt error of the platform. A sinusoid  $\ddot{x}$ , as used by LaCoste [1967] to derive equation (2.2.17), is basically equivalent to the Fourier transform of (3.1.15):

$$\Theta(\omega) = H(\omega) \frac{\ddot{X}(\omega)}{g} \quad (3.1.23)$$

with

$$H(\omega) = -\frac{\omega_0^2 + 2if\omega_0\omega}{\omega_0^2 - \omega^2 + 2if\omega_0\omega}.$$

In equation (3.1.23),  $\ddot{X}(\omega)$  is the Fourier transform of the input and  $\Theta(\omega)$  is the Fourier transform of the output.  $H(\omega)$  is the transfer function. Applying a digital filter to the horizontal acceleration  $\ddot{x}/g$  yields the tilt error. This filter might be realized in the frequency domain, as suggested with equation (3.1.23), or in the time domain using a suitable convolution filter. Swain [1996] developed a second-order recursive filter using a bilinear transformation of the form

$$q_j = c_0 p_j + c_1 p_{j-1} + c_2 p_{j-2} + d_1 q_{j-1} + d_2 q_{j-2} \quad (3.1.24)$$

with

$$c_0 = (a+b)7(4+a+b),$$

$$c_1 = 2b/(4+a+b),$$

$$c_2 = (b-a)/(4+a+b),$$

$$d_1 = (8-2b)/(4+a+b),$$

$$d_2 = (a-b-4)/(84+a+b),$$

$$a = 4f\omega_0\Delta t,$$

$$b = (\omega_0\Delta t)^2.$$

$\Delta t$  is the sample interval. This filter is applied in our aerogravity software. With

$$\ddot{x}_j = (x_{j-1} + x_{j+1} - 2x_j)\Delta t^2 \quad (3.1.25)$$

the horizontal accelerations  $\ddot{x}$  are computed from  $x$ . The same formula is used to derive the vertical acceleration from GPS locations. When the tilt angles for both axes are determined in the way described, the total tilt error is

$$e = \ddot{x} \sin(\phi) + \ddot{y} \sin(\lambda) + g(\phi^2 + \lambda^2)/2 \quad (3.1.26)$$

with

$\phi, \lambda$  = platform tilt angles and

$\ddot{x}, \ddot{y}$  = acceleration in forward and cross direction.

Valliant [1992] developed another method to estimate the platform tilt error. Starting with the formula

$$g_{total}^2 = g_{Meter}^2 + A^2 = (g + \ddot{z})^2 + a^2 \quad (3.1.27a)$$

or

$$g + \ddot{z} = \sqrt{g_{Meter}^2 + A^2 - a^2} \quad (3.1.27b)$$

we derive

$$g + \ddot{z} = g_{Meter} \sqrt{1 + \frac{A^2 - a^2}{g_{Meter}^2}} \cong g_{Meter} \left(1 + \frac{A^2 - a^2}{2g_{Meter}^2}\right) = g_{Meter} + \frac{A^2 - a^2}{2g_{Meter}} \quad (3.1.27c)$$

with

$$a = \sqrt{\ddot{x}_{GPS,East} + \ddot{y}_{GPS,North}} \quad \text{and}$$

$$A = \sqrt{\ddot{x}_{Meter,LongitudinalAxis} + \ddot{y}_{Meter,CrossAxis}} .$$

The approximation (3.1.27c) estimates the tilt error as

$$e = \sqrt{A^2 + a^2} / 2g_m \cong \sqrt{A^2 + a^2} / 2g . \quad (3.1.28)$$

This very practical and easy approach is also used in our aerogravimetry software as a first order estimate for the gravity effect of a platform tilt.

### *Schuler period tuning*

This paragraph will describe very briefly the problem of Schuler tuning. Although Schuler tuning is not realized in our aerogravimetry system, the Schuler period is an important inherent effect that everybody working in aerogravimetry should be aware of.

The differential equation (3.1.15) describes the characteristic of pendulum for an infinite earth radius. As soon as the platform (the aircraft) is not maintaining a constant speed and direction, we have to a change equation (3.1.15) to fit it to the earth's radius:

$$\ddot{\phi} + 2f\omega_0 \left(\dot{\phi} + \frac{1}{R} \int \ddot{x} dt + \frac{\ddot{x}}{g}\right) + \omega_0^2 \left(\phi + \frac{1}{R} \iint \ddot{x} dt^2 + \frac{\ddot{x}}{g}\right) = 0 \quad (3.1.29)$$

with

$R$  = radius of the earth.

For our platform (controlled by the gyros) we now would like use a direction normal to the surface of the earth rather than an arbitrary space fixed orientation. Therefore we define

$$\phi_e = \phi + \frac{1}{R} \iint \ddot{x} dt^2 \quad (3.1.30)$$

as the vertical reference. Using this substitution in equation (3.1.29) we get

$$\ddot{\phi}_e - \frac{\ddot{x}}{R} + 2f\omega_0 \left(\dot{\phi}_e + \frac{\ddot{x}}{g}\right) + \omega_0^2 \left(\phi_e + \frac{\ddot{x}}{g}\right) = 0 . \quad (3.1.31)$$

It is desired to make (3.1.31) independent from  $\ddot{z}$ . Therefore, we set  $f = 0$  and

$$\omega_0 = \sqrt{g/R}. \quad (3.1.32)$$

Then, equation (3.1.31) becomes the simple differential equation

$$\ddot{\phi}_e + (g/r)\phi_e = 0. \quad (3.1.33)$$

A platform satisfying these conditions is known as a Schuler tuned stabilized platform. The period of a Schuler platform is given by equation (3.1.32):

$$\frac{2\pi}{\omega_0} = \frac{2\pi}{\sqrt{g/R}} \approx 84.4 \text{ min}. \quad (3.1.34)$$

It is obvious from this very long period, that a Schuler-tuned platform would need extremely accurate gyros and accelerometers that have virtually no errors or drifts within this time range. For this reason, so far we are not operating a Schuler-tuned platform.

#### *Cross coupling effects*

Another source of errors in aerogravimetry is the cross coupling between horizontal and vertical accelerations especially in spatially expanded sensors such as the LaCoste & Romberg gravity meters. Cross coupling can be largely limited by a sensor that is symmetrical about the vertical axis or by continuously nulling the sensor. In our case, we have to correct for this effect. For further considerations, we will examine the inherent cross coupling and the cross coupling due meter imperfections.

#### *Inherent cross coupling*

Inherent cross coupling is a fundamental property of any beam-type gravity meter and cannot be eliminated. The differential equation for a beam-type gravity meter in the case of no horizontal accelerations was given in equation (3.1.2). In order to account for spatial effects of a hinged beam holding a test mass, we have to multiply all terms of (3.1.2) with the torque

$$T = MD \sin \beta \quad (3.1.35)$$

with

$M$  = test mass,  $D$  = length of hinge,

$\beta$  = hinge angle towards the horizontal.

Next, the term  $-MD\ddot{x}$  must be added to account for the horizontal acceleration effect. The resulting equation is then

$$g + \ddot{z} - \ddot{x} \tan \beta + b\ddot{B} + f\dot{B} + kB - cS = 0. \quad (3.1.36)$$

Comparing (3.1.2) and (3.1.36) we determine the error associated with omitting the effects of horizontal accelerations translated into cross coupling as

$$e = \ddot{x} \tan \beta \cong \ddot{x} \beta. \quad (3.1.37)$$

Assuming that, due to excitation by aircraft movements and gravity changes, the hinge and test mass are swinging around the horizontal, we construct

$$\beta = \beta_0 + \beta_1 \sin(\omega_2 t + \psi) \quad (3.1.38)$$

and

$$\ddot{x} = \ddot{x}_1 \sin \omega_1 t. \quad (3.1.39)$$

Applying this disturbance model to (3.1.37) leads to the expression

$$e = x_1 \beta_0 \sin \omega_1 t + x_1 \beta_1 \sin \omega_1 t \sin(\omega_2 t + \psi). \quad (3.1.40)$$

The average value of  $e$  is zero except when  $\omega_1 = \omega_2$ . Then equation (3.1.40) becomes

$$\langle e \rangle = \frac{1}{2} \ddot{x}_1 \beta_1 \cos \psi. \quad (3.1.41)$$

Equation (3.1.41) describes the average error of the inherent cross coupling. Since the beam (hinge plus test mass) is driven by vertical accelerations,  $\beta$  will have the same period as the vertical accelerations. Therefore, inherent cross coupling exists when horizontal and vertical accelerations have the same period. LaCoste [1967] determined that for a horizontal acceleration of  $\pm 0.1g$  and  $\psi = 0$ ,  $e = 49$  mGal. Valliant [1992] simplifies equation (3.1.41) for a more practical application. With  $\beta \propto \ddot{z}$  and hence  $\beta \propto d\dot{z}/dt$  for sinusoidal accelerations,  $\beta$  and  $\dot{z}$  are proportional to each other with a phase difference of  $\pi/2$ . We then can approximate from equation (3.1.41)

$$\langle e \rangle \cong \frac{1}{2} \ddot{x}_1 \dot{z}_1 \cos(\psi + \frac{\pi}{2}). \quad (3.1.42)$$

From equation (3.1.42), we conclude that the error is proportional to the product of longitudinal acceleration and beam position. Diagonal aircraft motions do not contribute to the inherent cross coupling. Nevertheless, if the meter is mounted off the roll and pitch axes of an aircraft, additional accelerations are generated that exacerbate the non-linear errors.

#### *Imperfection cross coupling*

LaCoste et al. [1967] estimates that the cross coupling error is often higher than the inherent cross coupling. Valliant [1992] gives an analysis of the imperfection cross coupling. It arises because the suspension of the platform is not stiff enough. An ideal system would have very low compliance (mechanically low-pass filtered) in the vertical direction and would be perfectly rigid in all other directions. Since all mechanical systems must exhibit some elasticity, this ideal cannot be realized. This is especially true for instruments that are expected to have a resolution of 0.1 mGal in the presence of 100000 mGal accelerations in vertical and horizontal directions, being equivalent to signal to noise ratio of  $10^{-6}$ . Moreover, small mechanical deviations in the air damper can cause large effects. For example, an eccentricity of 0.0025 mm in damper rings generates an error of 57 mGal in the presence of 30000 mGal vertical and horizontal accelerations. The distance between damper rings is about 0.1 mm (see Fig. 3.1.2).

#### *Cross coupling correction*

After LaCoste [1967] and Valliant [1992], we can assume that all systematic errors of our sensor, in conjunction with its platform, can be described as a power series of velocities and

accelerations. In such a power series, all first-order terms either average out or are elements of the Eötvös correction. The power series is then

$$e_g = a_1 \langle \ddot{x}^2 \rangle + a_2 \langle \ddot{y}^2 \rangle + a_3 \langle \ddot{z}^2 \rangle + a_4 \langle \dot{x}^2 \rangle + a_5 \langle \dot{y}^2 \rangle + a_6 \langle \dot{z}^2 \rangle + a_7 \langle \ddot{x}\dot{z} \rangle + a_8 \langle \ddot{y}\dot{z} \rangle + a_9 \langle \ddot{x}\ddot{z} \rangle + a_{10} \langle \ddot{y}\ddot{z} \rangle \dots + a_n \langle \ddot{x}^2 \dot{z} \rangle + \dots \quad (3.1.43)$$

The first two terms arise from platform leveling errors. The third and the sixth term arise from non-linearities in damping. After careful examination it was found that the fourth and fifth terms can be neglected for our type of meter. The seventh and eighth terms are due to inherent cross coupling. From laboratory tests, it also was found that the sixth term can be neglected. The ninth and tenth term are due to imperfection cross coupling. The nth term arises from second order imperfection cross coupling. After eliminating negligible terms we are left with

$$e_g = a_1 \langle \ddot{x}^2 \rangle + a_2 \langle \ddot{y}^2 \rangle + a_3 \langle \ddot{z}^2 \rangle + a_8 \langle \ddot{y}\dot{z} \rangle + a_9 \langle \ddot{x}\ddot{z} \rangle + a_{10} \langle \ddot{y}\ddot{z} \rangle \dots + a_n \langle \ddot{x}^2 \dot{z} \rangle + \dots \quad (3.1.44)$$

Although not all of these terms arise from cross coupling effects, this correction formula is generally named the cross coupling correction. The great advantage of equation (3.1.44) is that the correction can be computed as a linear combination of observable quantities. All average values in the terms must be computed in real time. Therefore, the seven observables left are recorded as part of the gravity meter data stream as “cross coupling monitors” (with the above mentioned constraints). The coefficients are determined empirically through cross correlation analysis in laboratory tests. Each of the “cross coupling monitors” have been assigned names:

- $\langle \ddot{x}^2 \rangle$  = XACC<sup>2</sup> (square of the cross accelerometer output, displays platform leveling error in x-axis),
- $\langle \ddot{y}^2 \rangle$  = LACC<sup>2</sup> (square of the longitudinal accelerometer output, displays platform leveling error in y-axis),
- $\langle \dot{z}^2 \rangle$  = VE (square of the beam velocity, calibrated via vertical motion),
- $\langle \ddot{y}\dot{z} \rangle$  = VCC (longitudinal accelerometer output times beam position, calibrated via circular motion in a vertical plane),
- $\langle \ddot{x}\dot{z} \rangle$  = AX (cross accelerometer output times beam velocity, calibrated via diagonal motion up and down a ramp),
- $\langle \ddot{y}\dot{z} \rangle$  = AL (longitudinal accelerometer output times beam velocity, calibrated via diagonal motion up and down a ramp),
- $\langle \ddot{x}^2 \dot{z} \rangle$  = AX2 (square of cross accelerometer output times beam velocity, calibrated via motion along an arc of circle).

The first two of these monitors are not cross coupling effects and thus are recorded to detect and correct for platform errors but are omitted for real-time cross coupling correction computations.

Apart from laboratory calibrations, the cross coupling parameters can be derived by cross correlation to real data (ground truth data). This method is described by LaCoste [1973]. Here, the aircraft motion is described in terms of a power series of aircraft accelerations and velocities. This power series is then cross correlated to the measured, Eötvös corrected gravity (see chapter 8.2.3) to obtain a new correction term to minimize the correlation between aircraft movement and gravity observation. So if any of the cross coupling monitors shows a correlation with the observed gravity, the corresponding coefficient has to be adjusted. However, errors from a badly stabilized platform are too erratic to allow good corrections.

In the future, this method will be applied as a future option of our aerogravimetry software to estimate the data quality.

### 3.2 Platform Controller

For the best performance and accuracy of the airborne gravity measurements it is mandatory to keep the platform that holds the gravity meter system as close to horizontal as possible. To achieve this for each of the two horizontal axes, an accelerometer and a gyro are implemented. The accelerometer itself is manually controlled and leveled when the gravity meter is in an undisturbed environment. The accelerometer is then being nulled with the help of a precise water level on top of the platform. The output signal of the accelerometer is linearly related to the tilt angle of the platform and has a maximum range of about  $16^\circ$ . The accelerometer signal is sent to the gyro processor, which means that the signal is appropriately shaped for gyro input. The gyro itself only measures the angular rates of the platform, but has no information of its own about the spatial orientation. Therefore, the accelerometer input is needed. The combined signals are filtered and sent to the servomotor to correct actual deviations of the platform from the horizontal (see Fig. 3.2.1). The reaction time of this negative feedback loop is close to immediate, but it has a limited “memory” due to the gyro drift. The memory time used with the filter is about 4 minutes for airborne application and 12 minutes for ship operations. On the LaCoste & Romberg S124b platform, optical gyros are used for attitude control. They do not need any heating as the mechanical gyros, and they have excellent control of rapid angular changes.

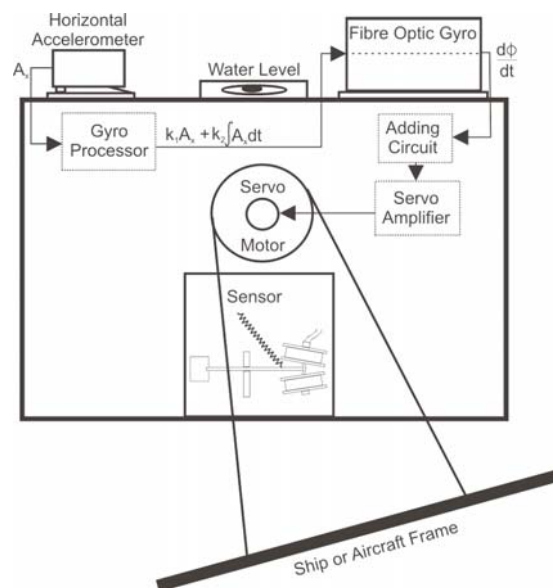


Figure 3.2.1: Schematic sketch of the platform horizontal leveling in one axis

### 3.3 Fiber optic gyros

All figures and technical design descriptions in this chapter are collected from SPIE Proceedings, Vol. 2837, Fiber Optic Gyros: 20<sup>th</sup> Anniversary Conference, Denver, Colorado, August 1996.

#### *Operation principle of optical gyros*

Two beams, one clockwise (cw) and one counter clockwise (ccw) traveling around a circle of radius (R) enclosed in a fiber of length (L), will arrive back at a reference point moving at an angular rate ( $\Omega$ ) with a phase difference ( $\Delta\phi$ , see Fig. 3.3.1) due to rotation.

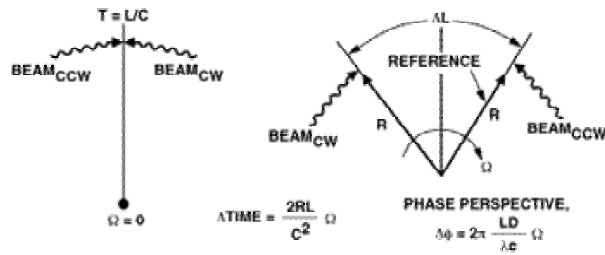


**Figure 3.3.1:** Fiber optic gyro operating principle

*Fiber optic gyro system concept*

This concept is implemented by sending the two light beams (cw and ccw) into a coil of fiber and collecting the two signals on a detector. With no rotation of the coil, the two signals add in phase and produce maximum signal power at the detector. As the coil rotates, the signals interfere and the detector power decreases. The detector power is a function of the phase difference between the two beams and is related to the rotation rate through the relationships given in Fig. 3.3.2.

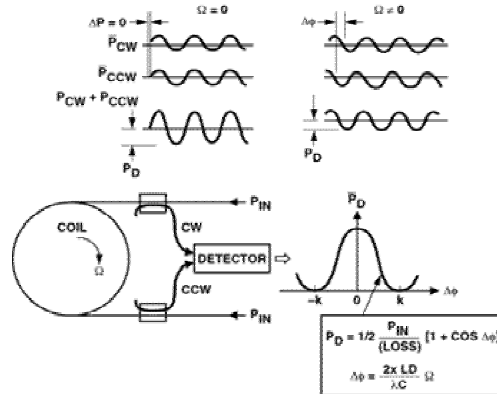


**Figure 3.3.2:** Fiber optic gyro principle

*Hardware implementation*

The light source sends light through a coupler into an integrated optics chip. On this chip, a splitter creates the cw and ccw beams that pass through the phase modulator and enter the sensing coil. On the return trip from the coil, the beams again pass through the phase modulator and are combined at the splitter. At this point, the cw and ccw signals are added and displaced in time with a phase shift proportional to the rotation rate. The combined beams travel to the photo detector where the photons of the cw and ccw are converted into electrical power (see Fig. 3.3.3). The electrical power is electronically measured and the phase shift is determined (and hence the rotation rate). The electronics also shift the relative phase of the cw and ccw beams (via the phase modulator) to maximize signal sensitivity at the detector. The phase modulator is also used for closed-loop tracking.

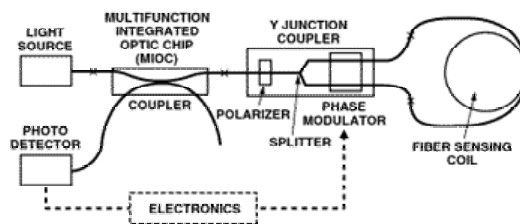


**Figure 3.3.3:** Closed loop tracking

## 4 Navigation equipment

### 4.1 IGI Inertial Navigation System

The IGI inertial navigation system showed a superb stability in performance and was very easy and safe to handle in the aircraft. The special software for the GFZ hardware version was recently upgraded to match latest Windows applications. In the future, the inertial navigation signal will not only be used for attitude determination of the aircraft but will be investigated for a possible inherent gravity signal.

#### 4.1.1 Theory of operation

##### *Introduction*

A Gyroscope is any rotating object that has two fundamental properties: gyroscopic inertia (rigidity in space) and precession (tilting of the axis). The term is applied to spherical, wheel-shaped, or disk-shaped bodies that are free to rotate in any direction. In nearly all practical applications, the gyroscope is controlled to keep it moving around axis of rotation only.

##### *Gyroscopic inertia*

Gyroscopes have inertia because, as Newton's first law of motion states, an object tends to continue moving unless an outside force acts on it. A model gyroscope, for example, has its flywheel supported in rings so that the flywheel's axle can assume any angle. When the flywheel is spinning, the model can be moved or turned in any direction, and the flywheel will maintain its original angle of rotation.

##### *Precession*

When a force is applied to a gyroscope, it causes the gyroscope's axis of rotation to precess, moving it at right angles to the direction of the applied force. A rolling hoop can demonstrate precession: to change the hoop's direction, apply a horizontal force across the top of the hoop. The hoop will then precess about its vertical axis at right angles to the applied force, turning it to roll in a new direction (Fig. 4.1.1).

##### *Applications of the gyroscope*

By using inertia and letting gravity cause precession, the gyroscope functions as a compass; controlling forces are applied automatically in just the right direction and proportion to cause the axle to point north and south. Gyrocompasses are used worldwide in ships because they indicate true, geographic north rather than magnetic north. Gyroscopes are an important part of automatic navigation and inertial guidance systems in aircraft, spacecraft, guided missiles, rockets, ships, and submarines. In these systems, gyroscopes and accelerometers continuously calculate the exact speed and direction of the craft, feeding signals into a computer, which compensate for any variations from the chosen course. Details on INS for geodetic applications are given in Jekeli [2001].

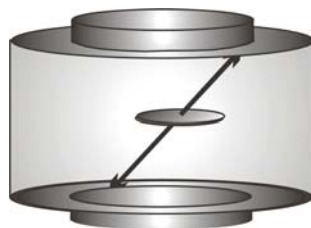


**Figure 4.1.1:** Gyro schematic – a spinning flywheel held on the edges of two plates

#### 4.1.2 Technical specifications

The standard CCNS4 system is a guidance, positioning and management system for aerial survey missions. The special version CAE-10-01 was adapted to GFZ requirements. The main task of the system is not the flight management, but the attitude measurement of the aircraft. Thus, most flight control options were omitted in favor of maximum control over the raw data. So one of the major disadvantages of INS packages for aerogravimetry was overcome: direct control of the raw data is guaranteed with the CAE-10-01 system.

The basic system consists of the central computer unit CAE-10-01 that handles the data flow, acquisition and visualization. The CAE-10-01 can either be used as a sub-unit of the CCNS4 system with status reports displayed on the CCNS4 information pages, or as a stand-alone data acquisition unit. For all airborne missions of the GFZ so far, the system was operated in the latter mode.

This special version CAE-10-01 can be used to control either remote sensing systems or just be taken for aircraft attitude measurements. Together with the AEROcontrol system, based on DGPS and information from an inertial measurement unit (IMU), it allows real-time and post-processing of sensor or aircraft frame positions for given instants. The system allows the determination of the elements of exterior orientation ( $\phi$ ,  $\omega$ ,  $\kappa$  and  $x/y/z$ ). Heading information with an accuracy of  $1/10^\circ$  and pitch as well as roll information are furnished with an accuracy of  $1/100^\circ$ .

The principal navigation sensors of the AEROcontrol system are a 12 channel parallel L1/L2 RX GPS receiver (Ashtech Z-Surveyor) operating at 1 Hz and a dry tuned gyro with a separate sensor head (modified LITEF LCR 88) operating at 50 Hz.

The data output is the system time, the angle increments and the velocity increments in the x-, y-, z-direction with a frequency of 50 Hz. Additionally, the system time, the GPS week-second and 5 optional channels are recorded at 1 Hz. This IMU and optional sensor data is stored parallel with the Ashtech GPS data on a portable flash disk. Events are time stamped and marked in an extra data channel (waypoints, power settings, etc.)

After first computing the kinematic DGPS positions from the Ashtech GPS receiver, the data can be post-processed using the IGI AEROoffice software.

The system is mainly being used to control the aircraft position and attitude at high rates. Nevertheless, there will be future investigations on the data acquired from Braunschweig with the CAE-10-01 system.

#### 4.2 GPS-Receivers

During the AGFA test installation and flights only Trimble 4000 SSE receivers and one Ashtech-Z-Surveyor were used. Fig. 4.1 shows the Trimble 400 SSE reference station at the airport at the DLR Oberpfaffenhofen. The mix of the receivers and the quality of the Trimble 4000 SSE receivers led to some problems during the data processing. From former airborne gravimetry campaigns such as AGMASCO [Forsberg et al., 1996] we learned that receiver mixing is not a good idea. Receivers in the air and on the ground should be as close to each other in observation technology as possible. In that way, systematic errors between receivers can be reduced dramatically. Furthermore, we learned that Trimble 4000 SSI receivers have a considerably better performance than those of the 4000 SSE series. Unfortunately, we could not obtain 4000 SSI receivers for precious tests. For the flight activities only one Trimble 4000 SSI was available to be installed in the aircraft.

Another problem that occurred was that the lowest elevation angle for satellite tracking was chosen to be  $10^\circ$ . This induced the problem that during aircraft roll, low satellites emerging or submerging were “switched on and off” continuously during observations due to the roll of

the aircraft. The Ashtech aircraft antenna especially suffered from this effect. For future applications, we therefore suggest that the elevation mask angle be set between  $10^\circ$  and  $0^\circ$ .

At present, 5 GPS receivers of a new generation are being procured, three for ground reference coverage and two for aircraft installation, more receivers of the same type will be available at the GFZ if needed. These receivers are Novatel OEM-4 receivers. They are capable of precise kinematic measurements at high data rates (up to 20 Hz). These receivers will considerably enhance the crucial GPS quality for our aerogravimetry system and will give a much better reduction control for more strap-down airborne gravimetry systems.

#### 4.2.1 Theory of operation

Most illustrations and text descriptions of this chapter are collected from P. H. Dana, [http://www.colorado.edu/geography/gcraft/notes/gps/gps\\_f.html](http://www.colorado.edu/geography/gcraft/notes/gps/gps_f.html).

##### *The GPS institution*

The Global Positioning System (GPS) is funded and controlled by the United States Department of Defense (DOD). While there are many thousands of civil users of GPS worldwide, the system was designed for and is operated by the U.S. military forces. GPS provides specially coded satellite signals that can be processed in a GPS receiver, enabling the receiver to compute position, velocity and time. A minimum of four GPS satellite signals are used to compute positions in three dimensions and the time offset in the receiver clock (Fig. 4.2.1).

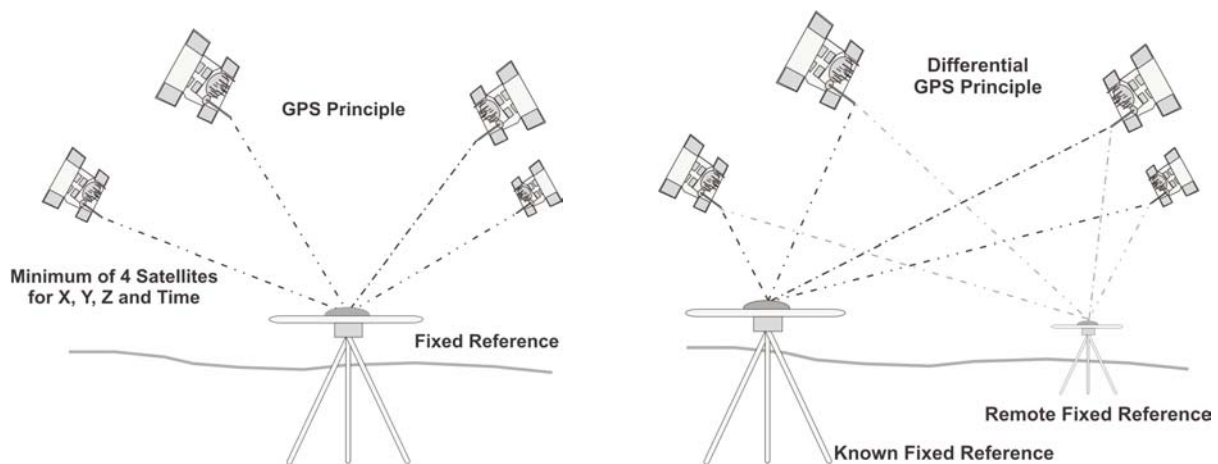


**Figure 4.2.1:** The GPS principle

##### *The GPS signals*

A GPS satellite transmits two microwave carrier signals. The L1 frequency (1575.42 MHz) carries the navigation message and the single point positioning code signals. The L2 frequency (1227.60 MHz) is used to measure the ionospheric delay by pulse per second (PPS) generator equipped receivers. Three binary codes shift the L1 and/or L2 carrier phase.

The C/A code (coarse acquisition) modulates the L1 carrier phase. This C/A signal is a repeating 1 MHz pseudo random noise (PRN) code. This noise-like code modulates the L1 carrier signal, "spreading" the spectrum over a 1 MHz bandwidth (see Fig. 4.2.2).

The C/A code repeats every 1023 bits (one millisecond). There is a different C/A code PRN for each satellite. Their PRN number, the unique identifier for each pseudo-random-noise code, often identifies GPS satellites. The C/A code that modulates the L1 carrier is the

basis for the civil single point positioning (SPS). The P-code (precise code) modulates both the L1 and L2 carrier phases. The P-Code is a very long (seven days) 10 MHz PRN code. In the anti-spoofing (AS) mode of operation, the P-code is encrypted into the Y-code. The encrypted Y-code requires a classified anti-spoofing module for each receiver channel and is for use only by authorized users with cryptographic keys. The P (Y)-Code is the basis for the PPS. The navigation message also modulates the L1-C/A code signal. The navigation message is a 50 Hz signal consisting of data bits that describe the GPS satellite orbits, clock corrections, and other system parameters.

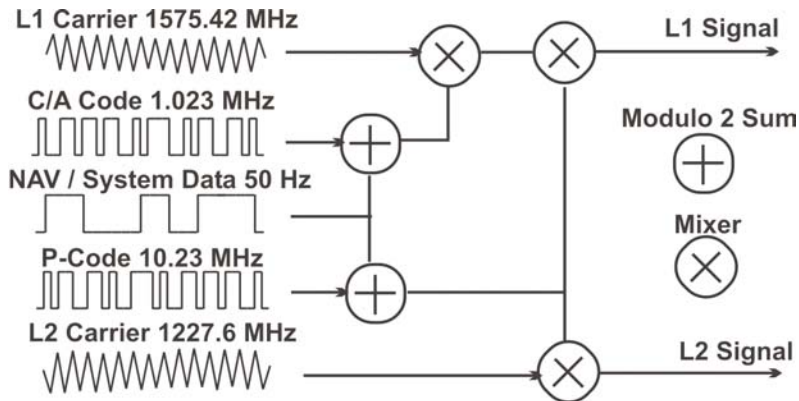


Figure 4.2.2: GPS signals

The nominal GPS operational constellation consists of 24 satellites that orbit the earth in 12 hours (Fig. 4.2.3). There are often more than 24 operational satellites as new ones are launched to replace older satellites. The satellite orbits repeat almost the same ground track (as the earth turns beneath them) once each day. The orbit altitude is such that the satellites repeat the same track and configuration over any point approximately each 24 hours (4 minutes earlier each day). There are six orbital planes (with nominally four satellites in each), equally spaced (60 degrees apart), and inclined at about fifty-five degrees with respect to the equatorial plane. This constellation provides the user with between five and eight satellites visible from any point on the earth.

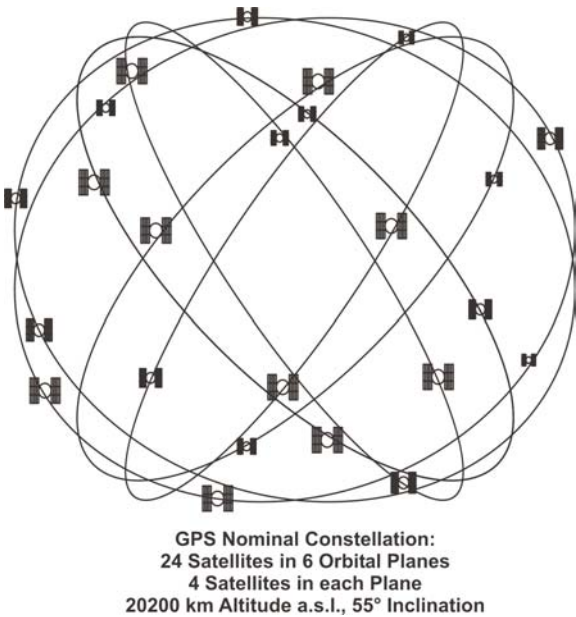
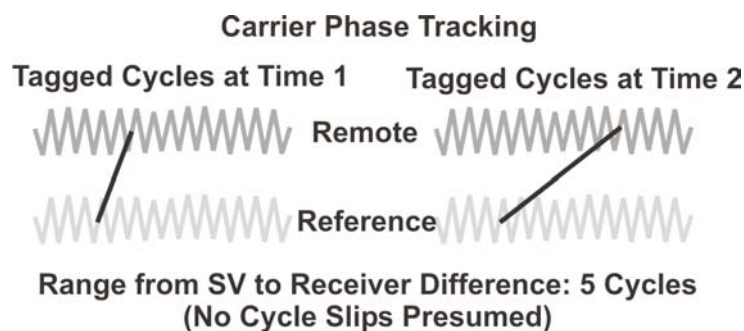


Figure 4.2.3: GPS constellation

The GPS user segment consists of the GPS receivers and the user community. GPS receivers convert satellite signals into position, velocity, and time estimates. Four satellites are required to compute the four dimensions of X, Y, Z (position) and time. GPS receivers are used for navigation, positioning, time dissemination, and other research. Navigation in three dimensions is the primary function of GPS.

Carrier-phase tracking of GPS signals has resulted in a revolution in land surveying. A line of sight along the ground is no longer necessary for precise positioning. This use of GPS requires specially equipped carrier tracking receivers. The L1 and/or L2 carrier signals are used in carrier phase surveying. L1 carrier cycles have a wavelength of 19 centimeters. If tracked and measured these carrier signals can provide ranging measurements with relative accuracies of millimeters under special circumstances. Tracking carrier phase signals provides no time of transmission information. The carrier signals, while modulated with time tagged binary codes, carry no time-tags that distinguish one cycle from another. The measurements used in carrier-phase tracking are differences in carrier-phase cycles and fractions of cycles over time. At least two receivers track carrier signals at the same time. Ionospheric delay differences at the two receivers must be small enough to insure that carrier phase cycles are properly accounted for. This usually requires that the two receivers are within about 30 km of each other. Carrier phase is tracked at both receivers and the changes in tracked phase are recorded over time in both receivers (Fig. 2.4.2).



**Figure 4.2.4:** Carrier phase tracking (SV – space vehicle)

All carrier-phase tracking is differential, requiring both a reference and remote receiver tracking carrier phases at the same time (Fig. 4.2.1 and 4.2.5). Unless the reference and remote receivers use L1-L2 differences to measure the ionospheric delay, they must be close enough to ensure that the ionospheric delay difference is less than a carrier wavelength. Using L1-L2 ionospheric measurements and long measurement averaging periods, relative positions of fixed sites can be determined over baselines of hundreds of kilometers. Phase difference changes in the two receivers are reduced using software to differences in three position dimensions between the reference station and the remote receiver. High accuracy range difference measurements with sub-centimeter accuracy are possible. Problems result from the difficulty of tracking carrier signals in noise or while the receiver moves. Two receivers and one satellite over time result in single differences.

Two receivers and two satellites over time provide double differences. Post-processed static carrier-phase surveying can provide 1-5 cm relative positioning within 30 km of the reference receiver with measurement time of 15 minutes for short baselines (10 km) and one hour for long baselines (larger than 30 km). Rapid static or fast static surveying can provide 4-10 cm accuracies with 1-kilometer baselines and 15 minutes of recording time. Real time kinematic (RTK) surveying techniques can provide centimeter measurements in real time over 10 km baselines tracking five or more satellites and real time radio links between the reference and remote receivers.

In order to correctly estimate the number of carrier wavelengths at the reference and remote receivers, they must be close enough to insure that the ionospheric delay difference is less than a carrier wavelength. This usually means that carrier-phase GPS measurements must be taken with a remote and reference station within about 30 kilometers of each other. Special software is required to process carrier-phase differential measurements. Newer techniques such as real time kinematic (RTK) processing allow for centimeter relative positioning with a moving remote receiver.

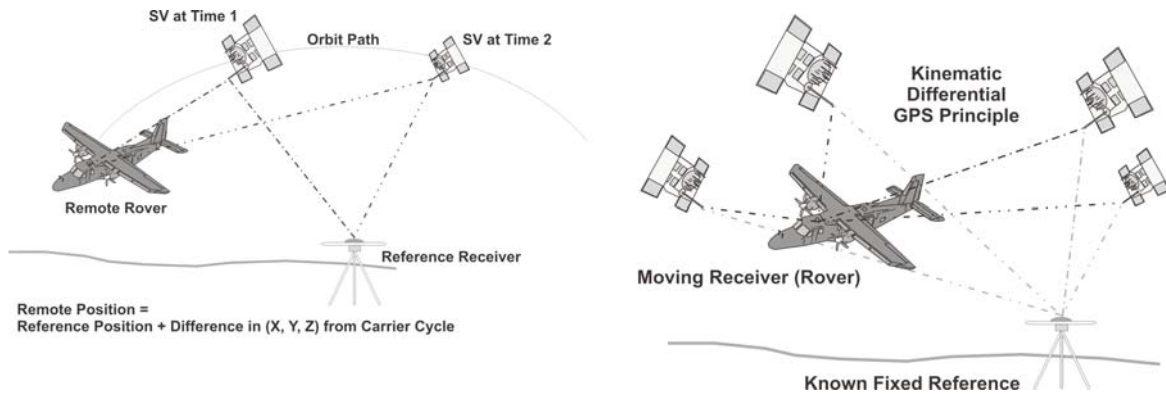


**Figure 4.2.5:** Carrier phase positioning

*Error sources*

Selective availability (SA) is the intentional degradation of the SPS signals by a time varying bias. The potential accuracy of the C/A code of around 30 meters is reduced to 100 meters (two standard deviations). About five years ago, the SA was switched off.

SV clock errors uncorrected by Control Segment can result in one-meter errors. Ephemeris data errors are about 1 meter, tropospheric delay errors around 1 meter. The troposphere is the lower part of the atmosphere (ground level to from 8 to 13 km) that experiences the changes in temperature, pressure, and humidity associated with weather changes. Complex models of tropospheric delay require estimates or measurements of these parameters. Un-modeled ionosphere delay errors are in the range of 10 meters. The ionosphere is the layer of the atmosphere from 50 to 500 km that consists of ionized air. The transmitted model can only remove about half of the possible 70 ns of delay leaving a ten meter un-modeled residual.

Multi-path errors are about 0.5 meters. Multi-path is caused by reflected signals from surfaces near the receiver that can either interfere with or be mistaken for the signal that follows the straight-line path from the satellite. Multi-path is difficult to detect and sometime hard to avoid. Table 4.2.1 summarizes errors in GPS positioning.

GPS Error Sources		
Error source	Typical Range of Error [meter]	DGPS Range of Error (Baseline < 100 km) [meter]
SV Clock	1	
SV Ephemeris	1	
Selective Availability (no longer active)	10	
Troposphere	1	
Ionosphere	10	
Pseudo-Range Noise	1	1
Receiver Noise	1	1
Multi-Path	0.5	0.5
RMS Error	15	1.5
Error @ PDOP = 4 (typical)	60	6

**Table 4.2.1:** GPS error sources

### GPS processing

As we learned, each satellite transmits signals on two sinusoidal carrier waves,  $L_1$  and  $L_2$ . Modulated onto  $L_1$  are two pseudo random noise codes, in RINEX (receiver independent exchange format) notation called  $C_1$  and  $P_1$  [Gurthner, 2000]. A second P-code,  $P_2$ , is modulated onto the  $L_2$  frequency.

Assuming the clocks in the satellite and in the receiver are both synchronized, the travel time signal can be determined by measuring the shift in between the internal and the incoming versions of the code in the receiver. The pseudo random noise codes are designed to have a low auto correlation allowing the shift to be measured precisely and without ambiguity. Multiplication of the transmission time by the speed of light gives the range between the satellite and the receiver. However, the time synchronizations between receivers and satellites are not perfect. Because of this effect and the influence of other error sources these ranges are called pseudo-ranges. It is possible to measure the carrier beat phase more precisely than the codes themselves, however integer ambiguities must be resolved for centimeter and better positioning. Both, phase and code measurements can be written in the form of pseudo-ranges. A phase pseudo-range (in meters) between receiver  $r$  and satellite  $s$  can then be expressed as [van der Marel, 1998]:

$$\phi_r^s = \|\vec{x}^s(t) - \vec{x}_r(t)\| + c\delta t^s(t) - c\delta_r(t) + I_r^s(t) + T_r^s(t) + M_r^s(t) + D_r^s(t) + \lambda N_r^s(t) + e_r^s(t) \quad (4.2.1)$$

with

$\vec{x}^s(t), \vec{x}_r(t)$  = vectors of satellite and receiver coordinates,

$\delta t^s(t), \delta_r(t)$  = satellite and receiver offsets from exact GPS time,

$I_r^s(t)$  = apparent range error due to ionosphere,

$T_r^s(t)$  = apparent range error due to troposphere,

$M_r^s(t)$  = multi-path error,

$D_r^s(t)$  = antenna phase center offset and variations,

$N_r^s(t)$  = integer ambiguity,

$e_r^s(t)$  = noise in measurements,

$c$  = speed of light and

$\lambda$  = wave length of the signal.

Pseudo-ranges are simultaneously measured from a number of satellites. Measurements to at least four satellites are required to calculate a three-dimensional position because the receiver clock must also be estimated. This reduces to three if Doppler measurements are available. The data has to be checked and repaired for outliers and cycle slips. The least-squares algorithm is used to estimate the unknown coordinates of the receiver and other receiver related parameters of interest. Consequently, the observation equation has the form:

$$\phi = f(x_r, y_r, z_r, \Delta\delta t_r) \quad (4.2.2)$$

with

$\phi$  = pseudo-range measurement,

$x_r, y_r, z_r$  = receiver coordinates and

$\delta t_r$  = receiver clock offset.

This must be linearized using a Taylor's series expansion for the use in all least-squares algorithm:

$$\phi - f(x'_r, y'_r, z'_r, \Delta\delta'_r) = \frac{\partial f}{\partial x_r} \Delta x_r + \frac{\partial f}{\partial y_r} \Delta y_r + \frac{\partial f}{\partial z_r} \Delta z_r + \frac{\partial f}{\partial \delta_r} \Delta \delta_r \quad (4.2.3)$$

with

$x'_r, y'_r, z'_r, \Delta\delta'_r$  = a priori estimates and

$\Delta x_r, \Delta y_r, \Delta z_r, \Delta \delta_r$  = corrections to the a priori approximate values.

$\Delta x_r, \Delta y_r, \Delta z_r, \Delta \delta_r$  are the unknowns being sought.  $m$  measurements and  $u$  parameters are then represented in the linear matrix form:

$$\mathbf{v} = \mathbf{A} \mathbf{x} + \mathbf{w} \quad (4.2.4)$$

$m \times 1$     $m \times u$     $u \times 1$     $m \times 1$

where  $\mathbf{v}$  is a vector of least-squares residuals,  $\mathbf{A}$  the design matrix resulting from the functional model which relates the observations to the unknown parameters being sought,  $\mathbf{x}$  is the vector of unknown parameters (corrections to the a priori estimates) and  $\mathbf{w}$  is the vector of computed minus observed measurements. A  $m$  by  $m$  variance-covariance matrix  $\mathbf{C}_l$  is constructed based on the stochastic model which describes the statistical behavior of the observations in the context of the mathematical model. The diagonal elements of  $\mathbf{C}_l$  are the variances  $\sigma^2$  of the measurement. The least squares optimized estimates for the parameters are then obtained by iterating:

$$\hat{\mathbf{x}} = -(\mathbf{A}^T \mathbf{P} \mathbf{A})^{-1} \mathbf{A}^T \mathbf{P} \mathbf{w} \quad (4.2.5)$$

where  $\mathbf{P}$  is the weight matrix, defined as the inverse of the covariance matrix  $\mathbf{C}_l$ .

The variance-covariance matrix of the least-squares estimates is obtained via [Mikhail, 1976]

$$\mathbf{C}_{\hat{\mathbf{x}}} = \sigma^2 (\mathbf{A}^T \mathbf{P} \mathbf{A})^{-1} \quad (4.2.6)$$

with

$$\sigma_0^2 = \frac{\mathbf{v}^T \mathbf{P} \mathbf{v}}{(m - u)}$$

The mathematical and stochastic model are critical to parameter estimation. The task of the mathematical model is to account for systematic errors in the observations whilst the stochastic model describes their random nature. Failure to correctly model the systematic biases will result in inaccurate coordinates. Inadequately modeled random errors can cause difficulties in the ambiguity resolution. Unfortunately many of the error sources listed are difficult to model, especially if the GPS antenna is moving. The most widely known processing method is differential positioning (DGPS). Other techniques as the employment of linear combinations of the code or phase measurements are used as well to estimate some sources of errors. For more detailed information see Hugentobler [2001].

#### 4.2.2 Deriving accelerations from GPS

In our special application, GPS plays a fundamental role. It is used to determine the aircrafts velocity and acceleration to reduce the total measurement of the gravity meter to a gravity disturbance or anomaly. Bruton et al. [1999] provided investigations about different methods to differentiate high-precision GPS phase observations to gain Doppler effect that are then used for aircraft acceleration determination. This approach has been considered advantageous because the resulting signal is less noisy than the raw Doppler effect. Starting from low order Taylor approximations, Fourier series and Remez differentiators, these filters are tested for their quality in reducing raw aerogravimetry measurements. All these differentiators are basically finite impulse response (FIR) filters with a linear phase and a reduced Gibb's phenomenon. The results show that the aircraft position and acceleration can be determined slightly better using the derived Doppler effect rather than the raw Doppler (see table 4.2.2). Currently, the GFZ aerogravimetry and GPS software uses 90 s filters and raw Doppler values. Depending on new GPS programs and receiver technology available, this might change in the future.

Results of 4 Flights: Gravity Disturbance Estimation Errors [RMS in mGal per Flight]				
Doppler Type	15 s Filter	30 s Filter	60 s Filter	90 s Filter
Raw	69.6 to 52.6	18.7 to 13.2	6.8 to 4.0	4.0 to 2.4
1 <sup>st</sup> Order	170.1 to 128.1	27.0 to 16.5	4.5 to 3.2	3.5 to 1.8
3 <sup>rd</sup> Order	54.5 to 36.1	15.0 to 9.4	4.1 to 2.8	3.5 to 1.8
49 <sup>th</sup> Numerical	54.5 to 36.1	15.0 to 9.4	4.1 to 2.8	3.5 to 1.8
49 <sup>th</sup> Optimal	54.6 to 36.1	15.0 to 9.4	4.1 to 2.8	3.5 to 1.8

**Table 4.2.2:** 1<sup>st</sup> and 3<sup>rd</sup> order differentiation versus 49<sup>th</sup> design filters, see Bruton et al. [1999]

In order to estimate the results of Bruton et al. [1999] for aerogravimetry applications Fig. 4.2.6 illustrates the GPS derived acceleration over the minimum resolvable gravity amplitude spectrum published by Schwarz and Li [1996].

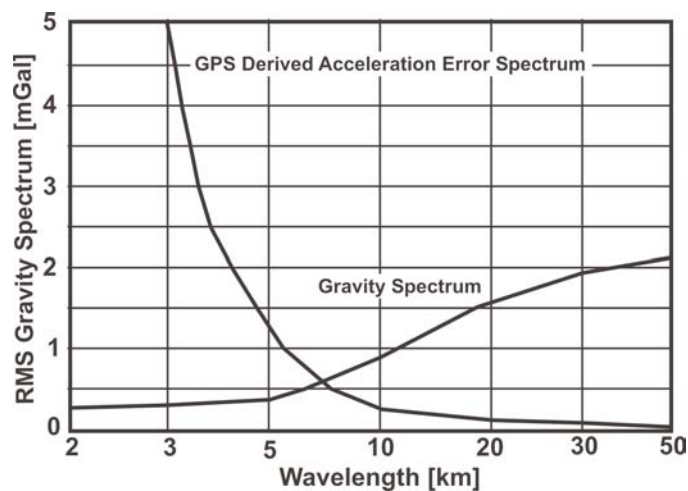


**Figure 4.2.6:** GPS acceleration error versus minimum detectable gravity

In a next step, Bruton et al. [2002] determined the effect on the aircraft accelerations derived via GPS using different recent GPS processing software packages. Depending on flight conditions the GPS error in gravity for a 90 s filter estimates from 1.1 mGal to 3.7 mGal.

### 4.3 Laser Altimeter

The laser performed well over all water surfaces at even more the 800 meters altitude when no fog or clouds were in the way. Problems were detected with the laptop that controlled the laser. It could not handle the vibrations in the aircraft and had to be often rebooted. Another problem occurred with triggering. The laser readings have no internal time stamps. Even when external triggers are applied, these triggers are ignored when a measurement fails due to low signal quality. This apparent bug for our application was fixed by Riegl©. After changing the measurement program please note that is mandatory to choose to trigger period that is bigger (not equal!) to double the measurement cycle time.

All figures, descriptions and technical data of this chapter are supplied by Riegl, Austria.

#### 4.3.1 Theory of operation

An electrical pulse generator periodically drives a semiconductor laser diode sending out infrared light pulses, which are collimated by the transmitter lens. Via the receiver lens, part of the echo signal reflected by the target hits a photodiode, which generates an electrical receiver signal. The time interval between the transmitted and received pulses is counted by means of a quartz-stabilized clock frequency. The calculated range value is fed into the internal microcomputer that processes the measured data and prepares it for range (and speed) display as well as for data output.

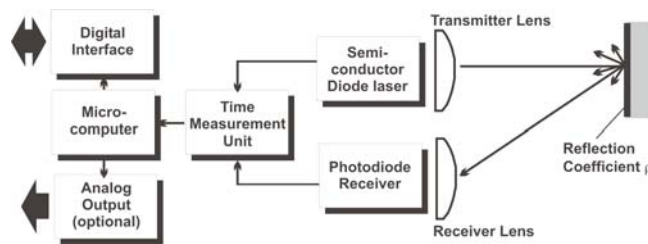


**Figure 4.3.1:** Principle of operation for a laser altimeter

The Riegl® last pulse distance meters enable laser range measurements even under conditions of bad visibility. Generally spoken, the distance meter provides the range of the last target, even if the measuring beam partially hits or penetrates other targets before. Thus, the technique is addressed as last pulse detection.

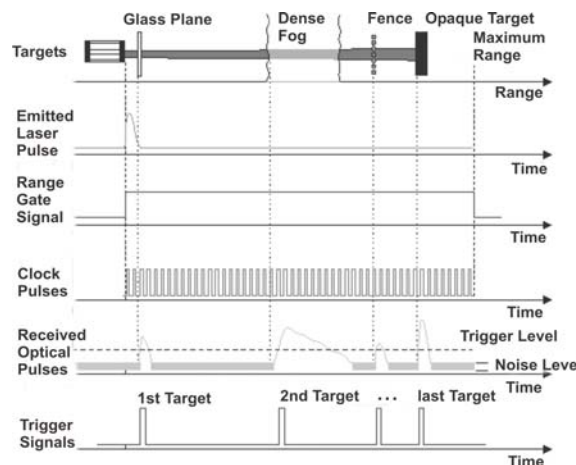


**Figure 4.3.2:** Last Pulse Detection

Fig. (4.3.2) shows a typical situation (1) where the emitted laser pulse (2) first travels through a glass pane, then penetrates a cloud of dust or fog, afterwards e.g. a wire fence, and finally hits the last, solid target.

*Diffuse reflection*

The signal is reflected omni-directionally according to Lambert's cosine law.

*Mirror-like reflection*

The angle of the reflected beam with respect to the targets surface is equal to the angle of incidence. Incident beam and reflected beam lie in the same plane.

*Retro reflection*

The retro reflected beam is returned in the same direction from which the incident beam came. This property is maintained over a wide range of directions of the incident beam.

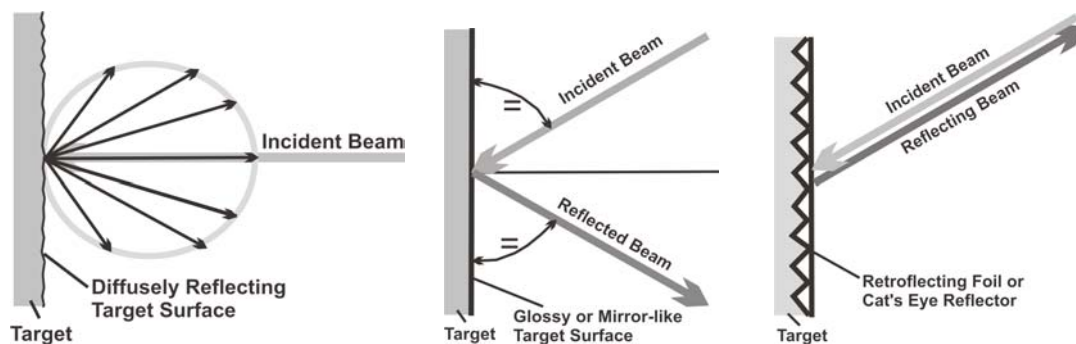


**Figure 4.3.3:** Diffuse reflection, mirror-like reflection and retro-reflection

An overview of diffusely reflecting surfaces / materials for a wavelength of about 0.9 micrometers is given in Table 4.3.1.

Material	Reflectivity
White paper	up to 100%
Dimension lumber (pine, clean, dry)	94%
Snow	80-90%
Beer foam	88%
White masonry	85%
Limestone, clay	up to 75%
Newspaper with print	69%
Tissue paper, two ply	60%
Deciduous trees	typ. 60%
Coniferous trees	typ. 30%
Carbonate sand (dry)	57%
Carbonate sand (wet)	41%
Beach sands, bare areas in dessert	typ. 50%
Rough wood pallet (clean)	25%
Concrete, smooth	24%
Asphalt with pebbles	17%
Lava	8%
Black neoprene	5%
Black rubber tire wall	2%

**Table 4.3.1:** Selection of material reflectivities

## 5 Central timing

This trigger and time control instrument was not used in the way presented here for the test flights described. At that time, the Meinberg clock only was used for time synchronization of the strap-down airborne gravimetry system (SAGS). It soon became clear that it was essential to have a multi-purpose trigger system to ensure exact timing on board of the aircraft. For the future we aim to make as much instruments as possible within the aero-gravity instrumentation fit for external measurement triggering.

### 5.1 Theory of operation

#### *Meinberg clock*

The Meinberg clock that was used in AGFA is of the type Meinberg Funkuhr GPS166. It normally is used for spatially static high precision timing. When the instrument is started, a minimum number of four GPS receivers are searched for to determine a precise GPS time signal. When more than four satellites are available, the GPS time errors can be minimized by comparing the different GPS clocks and re-adjusting the clock errors. If the location of the Meinberg clock was changed considerably or the instrument was not used for some months, this procedure may take up to 20 minutes because the clock must then determine its new position and download the new set of ephemerides from the satellites. Once this is successfully accomplished, the procedure will only take a few minutes if the clock is newly started. The initialization procedure only can take place for a static GPS antenna. Before the aircraft starts moving, the initialization must be completed and the antenna must be switched off. Once a good static GPS timing is achieved, this signal is used to initialize and control an internal high quality rubidium quartz clock. The highest internal clock rate is 10 MHz. From that signal a pulse per minute and a pulse per second signal are derived. Furthermore 10 MHz, 1 MHz and 100kHz signals are generated for output. Moreover, two serial data strings provide ASCII data if requested.

#### *Time trigger system*

After the AGFA mission, the GPS166 clock was used as the central part of a time trigger unit. The 10 MHz output was used to generate different trigger pulses ranging from pulse per minute to 100 Hz triggers. The flanks of the trigger pulses can be switched to positive to negative, depending on the sensor application. When a trigger pulse is switched on, it is activated only at the next full GPS minute for better timing control. This applies as well to a sinusoid output with a frequency of 1 Hz and a phase accuracy of 1/1000 of a second that is lately used for the SAGS2.2 timing.

#### *Internal power supply*

The Meinberg clock has its own internal unbreakable power supply using re-chargeable batteries. This power supply is able to bridge power fails up to 30 minutes automatically. This feature ensure that the timing is still operable after switch from a ground power unit to engine power in airborne applications.

## 6 Strap-Down Airborne Gravimetry System SAGS-2.2 (BEK)

### 6.1 Theory of operation

#### 6.1.1 Introduction

After scalar airborne gravimetry has proven an operational tool for high-resolution gravity observations, strap-down techniques will enable an even higher spatial resolution and vector potential at reduced costs. Operational advantages are an improved and simplified handling on board the aircraft and significantly less volume and weight of the instrument in comparison to conventional systems. Among several problems to be solved such as increased GPS positioning accuracy, improved signal processing, also the alignment and calibration problem has to be developed, if possible, as in-flight procedure as part of the observation mission.

SAGS is basically an assembly of accelerometers, which is strapped down to the aircraft without a gyro controlled stabilized platform. The referring sensors are approximately perpendicular, but in general we have to consider their signals as referred to a non-orthogonal set of three base vectors.

The observed acceleration is compared to kinematic accelerations derived from precise positioning, usually GPS. The difference provides the gravitation sought for. Depending on the algorithm used scalar gravity or vector gravity (where enhanced attitude quality is required) can be determined.

The basic equations of vector airborne gravimetry are given below. From these equations, algorithms for scalar gravimetry may be derived.

$$\delta g^n = R_b^n f^b - \ddot{r}_{eb}^n - (2\omega_{ie}^n + \omega_{en}^n) \times \dot{r}_{eb}^n - \gamma^n \quad (6.1.1)$$

with

$\delta g$  = gravity disturbance,

$R_b^n$  = attitude/rotation matrix,

$r_{eb}^n, \dot{r}_{eb}^n, \ddot{r}_{eb}^n$  = GPS position, velocity and acceleration,

$\omega_{ie}^n, \omega_{en}^n$  = earth rotation rate, transport rate,

$f^b$  = accelerometer output,

$\gamma^n$  = normal gravity.

#### 6.1.2 Accelerometer triad calibration

The accelerometer triad calibration has been carried out using standard procedures: The accelerometers are tilted at various angles. The gravity components acting along the sensitive axes are computed from tilt angles and the observations are fit to the computed gravity components by means of a model, similar to e.g. Lawrence [1998] p. 243, the 'IEEE-model':

$$\dot{a} = c_0 + c_1 \ddot{a} + c_2 \ddot{a}^2 + c_3 \ddot{a}^3 + c_4 \ddot{a}^4, \quad (6.1.2)$$

$$\underline{a} = \underline{K} \cdot \dot{\underline{a}} \quad (6.1.3)$$

with

$\ddot{a}$  = observed and scaled accelerometer observations,

$c_i$  = calibration coefficients for acceleration observations and

$K$  = matrix of non-orthogonalities.

The above model has to be complemented by parameters for accelerometer drift and errors of the test device. The non-orthogonalities provide a rotation from the non-orthogonal sensor base vectors to an ideal mean and orthogonal sensor frame. With the above model and procedure, a least-squares fit to the 1 mGal level has been achieved. Any accelerometer observation may be pre-calibrated with  $f$  and then standardized with the above procedure. Figs. 6.1.1 to 6.1.3 provide an impression of the tilt angle variation (down), which requires quite high angle observation accuracy over a wide range, acceleration observations in three components (middle) and model fit residuals (up).

In a second step, the ideal 3D-accelerometer sensor frame has to be related to the body frame of the aircraft. This shall not be pursued further in this paper. Disadvantages of this procedure are:

- The calibration is carried out in an environment different from the operational environment, e.g. with respect to vibrations, causing a constant offset through vibration rectification.
- The laboratory calibration admits a transformation to an ideal accelerometer sensor frame. Another step is required for the transformation to the body reference frame.
- Any change of sensor characteristics requires another laborious calibration.

For these reasons, in-flight calibration would be an advantage.

### 6.1.3 Attitude alignment and calibration

Let a set of airborne GPS antennae represent the body reference system. Because a 3x3 matrix may describe any 3D transformation including rotation and scaling without translation, we may use the relation

$$\mathbf{r}^b = \mathbf{R}_s^b \mathbf{r}^s \quad (6.1.4)$$

to formulate the transformation of a triplet of e.g. accelerations or rotation velocities as observed in the real sensor frame (s), to e.g. an orthonormal body reference (b) (forward / right / down). Of course, each set of sensors (rotation, acceleration) requires its own transformation to the unique body reference system. The transformation matrix  $\mathbf{R}_s^b$  may be interpreted in different ways, e.g. as rotation / stretch [Green, 1976].

In view of these options, there are various strategies:

#### a) Transformation of each sensor subsystem into a unique ideal sensor system

For the accelerometer subsystem, the calibration mentioned above includes such a transformation into an ideal orthogonal sensor frame. The advantage of such a procedure is the high potential accuracy of a laboratory calibration device. In a second step, this may be transformed into the body frame.

We have tested this strategy, using laser pointers installed in the SAGS for materializing the sensor frame and the antennae on the aircraft materializing the body frame and employing standard surveying methods.

The disadvantages are as follows:

- difficult realization of alignment transfer to body (aircraft) frame,
- loss of accuracy,
- vibrations during flight affect accelerometer signal (this is not taken into account in the observation of transformation parameters on the ground)
- wing flex and other aircraft deformation is not taken into account (it is estimated that this accounts for about 0.1°),
- the SAGS is strapped to the aircraft with intermediate dampers which allow about 2 mm amplitude resulting in about 0.3° (on the ground this is different from flight attitude).

b) Transformation of each sensor subsystem directly into the body reference frame

The problem presented here is not far from the problem in aero-photogrammetry. It is sometimes referred to as ‘image orientation’ or ‘direct geo-referencing’ etc. using INS/GPS integration (Cramer, 2001). Cramer did not use, however, multi-antennae GPS systems. The damping of cameras and INS systems is different from our case because of different goals for optimization. Usually, INS/IMU with a known internal calibration are used. The external alignment makes use of aero-photogrammetric procedures. For these reasons, strategies and results are not directly comparable.

The attitude of the 4-antennae configuration in the local navigation (north / east / down) frame is given by the A3DF-system and admits the transformation

$$\mathbf{r}^n = \mathbf{R}_b^n \mathbf{r}^b \quad (6.1.5)$$

where  $\mathbf{R}_b^n$  may be constructed from the Euler attitude angles  $\phi$  – *Roll*,  $\theta$  – *Pitch*,  $\psi$  – *Azimuth* .

We start from the equation

$$\mathbf{R}_s^b \boldsymbol{\omega}_{is}^s = \mathbf{R}_n^b (\boldsymbol{\omega}_{ie}^n + \boldsymbol{\omega}_{en}^n + \boldsymbol{\omega}_{nb}^n) \quad (6.1.6)$$

with

$R$  = rotation matrix,

$\omega$  = rotation velocity vector,

$i, e, n, b, s$  = inertial, earth, navigation, body, sensor.

For details of the quantities, consult Titterton and Weston [1997]. In the above equation, the numerical quantities are provided by the following sources:

$\mathbf{R}_s^b$  transformation from (non-orthogonal gyro) sensor frame to orthogonal body frame as materialized by the 4 GPS antennae, to be determined by least squares fit,

$\boldsymbol{\omega}_{is}^s$  angular velocity vector observed by gyros in their respective frames,

$\mathbf{R}_n^b$  orthogonal transformation from local navigation frame to body frame, elements provided by multi-antennae GPS attitude system,

$\boldsymbol{\omega}_{ie}^n$  earth rotation velocity in inertial space (‘earth rate’), coordinatized in local navigation frame and computed from GPS positioning,

$\boldsymbol{\omega}_{en}^n$  navigation frame rotation velocity with respect to the earth (‘transport rate’), coordinatized in navigation frame and computed from GPS velocity and finally

$\boldsymbol{\omega}_{nb}^n$  attitude rate, coordinatized in navigation frame and derived from multi-antennae GPS attitude system. In addition to the above equation, drift gyro drift rates are introduced.

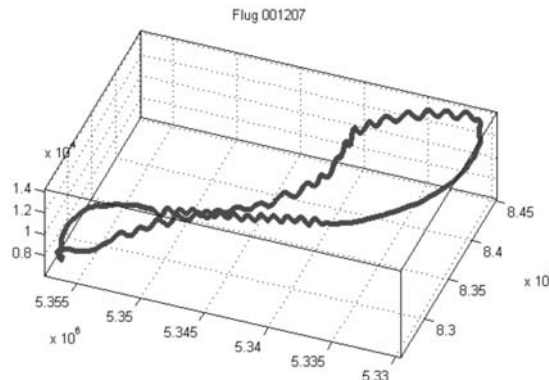


**Figure 6.1.1:** Spatial path of a SAGS test flight

In order to produce some signal, we applied some rotations to the aircraft about all three axes, see Figs.6.1.1 to 6.1.3.

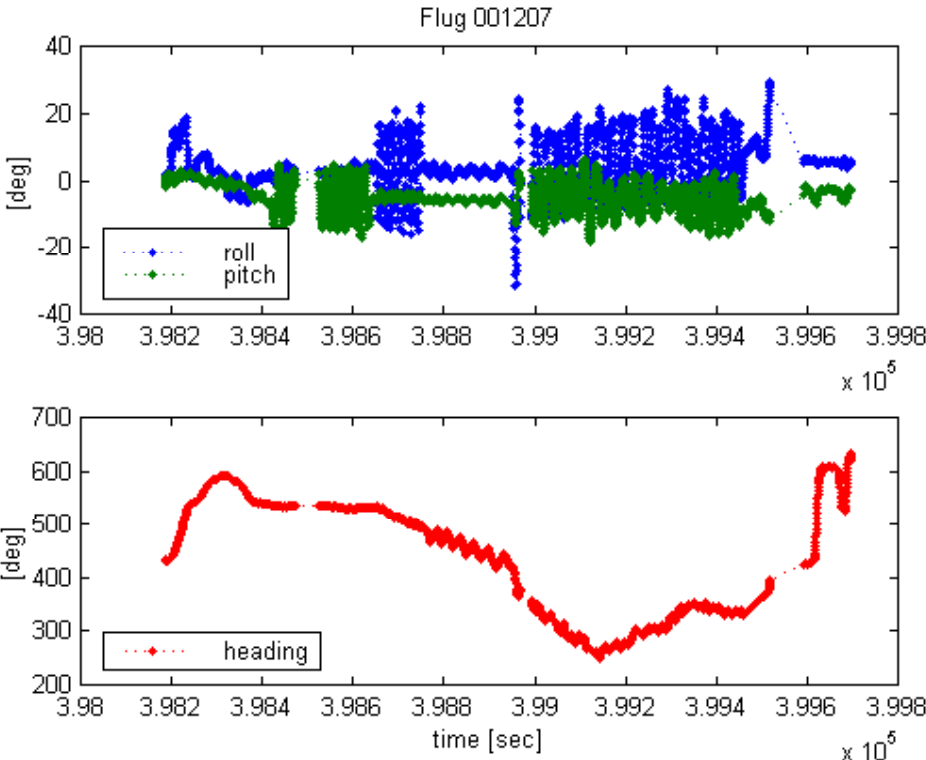


Figure 6.1.2: Pitch, roll and heading for the test flight

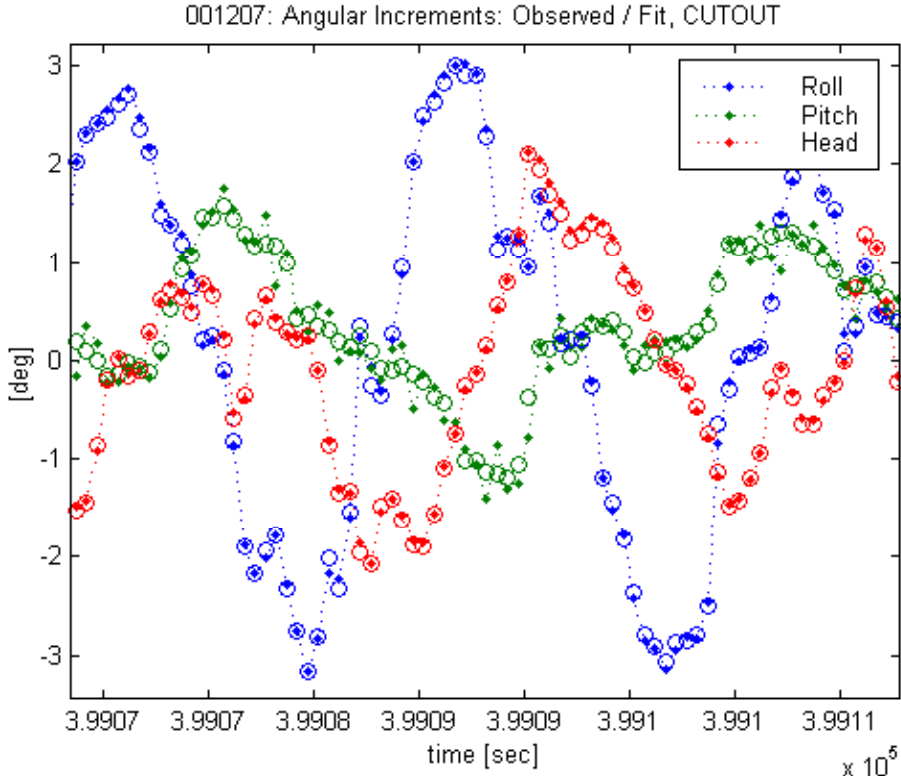
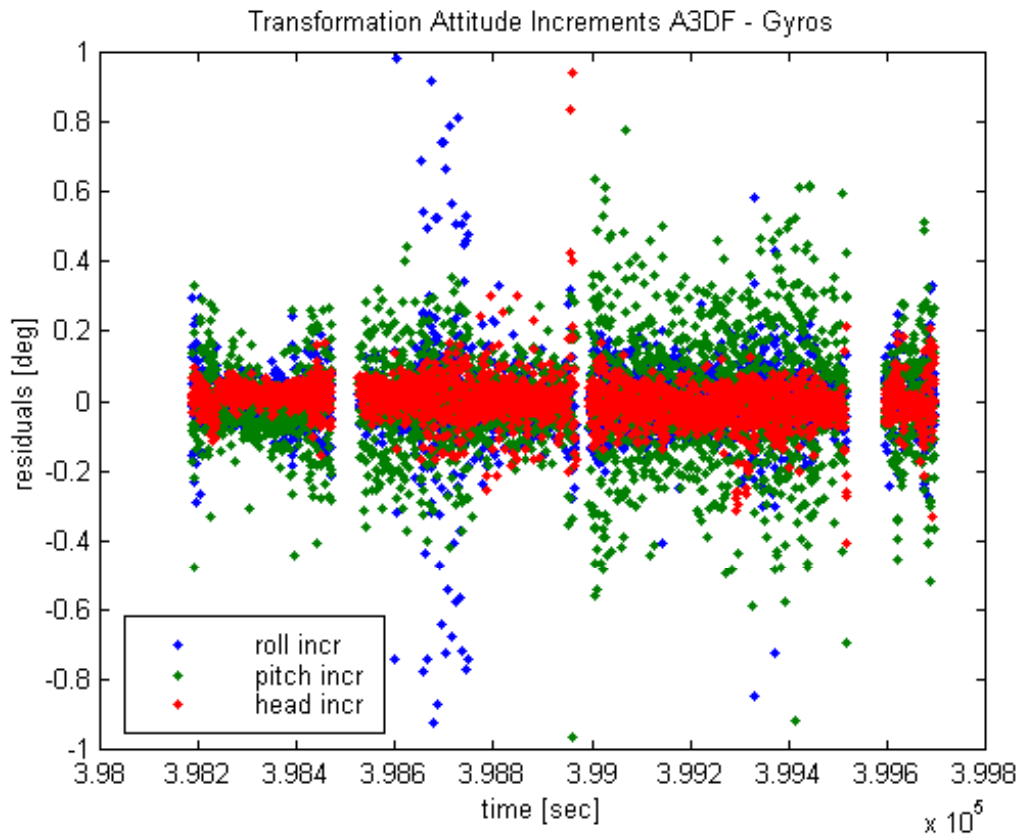


Figure 6.1.3: Pitch, roll and heading of the test flight in high resolution



**Figure 6.1.4:** Residual differences between the A3DF system and the gyros computed from test flight

The residuals of the least squares fit on the basis of the equation (6.1.6) are given in Fig. 6.1.4. The transformation matrix assumes the following numerical example values for  $R_s^b$  :

$$\begin{bmatrix} 0.9907 & 0.0244 & -0.0419 \\ -0.0198 & 1.0225 & -0.0735 \\ 0.0635 & 0.0986 & 1.0186 \end{bmatrix}$$

The variance-covariance matrix shows that any angular increment sensed in the sensor frame may be transformed to the body frame with an accuracy better than  $10^{-4}$ . This is the standard deviation of the mean transformation.

In the discussion of residuals, it has to be taken into account, that a GPS noise of 5 mm (in height) results in attitude (roll and pitch) noise of  $0.1^\circ$ . The vibration isolation of the SAGS with 2 mm vertical displacement results in  $0.3^\circ$  tilt. The quality of the transformation of any single observation of the SAGS to the navigation frame – and hence to a global reference frame – depends primarily on the quality of the gyros.

## 6.2 Technical description

We have demonstrated that the integration of a multi-antennae GPS attitude system and some low cost gyros provides a high accuracy for the rotation transformation between the sensor frame and the navigation frame – and hence any global reference frame. Another step will be the determination of calibration parameters also for the accelerometers by GPS observations. These in-flight calibration procedures are an important prerequisite for big operational advantages of strap-down airborne gravimetry.

### 6.2.1 Introduction

Other strap-down system developers in the field of aerogravimetry use off-the-shelf inertial navigation systems. These systems suffer from the handicap that they are optimized only to get the navigation and attitude solution precisely but not gravity. They are mostly not temperature controlled, therefore then have high drift rates and generally allow only limited access to the signal processing. Thus, an independent solution from INS packages was strived for. Within SAGS-2.2 Q-Flex accelerometers have been utilized. These sensors still have the best potential for gravity observations and are used as industry reference for acceleration measurements of all kinds. The integral Q-Flex electronics develops an acceleration-proportional output current providing both static and dynamic acceleration measurement. Through the use of a customer supplied output load resistor, appropriately scaled for the acceleration range of the application, the output current can be converted into a voltage. The QA-3000 includes a current-output and an internal temperature sensor. Through the use of a temperature-compensating algorithm bias, scale factor and axis misalignment performance is dramatically improved.

To reduce temperature and electromagnetic noise effects on the Q-Flex sensors special shields were tested and implemented in the SAGS housing. Additionally, a vibration damping platform to hold the housing was constructed. The SAGS control and data acquisition system was individually developed for this purpose running on a laptop using a MatLab environment.

### 6.2.2 Q-Flex accelerometer technique

In detail, SAGS-2.2 implements 3 Q-Flex® Quartz Accelerometer 3000 (QA-3000) within an airborne strap-down system to measure 3D accelerations resulting from gravity and kinematics (see Fig. 3.2.1). Primary applications of QA-3000 include spacecraft navigation and control systems. The QA-3000 features an etched quartz flexure seismic system. The proof mass is etched from a single piece of quartz to form an outer, stationary mounting ring and an inner pendulous disk. The disk is connected to the outer ring by two thin flexures or “hinges” (see Fig. 3.2.2). These flexures tightly constrain the proof mass and allow rotation only about the hinge axis. The amorphous quartz makes an ideal material from which to form proof mass and flexures, which are essentially perfectly elastic. There is no energy lost in their bending. The dimensional stability of the material also guarantees unchanging proof mass parameters as size and mass. It provides excellent bias, scale factor, and axis alignment stability.

The Q-Flex accelerometer combines advantages of fused quartz with solid-state servo electronics. Acceleration along the sensitive axis creates a force on the proof mass pendulum, displacing it slightly, causing a signal in a capacitive null detector. In response to this signal a servo circuit sends a current through coils attached to the proof mass. The current in these coils, moving through a permanent magnetic field mechanically restores the proof mass to the null or balanced position. The current required to re-balance the proof mass is proportional to

the input acceleration. The basic formula for the accelerometer output as a function of the acceleration input is [Allied Signal, 1997]:

$$\text{Output} = \text{Scale Factor} \times (\text{Acceleration along input axis} + \text{Bias}).$$

Please note that the scale factor and the bias depend also on temperature, axis misalignment and vibration. For more details on the Q-Flex accelerometers please refer to the Instruction Manual of Allied Signal [1997].



**Figure 6.2.1:** Q-Flex Accelerometers (for scaling: diameter is about 4 cm)

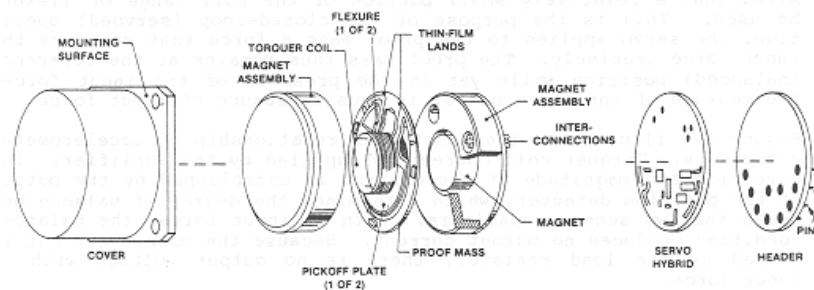


**Figure 6.2.2:** Q-Flex physical features

### 6.2.3 Temperature and other effects on SAGS

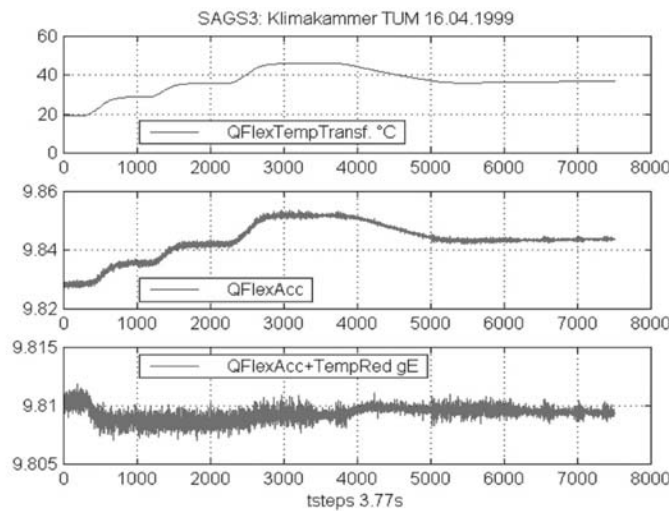


**Figure 6.2.3:** Temperature control of SAGS-3.0, a parallel model to SAGS-2.2

Very critical for performance and accuracy is the temperature control. A change of 0.01 °C of the ambient temperature causes a change of typically 1mGal in the acceleration measurement using the Q-Flex accelerometer. A complex correction model including e.g. the effects via the changing axes misalignments comes with the sensor to correct for this dependency. The SAGS-2.2 housing therefore is specially double-shielded and temperature controlled. By limiting temperature variations it is possible to reduce the complex correction model to a simple one. In a climate chamber a linear temperature model for the SAGS was determined (see Fig. 2.14). The temperature of the individual accelerometers is detected and stored parallel to the acceleration measurement. Remaining temperature variations are corrected for with the help of this model. To keep other disturbing environmental effects close to minimum influence, also magnetic and electromagnetic shielding has been developed and installed. With the help of this model remaining temperature variations are corrected for.

#### 6.2.4 Sensor configuration

The minimum configuration for strap-down airborne gravimetry systems would be one single accelerometer installed to measure in the approximate vertical component only. The next step to upgrade the system would be to add two tilt meters for the horizontal components. SAGS-2.2 holds the maximum configuration, three Q-Flex accelerometers in an orthogonal system with the best sensor mounted in the vertical component. This sensor was used in most of the GFZ aerogravimetric flights.

#### 6.2.5 Vibration damping

In an aircraft environment vibrations easily have much larger amplitudes than the gravity signal that is to be determined. They are comparable in amplitude to the aircraft kinematic induced acceleration with only a small frequency gap in between. The SAGS principle of measurement (meaning accelerometer reference, attitude and position reference have a fixed relation) does not allow high damping ranges (below 5 mm). It is still a difficult task to design an optimized vibration damping platform that suits a range of different aircraft.

#### 6.2.6 Signal processing

Three different acceleration signal sources merged have to be processed by SAGS: vibration, aircraft kinematics and the gravity field. As discussed above, vibrations are physically damped by the platform design. The lasting signal is measured by the Q-Flex accelerometers and analogue-filtered. The filtered signal can either be digitized by a frequency counter or by an analogue-to-digital converter. The derived signal on each way now can be filtered digitally and reduced by the accelerations computed from the GPS-signal from aircraft antennas.

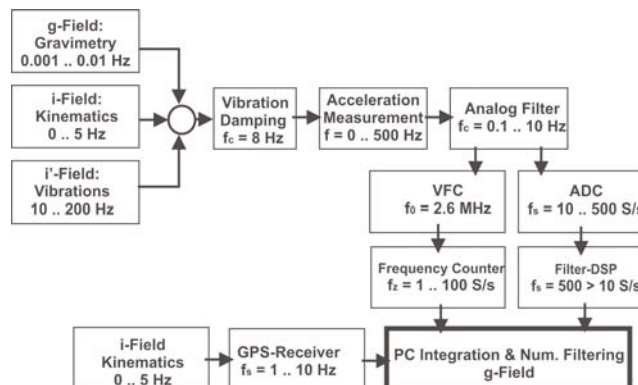


Figure 6.2.4: Signal flow

## 7 The aircraft: DLR Cessna Grand Caravan

All data, descriptions and figures given in this chapter and in section 11.9 are courtesy of DLR Oberpfaffenhofen.

### 7.1 General Description

The Cessna Grand Caravan is an un-pressurized single-engine high wing turboprop with fixed landing gear. The aircraft can accommodate up to 14 persons including a minimum crew of one. (Operations with more than nine passengers are limited to countries that issue a FAR Part 23 nine passenger limit waiver). Suitable allowance for luggage and optional equipment is also provided.

The power plant is a Pratt and Whitney of Canada PT6A-114A turboprop engine mounted in the nose of the airplane fuselage.

Certification basis is to U.S. FAA FAR Part 23 Requirements; day, night, VFR, IFR and flight-into-icing conditions are allowed when equipped with the appropriate options.

### 7.2 Special DLR Modifications

#### *Fuselage*

Two ports in the floor are provided to install cameras, scanners or other instruments. So each port has the length of approximately 675 mm; the usable width between the seat-rails is 630 mm. Two further small holes (diameter each min. 150 mm) can be used to install a NAV-sight or other small instruments. There are also two small holes ( $\varnothing$ 150 mm) in the cabin-top opposite the large camera-ports for installation of antennae or other small and light sensors. To protect the port-mounted instruments and cameras the ports are equipped with sliding doors outside.

#### *Wing*

To perform the installation of external stores (i.e. PMS or certain pods) left and right wing-hard points will be installed. These points are close to the wing strut and allow carrying 120 kg on each side.

#### *Electric Power*

The aircraft's electric system will provide a maximum electrical power of maximum 200 amps at 28V DC. Conversions to 220 VAC and 115 V / 400 Hz are available on request.

The power distribution-panel is situated left side mid cabin and provides 4 Sockets fused with 50 amps and 4 Sockets fused with 20 amps (28 VDC).



Figure 7.1: DLR Cessna Grand Caravan

## 8 The Software: GPS, Aerogravimetry, Geoid

### 8.1 Kinematic DGPS-software

The most significant reduction on the airborne gravity signal is the subtraction of the aircraft's acceleration. Any error or uncertainty in the post-processed kinematic DGPS solution will directly affect the quality of the aerogravimetric measurement. Therefore, careful kinematic DGPS processing is mandatory. Here we will give only a short overview about the programs used, details of GPS processing are described in chapter 2.4 and will be subject of later reports.

#### 8.1.1 Kinematic GPS software for AGFA

The GPS software mainly used for aerogravimetry data processing within the ANGEL projects is GeoGenius<sup>®</sup>. GeoGenius is a commercial software package used for static and kinematic GPS processing. It is also able to include geodetic leveling and laser distance measurements. Its preceding version (GeoTracer<sup>®</sup>) was successfully used during the AGMASCO project for GPS computations. GeoGenius is easy and fast to handle even on laptops and in the field.

Within GeoGenius, at first for each land based GPS reference a single point solution is calculated. This new, enhanced position in space is then combined with the raw data of the station in use. When a set of ground references is available with time parallel measurements a differential GPS network solution can be computed. The results of the network fixing will once more improve the reference positioning. The reference stations that cover the flight profiles best are then used for recovering the kinematic DGPS positions on the flight path of the aircraft. In practice, this means that the flight must be fully covered in time and that the baseline between ground reference and aircraft is at a minimum.

As most DGPS processing software tools, also GeoGenius has problems with a large number of small subsequent data gaps in the observations of the airborne GPS receiver. Therefore, by default all GPS raw data is converted into RINEX formatted files, which are then "repaired" by special GFZ developed programs using Lagrange interpolation. Programs as GeoGenius, GPSurvey or KSG-Soft, the latter a program developed at GFZ [Xu et al., 1998], can thereafter handle the „repaired“ files with significantly better results. Other small service programs that check the RINEX format and delete satellite observations of only a few minutes from the raw data are continuously developed.

#### 8.1.2 Latest kinematic GPS software for ANGEL

Recently, updates for the GFZ software KSG-Soft were developed and tested. In the new version, the source code (language C) can be compiled and afterwards executed either on UNIX platforms or PC based systems. Only since this version is available, the software can be used in the field where only laptops are available with the ANGEL equipment. This enables much better quality control in the field by evaluating the results and comparing them to those of independent software. During the past years it became clear that GeoGenius held some internal bugs that made it i.e. impossible to process and monitor the data that was acquired in the southern Gulf of Mexico. Therefore, a new kinematic DGPS program as a counter part to KSG-Soft was obtained, Trimble Total Control. This software proved to be much more stable than GeoGenius both in data pre-processing and in the final results.

However, the aerogravimetry group is still developing secondary GPS software for RINEX conversion, re-sampling of data and data checks.

## 8.2 Aerogravimetry software

The core of the aero-gravity processing (AGP) software was developed during the AGMASCO project in 1997 by Arne Olesen at KMS in Copenhagen, Denmark. In 1999, Dag Solheim from the Statens Kartverk in Honefoss, Norway, translated the original Pascal version of the program into Fortran77. At GFZ, the Fortran software was adapted to the specifics of the LaCoste & Romberg S124b system and is continuously upgraded. The current software used at GFZ, AGS-124, is described in the subsequent paragraphs. Most of the theory, that was applied in our aerogravimetry processing program was already described in chapter 2.2. Therefore, we concentrate only on some few additional aspects of the program.

### 8.2.1 General overview

AGS-124 reads different types of data sets for processing; the minimum information is the LaCoste & Romberg raw gravity data and a flight path position file in Ashtech-C format or KSG output format. Other GPS post-processing formats may be added at any time. Both files usually cover the full length of the flight but only a limited time span representing a survey profile is compiled. The start and stop time information like other program parameters are defined in a parameter file. Each survey profile has its own individual parameter file. The program initiates the processing sequence by checks on the input data, and then calculates a time shift for best correlation of the data sets (that might occur due to time shifts in the different instrument clocks). The time left fixed is always the GPS time in the position file.

When the time shifts are cared for, the gravity corrections and reductions are applied. First of all, the Eötvös-effect is compensated for. Next, the cross-coupling errors are re-compiled and eliminated. Then, platform deviations from the vertical are corrected for. Finally, the data is once more low-pass filtered by RC- or Butterworth-filters, depending on the data quality and the time constants used for the gravimeter platform horizontation. At last, the total gravity reading is reduced by the aircrafts vertical acceleration (second time derivative of the aircraft altitude). Optionally, the result is further reduced for the normal gravity field and related to sea level, thus getting free-air anomalies instead of gravity disturbances. The final gravity data is compared to ground truth data as independent gravity information or geoid undulations when available. For an overview about the data processing, see Fig. 8.2.1.

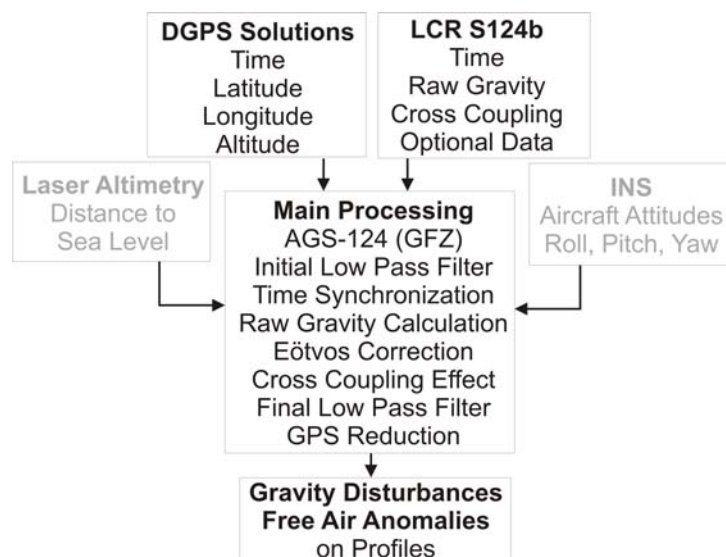


Figure 8.2.1: Aero-gravity data processing schematics

### 8.2.2 Synchronization of time series

One of the most important steps in aerogravity processing is to ensure the time synchronization of all time series involved in the data processing. Time errors mainly result from different or imprecise system clock settings. Usually, the GPS time series is held fixed and all other data sets are then shifted “along” the GPS data until the best correlation is found. Hereby, it is assumed that the GPS data series and the data series to be checked for time shifts have a first order correlation due to their physical nature (horizontal accelerations from GPS – accelerometers on top the gravity meter, vertical accelerations from GPS – raw gravity meter readings, etc.) The algorithm used in the GFZ aerogravity software is able to correct for time shifts with an accuracy better than 0,1 seconds assuming time shifts with no additional linear or non-linear drifts. This is the benchmark required for 10 Hz data.

The empirical correlation coefficient used is defined as [Bronstein & Semendjajew, 1979]

$$r = \frac{\sum_{i=1}^n (x_i - \bar{x})(y_i - \bar{y})}{\sqrt{\sum_{i=1}^n (x_i - \bar{x})^2 (y_i - \bar{y})^2}} \quad (8.2.1)$$

with

$x_i$  and  $y_i$  = i-th value of time series to compare and

$\bar{x}$  and  $\bar{y}$  = mean values of the time series  $x(t)$  and  $y(t)$ .

### 8.2.3 Eötvös correction

All types of gravity meters or accelerometers in general based on a moving platform are affected by their motion over a curved, rotating earth. The motion of a mass particle in a rotating coordinate system is expressed by the vector equation [Harlan, 1968]

$$\vec{a} = \vec{\ddot{r}} + 2\vec{\omega}\vec{\dot{r}} + \dot{\omega} \times \vec{r} + \omega \times \omega \times \vec{r} \quad (8.2.2)$$

with

$\omega$  = angular velocity,  $\vec{r}$  = radius vector.

This motion results in a centripetal acceleration, which must be corrected for. This correction, known as Eötvös correction, is defined by LaCoste [1967] as

$$E = (R_\phi + h)(2V_\phi V_e + V^2)/R_\phi^2, \quad (8.2.3)$$

with

$$V^2 = V_e^2 + V_n^2,$$

$R_\phi$  = earth radius at latitude  $\phi$ ,

$h$  = height above sea level,

$V_\phi$  = speed of rotation of the earth surface at latitude  $\phi$ ,

$V_e$  = easterly speed component of the platform,

$V_n$  = northerly speed component of the platform.

For speeds less than 15 knots as in marine gravimetric surveys the correction can be simplified to [Dehlinger, 1978]

$$E = 7.503V \cos \phi \sin \alpha + 0.004V^2 \quad (8.2.4)$$

with

$\alpha$  = azimuth angle.

In the special case of speeds less than 15 knots the Eötvös correction is in the range of +50 mGal to –50 mGal. In the case of aircraft speeds it is in the range of +1000 mGal to –1000 mGal. Therefore, a more precise expression for the Eötvös correction is necessary to avoid errors on the final gravity results from airborne platforms. Harlan [1969] developed a suitable form to correct for the Eötvös effect on aircraft measurements:

$$E = V^2/a (1 - h/a - \varepsilon(1 - \cos^2 \phi(3 - 2\sin^2 \alpha))) + 2V\omega_e \cos \phi \sin \alpha \quad (8.2.5)$$

with

$\varepsilon = V^2/a \sin^2 \phi + 4V\omega_e \cos \phi \sin^2 \phi \sin \alpha$  and

$\omega_e =$  angular velocity.

The formula from Harlan is used in the AGS-124 program. It is clearly visible, that errors in navigation have a large impact in the Eötvös correction. Consequently, only the best possible navigation solution should be used for airborne gravity correction.

#### 8.2.4 Vertical Accelerations

No gravity sensor can distinguish between gravity and platform acceleration. Therefore, any raw, relative scalar “gravity” measurement on a moving platform is actually the addition of the vertical acceleration and the change in gravity:

$$g_{raw} = g + \ddot{z}. \quad (8.2.6)$$

Furthermore, in an airborne environment instantaneous vertical acceleration are generally 10000 to 100000 times greater than both the expected variation of the gravity signal and the accuracy of the gravity meter. It is therefore mandatory to filter the data. The amount of filtering required is highly dependent on the quality of the meter, the quality of the platform and the quality of the flight performance. Due to the problems described, the gravity meter response and the filter response both must be extremely linear and stable in phase to avoid artifacts in the filtered and acceleration reduced gravity (see also chapter 3.2.1 for the discussion of non-linear effects of the LaCoste & Romberg S124b meter).

In our case,  $\ddot{z}$  is derived by simple differentiation. The filter used in the program is either an RC-filter as used with the current version of the LaCoste & Romberg S124 meter or a Butterworth-Filter with adjustable stages and filter lengths. For the future a FIR-filter is planned to be implemented using a “Mexican hat” shape as it is realized with the fully digital upgrade of the meter.

### 8.3 Geoid modeling software

Recently, a geoid processing software, AGF-4.2, developed on behalf of the GFZ was successfully tested and installed. The intention of the AGF-4.2 program is to construct a regional geoid on the basis of airborne and / or surface data using different mathematical approximation methods. In particular, variations of the collocation method and dipole-fitting algorithms are realized. The software is able to handle different input data as absolute measurements, free-air anomalies or gravity disturbances. The software and an application to airborne gravity data is already well documented in Marchenko et al. [2001].

## 9 Test flight data

### 9.1 Introduction

Two different test areas were chosen for the aerogravimetry system tests, the Bavarian Alps and the Rhine Graben. Over the Alps, the effect of turbulence and rough topography were to be investigated. The Rhine Graben was chosen to see how well long wavelength gravity anomalies can be recorded by the system. In order to evaluate the in-flight data, ground truth maps were generated. From these maps, the actual profile data were extracted by bi-cubic interpolation. In the following chapters, the ground truth data is presented and compared to the airborne results. The effects in the airborne gravity data and its quality are discussed.

All test flights were conducted from the airport in Oberpfaffenhofen using the DLR Cessna Grand Caravan. A GPS base station was set up at the same airport. For the flight over the Bavarian Alps, only this station was available because on this day the complete SAPOS (Satelliten-Positionierungsdienst der deutschen Landesvermessung) network broke down in Bavaria. Fortunately, SAPOS data were available for the flight over the Rhine Graben.

Both flights were conducted in the calm air of the early morning hours just after sunrise. Turbulence only occurred over hilly area to a moderate extent. Some mountain tops of the Bavarian Alps were passed only with a few meters ground clearance. This resulted in moderate turbulence but higher corrections in the flight altitude. The latter effect degraded the airborne gravity signal significantly during the moments of attitude corrections. These corrections were the only ones done by the pilots, on all other parts of the profile the autopilot was active. The autopilot was controlled by ambient air pressure for height correction (constant barometric altitude) and GPS for course and heading. The constant barometric altitude is the smoothest flight level available, therefore this option was chosen for the aerogravimetric profiles.

At this point, it is necessary to explain the airborne gravimetry result figures in more detail. As an example, we take Fig. 9.3.1. The result figure is divided into eight boxes. The upper three boxes show the most important parameters derived from the sensor to compute the gravity signal (see equation 3.1.1). The uppermost box will be referred to as box1, the lowermost one as box 8. Box 1 displays the unscaled, unfiltered and filtered spring tension variation of the meter along the profile. The filter setting is always given in the plot titles. We always observe a smooth variation in the spring tension setting due to system internal filtering applied on this feedback loop. Box 2 shows the unscaled beam velocity both filtered and unfiltered. The unfiltered beam velocity peaks are 10 to 100 times higher than the filtered version. This problem was discussed in section 2.2.1 resulting where it was shown that low-pass filtering of this data is mandatory before reducing it with GPS data (which of course has to undergo the same filtering). Box 3 shows the unfiltered and filtered cross coupling correction in mGal (including level corrections, see section 3.2.1). Box 5 displays the aircraft attitude in terms of pitch and roll angles as well the heading (course towards geographic north). Box 6 shows the vertical accelerations, both from GPS and the gravity meter on the flight level. The difference in between both signals is the gravity disturbance due to the earth's gravity variations at the flight level. Depending on the reduction level, either the free-air anomaly or the gravity disturbance is displayed in box 7. Moreover, box 7 shows the direct comparison to the unfiltered and filtered ground truth data, the flight level and the topography. If available, aero-magnetic data are also plotted in the same box. The last box indicates data gaps marked in different colors for different data sets. In Fig. 9.3.1 some INS data is missing. More principle details of the sensor handling and performance are discussed in sections 9.3 and 9.5. All free-air anomalies shown are downward continued from the flight height using the normal gravity gradient of WGS84.

## 9.2 Ground-truth data: southern Bavaria and the German Alps

The area of southern Bavaria and the German Alps (including the northernmost part of Austria) is covered by datasets obtained from Bureau Gravimétrique International de Toulouse (BGI) and from the Deutsches Geodätisches Forschungsinstitut in Munich (DGFI). The BGI data was received in two sets: the first set included German data only (2199 points); the second set also contained Austrian data after public release (5103 points, partly overlapping the first set). The BGI data was delivered using the standard BGI land gravity data format with all standard reductions included. The DGFI data set (5780 points) supplements the BGI data significantly. It was delivered using Gauss-Krüger-coordinates that were transformed to latitude and longitude for GMT-mapping. The gravity data included in the DGFI set was converted into the same system as used by BGI. For ground truth map production, 10900 data points out of the combined data sets were used (statistically 0.3 points per square kilometer).

Fig. 9.2.1 shows a map of topographic heights compiled from height information given with the gravity data sets. Fig. 9.2.2 shows the topographic map as generated from ETOPO'2 data. A comparison of both topographic maps show that the ETOPO'2 data is slightly smoother in the Bavarian Alps and that the Austrian part of the Alps is not well covered with gravity data. This comparison is used to give an idea of the quality of the derived ground truth gravity maps. The small spots in the maps represent gravity stations combined with height information. Nevertheless, the flight track profile can be extracted with a satisfactory amount and quality to allow the comparison with the airborne gravity results. Fig. 9.2.3 shows the free-air anomaly map that was used for ground truth comparison.

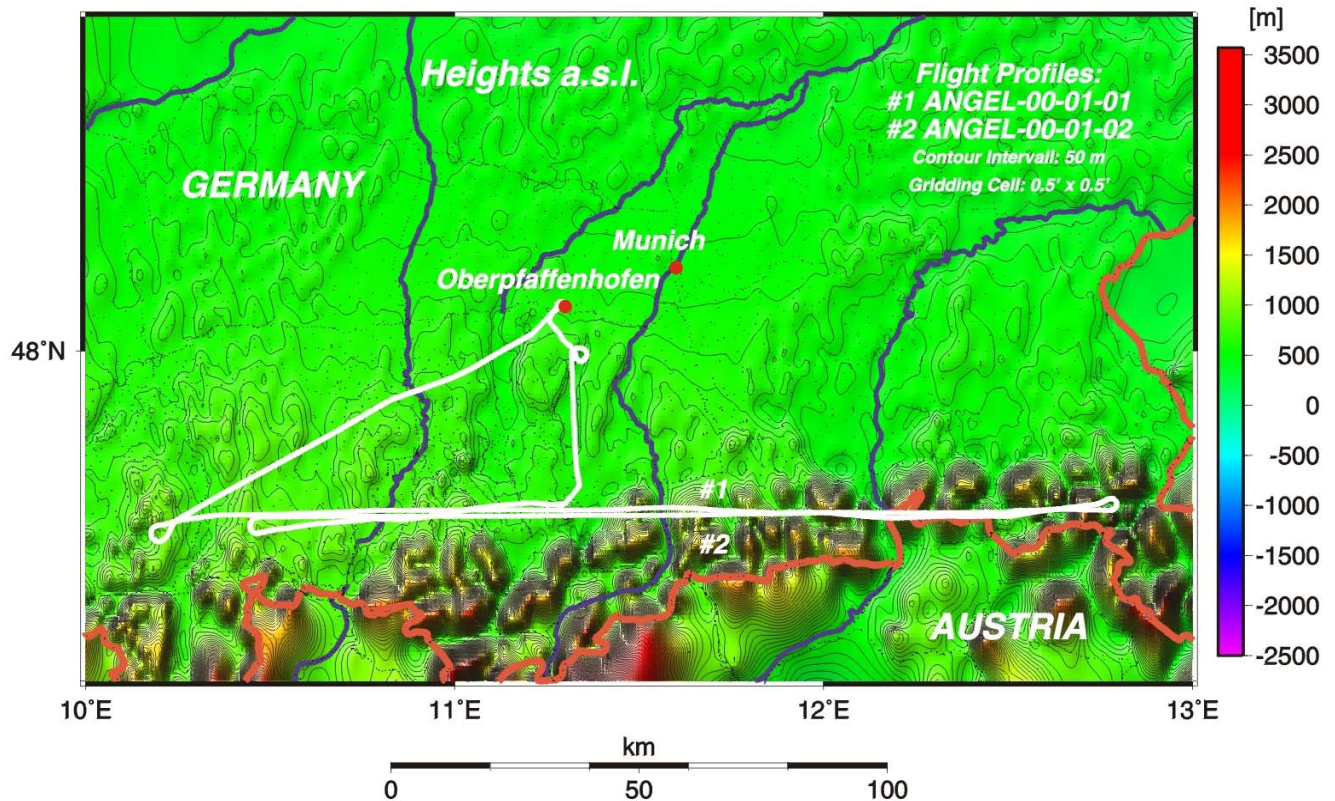


Figure 9.2.1: Height map of the Bavarian Alps derived from the BGI and DGFI data sets

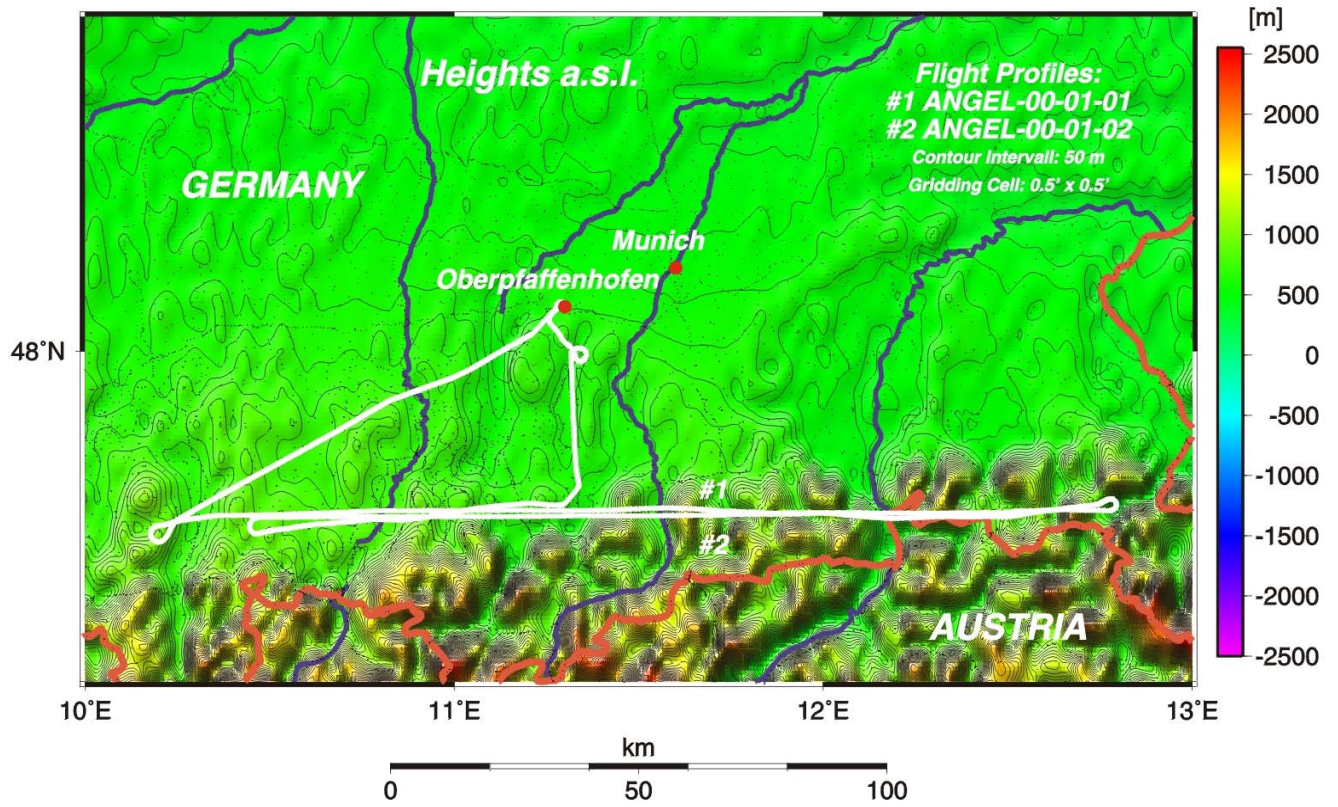


Figure 9.2.2: Height map of the Bavarian Alps derived from ETOPO'2 data

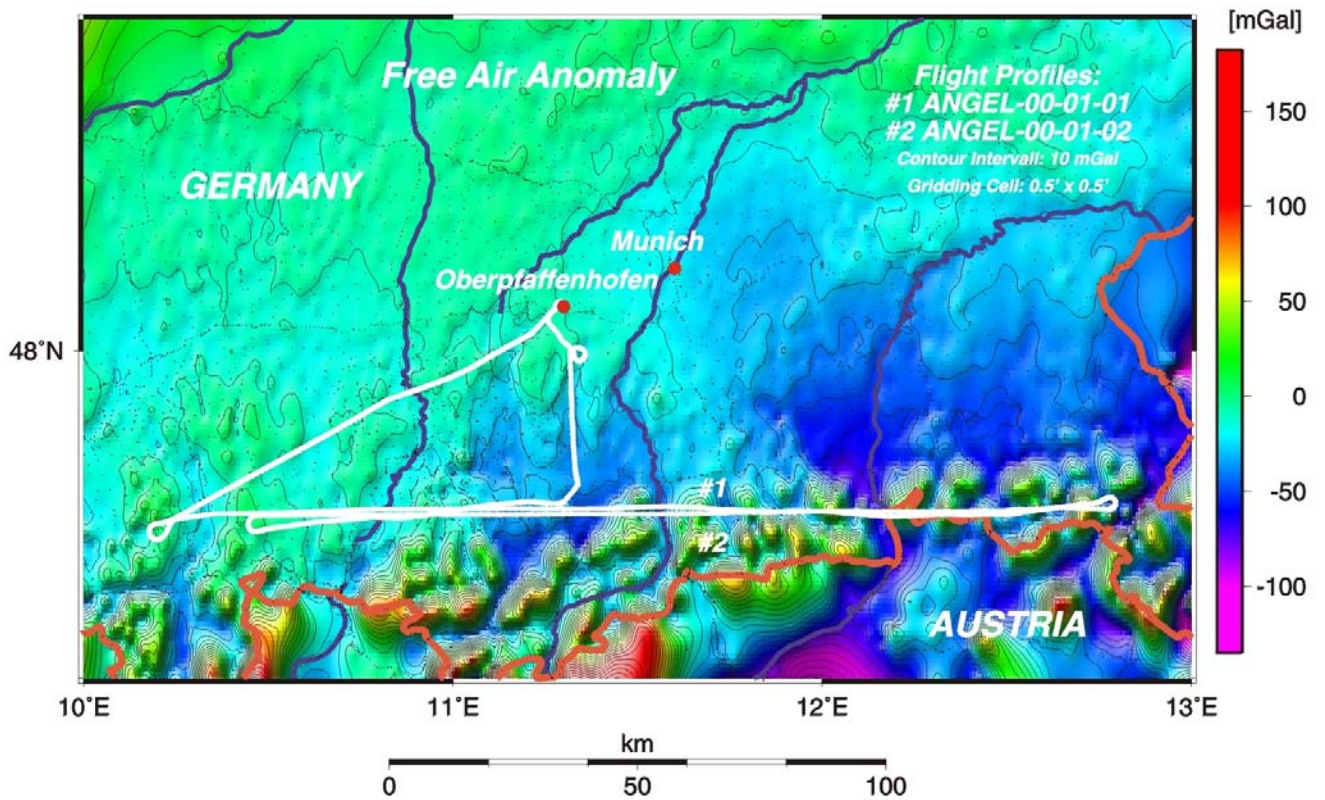


Figure 9.2.3: Free-air anomaly map of the Bavarian Alps derived from the BGI and DGFI data sets

### 9.3 Airborne data: Bavarian Alps

As already stated, the airborne gravimetry data processing for the profiles over the Bavarian Alps suffered from an unfortunate event: on the day of the flight, May 23<sup>rd</sup> 2000, the same day a SAPOS (Satelliten Positionierungsdienst der deutschen Landesvermessung) symposium took place in Munich, the complete Bavarian SAPOS network broke down. Therefore, only a single ground GPS reference was available for kinematic DGPS processing: the GFZ station at the DLR in Oberpfaffenhofen. This event has some degrading effect on the quality of the GPS data that is further from the base station.

Thus, for data processing only a single point solution was computed for the GPS site in Oberpfaffenhofen and then was used as a reference. Moreover, the airborne GPS receivers suffered some satellite signal losses due to the roll angles of the aircraft. This especially affected the Ashtech antenna on board. Some spline interpolations to bridge GPS data gaps were developed to fix this problem. In the end, the result was not perfect, but still satisfying.

We will first discuss Fig. 9.3.1. This figure holds more information than usually displayed for aerogravimetric profiles because the effects of sensor handling and filter edges are shown and briefly discussed as well.

At 100 seconds, the sensor beam was “unclamped”, meaning the latch to hold the sensor fixed was released after reaching the profile onset (see attitudes in box 5). The effect of the unclamping is clearly seen in the gravity response. From this moment onwards, the beam was free to swing and react to vertical acceleration responses. We now observe that the spring tension, that was not pre-adjusted for this purpose, slowly moves to a stable level. The effect (translating to a half-wavelength resolution of 4.8 km at 120 kts ground speed) of the beam release is overlain by the filter edge effect of the 80 seconds, 3 stage Butterworth filter. This effect is most prominent in the beam velocity and the cross coupling. The platform period was set to 4 minutes. Two platform periods (480 seconds) after the beam release, the gravity signal becomes stable and matches the ground truth data well. At about 1700 seconds a “pitch dump” was provoked and at about 2600 seconds a strong “roll dump” was experienced. A pitch dump is a fast aircraft movement that forces the nose down and then up again and therefore introduces an additional large vertical acceleration of the platform. As expected, after this “shock wave” the platform needs about one platform period to recover, the gravity error signal is transformed to a wavelet like form due to the Butterworth filter. After the platform recovery, the airborne sensor starts to pick up the gravity signal again until it is once again disturbed by a strong roll maneuver through a right wing dip followed by some more turbulence.

The errors included are a test of the recovery time of the platform which all lay in the expected time frame. The fact that in the second part of the profile the matches to ground truth are less obvious are due to lack of data on the higher mountains and ground truth interpolation errors and the degrading GPS quality for vertical acceleration reduction. Finally, note that data were filtered with a very small low-pass window just at the very edge of gravity meter platform performance. Normally, a 120 second filter of the same type is used with our meter (resulting in a half wavelength resolution of 8.4 km).

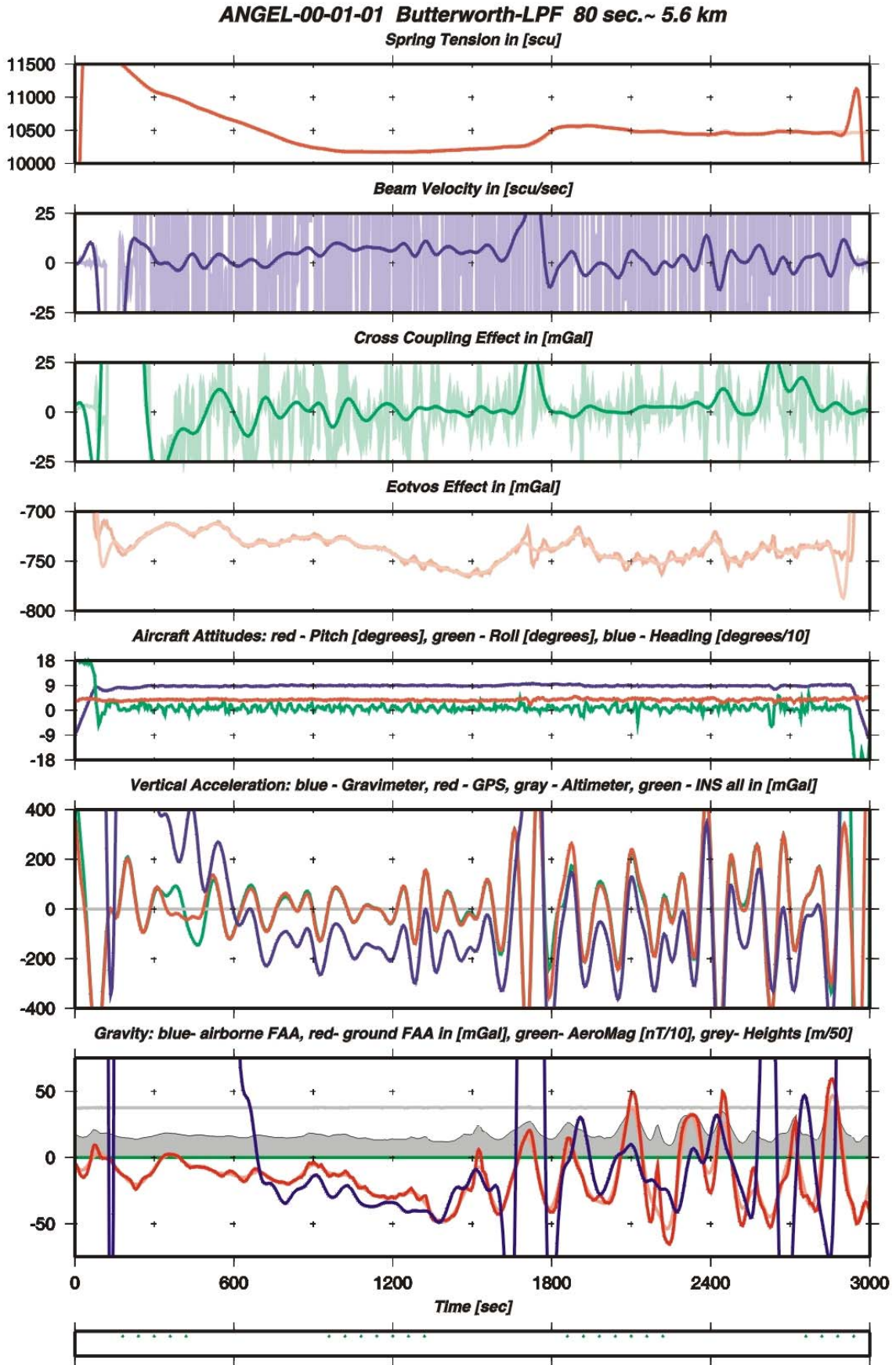


**Figure 9.3.1:** Bouguer anomaly map of the Bavarian Alps derived from the BGI and DGFI data sets

## 9.4 Ground truth data: Rhine Graben

The area of the central Rhine Graben displayed in figures 9.4.1 to 9.4.3 is covered by two major gravity data sets. The first data set was obtained from BGI in Toulouse. It consists of 8805 point measurements.

Unfortunately, this data set only included very sparse data in Germany west of the Rhine. Therefore, a second data set to complement the BGI data was necessary. This data was obtained from the GGA in Hannover. Their data set holds 5826 data points that nicely covered the aforementioned region of poor data coverage. Altogether, 13151 data points were used for mapping the heights, free-air anomaly and Bouguer anomaly of the area. Statistically, the map is covered by 0.15 data points per square kilometer. There were no problems detected when merging both data sets. The comparison between the ETOPO'2 topography map and the one derived from the heights from the gravity data files are in good agreement. Therefore, we concluded that the free-air anomaly map is representative of the area and can be used for comparisons of extracted ground truth and airborne results.

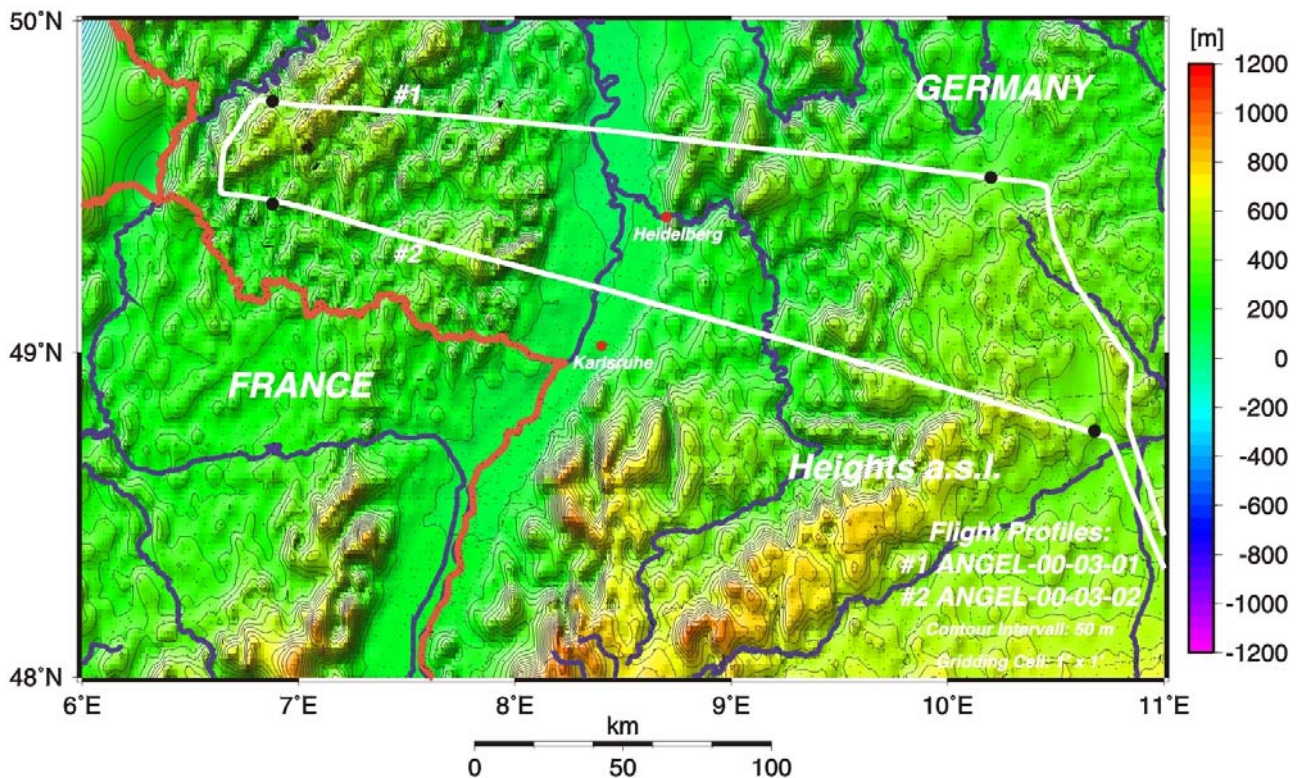


Figure 9.4.1: Height map of the Rhine Graben area derived from the BGI and GGA data sets

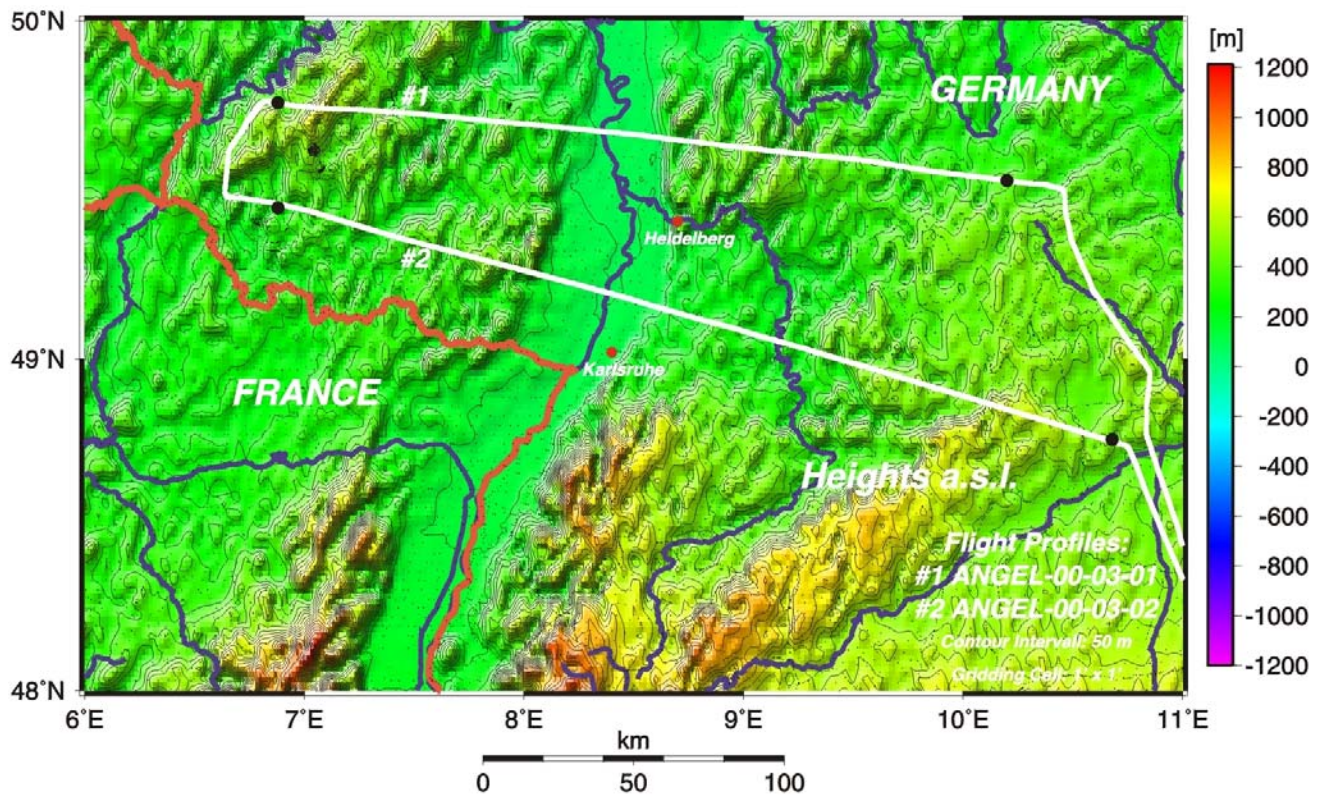


Figure 9.4.2: Height map of the Rhine Graben area derived from ETOPO'2 data

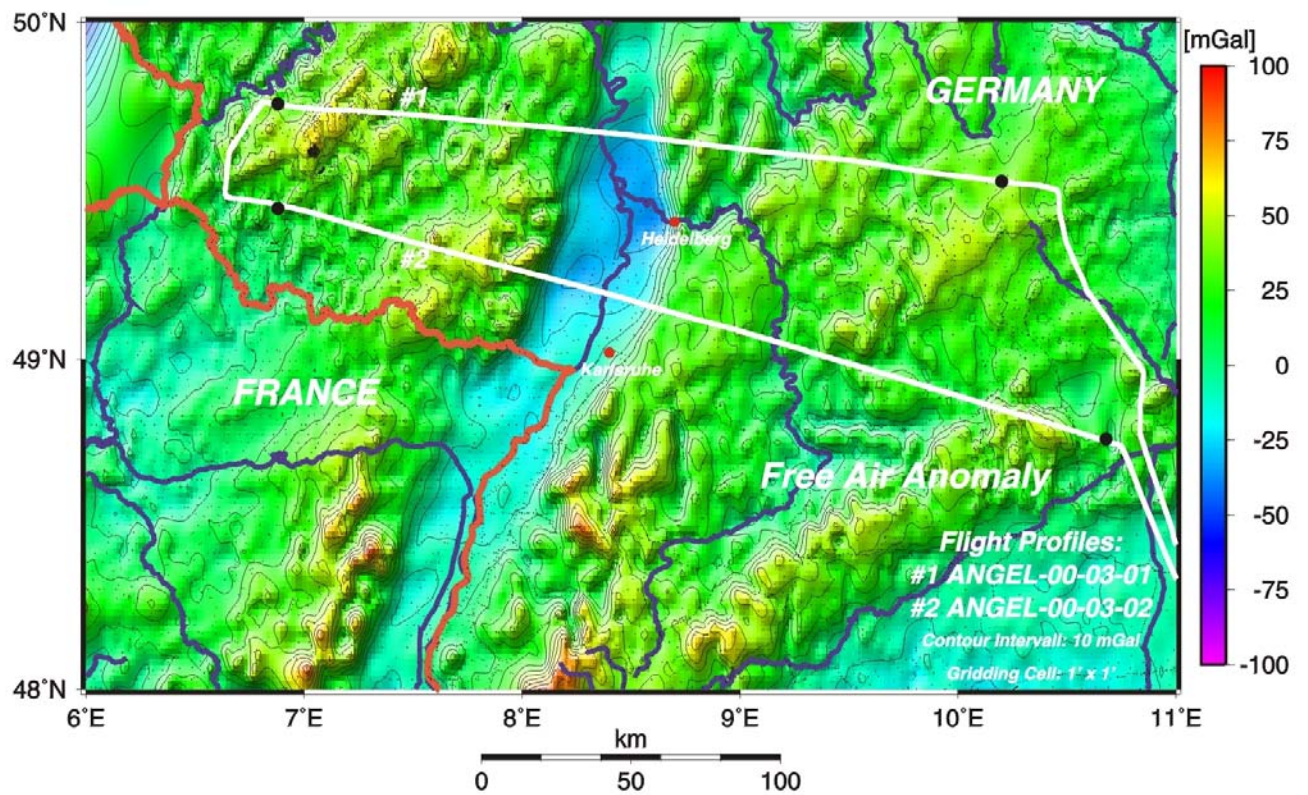


Figure 9.4.3 Free-air anomaly map of the Rhine Graben area from the BGI and GGA data sets

## 9.5 Airborne data: Rhine Graben

The Rhine Graben survey took place the day after the flights over the Bavarian Alps. On this day, the 24<sup>th</sup> of May 2000, SAPOS network stations were available in the survey area. Ground reference GPS data were received from Karlsruhe, Daun, Heidelberg, Ansbach, Alzey, Kitzingen, Nördlingen, Schwäbisch-Hall and Oberpfaffenhofen. For final processing, the GPS station in Heidelberg showed the most suitable data. The processing result is shown in Fig. 6.5.1, covering the leg number 2 over the Rhine Graben.

In contrast to the first profile over the Alps, the second profile over the Rhine Graben was performed under rather smooth flight conditions. The data were filtered using a 120 second, 3 stages Butterworth filter. The results shown in Fig. 9.5.1 have a mean deviation of 0.32 mGal from the ground truth data with rms of 5.64 mGal. This rms would be even smaller if artifacts in the ground truth data (as seen at second 300) were removed. Apart from small disturbances, the overall data quality is good.

Small sinusoidal-like perturbations result from imperfect cross coupling correction due to slightly wrong manufacturers corrections coefficients. These coefficients are now being estimated by cross correlation techniques.

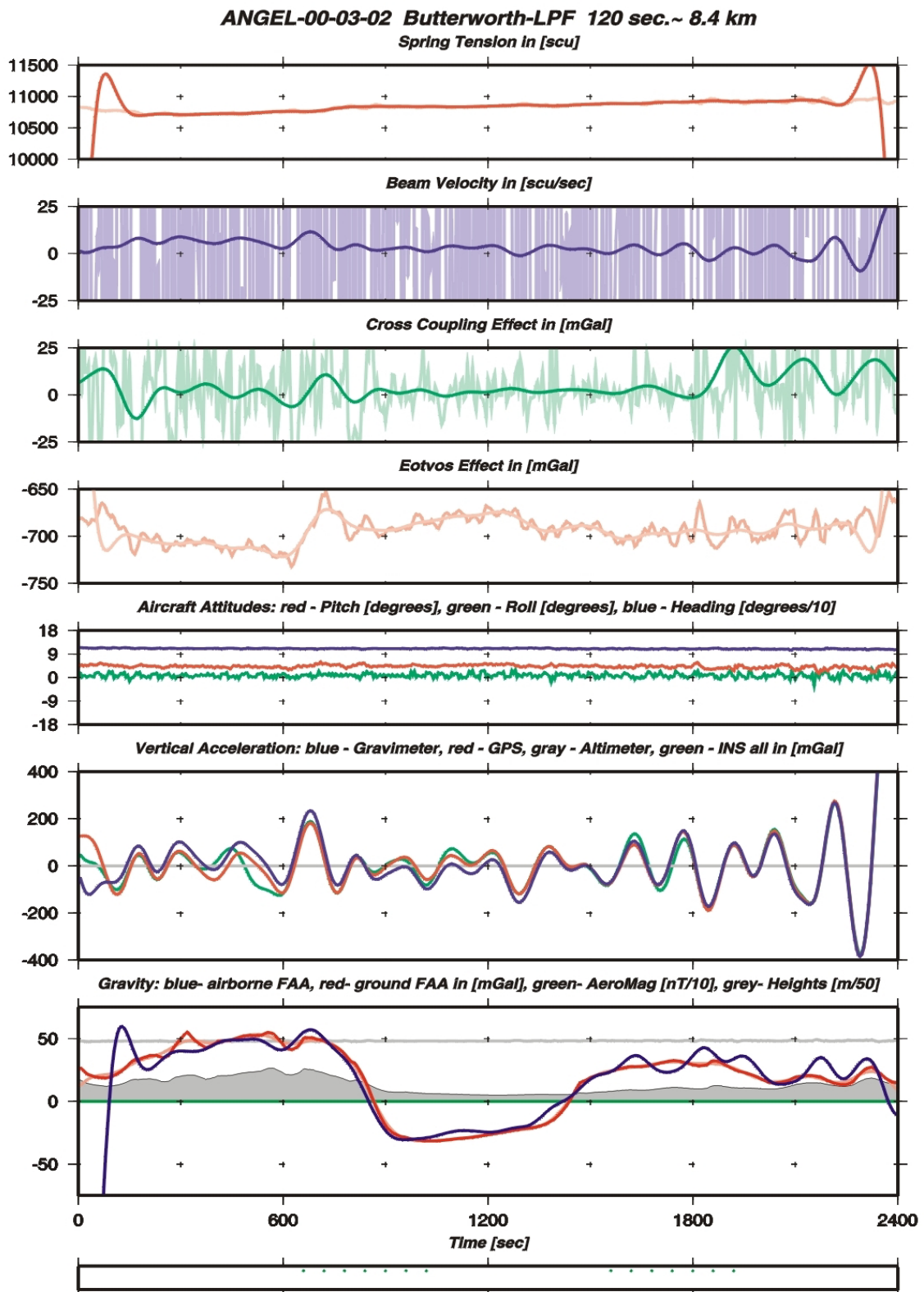


Figure 9.5.1: Rhine Graben airborne gravimetry profile

## **10 Conclusions**

### **10.1 Hardware**

Most of the hardware components showed no failures. Problems occurred with Toshiba laptops on a rather shakey laptop rack used in the Cessna Grand Caravan. For later surveys, a new, more stable laptop rack was constructed. The biggest problem occurred with the laser triggering. All external triggers were ignored when the actual measurement was not successful because the integration range was widened until the signal strength was sufficiently high.

### **10.2 Software**

The software needs some more homogenization for easy application. Within the AGS-124 program for aerogravimetry processing, a FIR-filter should be included. In the long run, all programs necessary for aerogravimetry data processing should be able to be used on Windows based PCs and on UNIX based workstations. In the long term, work on the software should also include some more detailed upward and downward continuation algorithms.

### **10.3 SAGS**

The SAGS processing is still being developed at the Bayerische Akademie der Wissenschaften.

# 11. Technical specifications of the instruments

## 11.1 LaCoste & Romberg S124b

### Overview

Platform physical size:	55 cm (22") W x 70 cm (27") D x 64 cm (25") H
Platform weight with sensor:	79 kg (175 lbs.)
Center of gravity height:	28 cm (15")
Driver / Computer unit size:	46.5 cm (19") W x 48 cm (18.9") D x 27 cm (10.6") H
Driver / Computer unit weight:	21 kg (46 lbs.)
Keyboard unit size:	46.5 cm (19") W x 44 cm (17.3") D x 4.5 cm (2") H
Keyboard unit weight:	7 kg (15.5 lbs.)
UPS physical size:	43.3 cm (17") W x 41 cm (16") D x 9 cm (4") H
UPS weight:	19 kg (42 lbs.)
Operating temperature:	0°C to 40°C (32°F to 104° F)
Storage temperature:	-30°C to 50°C (-22° F to 122° F)
Power requirements:	300 Watts @ 115/230 VAC or ~ 1.5 A@230VAC

- a. Control Panel
- b. Sensor Lid Instruments
- c. Sensor
- d. Torque Motors
- e. Gimbals
- f. Oil Filled Dampers
- g. UPS
- h. Ground Plate
- i. Airdamped Shockmounts
- j. Frame
- k. Lower Elastic Strings
- l. Pressure Display
- m. Upper Elastic Strings.

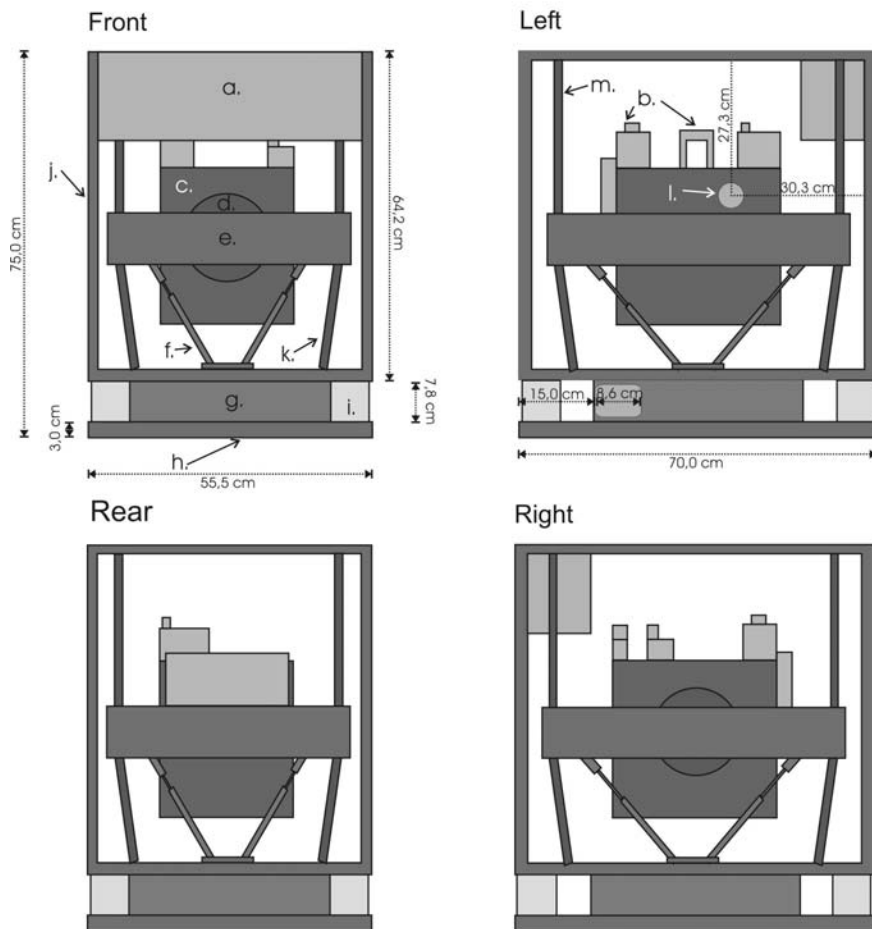


Figure 11.1.1: LaCoste & Romberg S124b gravity meter system within the dual gimbal frame

### *Short description*

The Model "S" gravity meter consists of a highly damped, zero-length spring type gravity sensor mounted on a stabilized platform with associated control electronics and recording system. The meter uses two-axis platform stabilization. The control electronics are digital solid state and designed to withstand the conditions encountered on surface ships and aircraft .

### *Sensor specifications*

Range:	12,000 mGal
Drift:	3.0 mGal per month or less
Temperature set point:	49° C
internal k-Factor:	1.37
external k-Factor:	37.9
Scale-factor (spring tension):	1.014
<i>Stabilized platform specifications</i>	
Platform pitch (mechanical):	± 25 degrees
Platform roll (mechanical):	± 25 degrees
Platform pitch (accelerometer range):	± 16 degrees
Platform roll (accelerometer range):	± 16 degrees
Platform period:	4 minutes (used for airborne applications)
Platform damping:	0.707 of critical period

### *Control systems specifications*

Recording rate:	1Hz plus 10Hz for beam positions (AIRSEA 3.1)
Serial output:	RS-232
Additional output:	3 analogue channels (±10V)

### *Gravity system specifications*

Accuracy in laboratory:	± 0.25 mGal @ 50000 mGal horizontal acceleration
	± 0.50 mGal @ 100000 mGal horizontal acceleration
	± 0.25 mGal @ 100000 mGal vertical acceleration

### *Environmental effects*

The sensor is temperature controlled, pressure sealed, and protected from magnetic fields. The sensor is permanently sealed and filled with dry nitrogen at the factory.

### *Inherent short-time response*

Although no use has yet been made of the short response time inherent in the gravity sensor, it should be noted that the response time is less than one thousandth of a second when the velocity of the mass is taken into account. The reason for not making use of the short response time is that gravity readings have to be filtered to remove unknown accelerations due to wave motion. Such filtering removes any information that might be obtainable from the fast response. With high resolution GPS, some operators are now making use of this fast response.

### *High response torque motors*

High response torque motors control the stabilized platform. These motors have no gear trains that would slow the response, introduce backlash and greatly increase friction.

### *Proportional heating system*

The new proportional heating system for the gravity meter heater circuit and both gyro heaters removes heater noise from traditional on-off heating circuits.

### *AIRSEA 3.1 digital control system*

A computer controls the stabilized platform and sensor, records data and performs system checks. The highly automated system permits fully unattended operation. When turned on, the system automatically sequences through a start-up procedure. If desired, menu selections allow the automatic system to be disabled and full manual control to be implemented.

### *Accuracy*

Accuracy determinations have been made by checking gravity readings taken at intersections of the network of traverses that are usually made in commercial surveys. When comparing the accuracy of different surveys, consideration must be given to the size of the ship or aircraft, the sea conditions, and the precision of the navigational system used. It is generally agreed that navigational errors contribute more to the overall errors than do gravity meter errors. Accuracy within 1 mGal is consistently reported.



**Figure 11.1.2:** LaCoste & Romberg gravity meter in a Britten-Norman Islander aircraft

## 11.2 IGI Inertial Navigation System

### Overview

IMU sensor unit physical size:	20 cm (7,9") W x 20 cm (7,9") D x 25 cm (9,8") H
IMU sensor unit weight:	49.5 kg (109 lbs.) (without cable)
IMU E-box unit physical size:	20 cm (7,9") W x 35 cm (13,8") D x 25 cm (9,8") H
IMU E-box unit weight:	49.5 kg (109 lbs.) (without cables)
IMU E-box power requirements:	60 Watts @ 12 VDC (initial heating) 15 Watts @ 12 VDC (standard operation)
CAE-10-01 unit physical size:	48,3 cm (19,0") W x 36 cm (14,2") D x 18 cm (7,1") H
CAE-10-01 unit weight:	4.5 kg (9.9 lbs.) (without cables)
CAE-10-01 power requirements:	less than 10 Watts @ 12 VDC or 220 VAC



**Figure 11.2.1:** CAE-10-01 control and data acquisition unit



**Figure 11.2.2:** IGI E-Box for power and signal conversion



**Figure 11.2.3:** IGI sensor head

### 11.3 Ashtech Z-Surveyor GPS receiver



**Figure 11.3.1:** Ashtech Z-Surveyor

#### *Overview*

Physical size:	7.6 cm (3") W x 21.0 cm (8.3") D x 18.5 (7.3") cm H
Receiver weight:	1.7 kg (3.75 lbs)
Power requirements:	7.5 Watts @ 10 - 28 VDC
Battery:	-20°C to +50°C, 12 V, 4.5 hours of operation
Temperature ranges	
Receiver:	-30°C to +55°C (Operation) -40°C to +85°C (Storage)
Antenna:	-40°C to +65°C (Operation) -55°C to +75°C (Storage)
Water resistance:	meets MIL-STD 810E, wind driven rain and dust

#### *Performance*

Static, rapid static survey:	5 mm + 1 ppm 2d-rms
Post-processed kinematic survey:	1 cm + 1 ppm 2d-rms
Real-time differential position:	< 1 m 2d-rms
Static occupation time:	2 seconds
Azimuth:	0.15 + 1.5 / baseline in km (arcsec)
RTK on-the-fly initialization:	> 99.9% reliability
RTK initialization time:	< 30 seconds following the acquisition of 8 or more satellites
RTK baseline recommendation:	< 10 km
RTK maximum baseline:	< 40 km

(All accuracies assume a minimum of 5 satellites at good quality.)

#### *PC-Card Specifications*

Type:	ATA Type II PCMCIA Memory Card
Temperature Range:	-40°C to +85°C
Typical number of epochs:	4500 per 2 MB @ 8 satellites, 20 seconds data rate

#### *Features*

- 12 channel all-in-view operation
- Full wavelength carrier on L1 and L2
- Z-Tracking and multi-path mitigation
- Real-time kinematic for cm-accuracy
- Dual-frequency smoothing for improved code differential
- Removable PCMCIA memory card slot
- Selectable update rate from 1 to 5 Hz (10 Hz optional)
- Real-time data output on NMEA 0183 output
- 1 PPS timing signal output
- Remote monitoring
- 4 RS-232 ports (115200 baud max.)

#### 4.3.2 Technical specifications

### Overview

Physical size:	13 cm (5") W x 20 cm (8") D x 7.6 cm (3") H
Weight:	approx. 1.5 kg (3.3 lbs)
Power requirement:	approx. 10 Watt @ 11-18 Volts DC protecting circuitry for over-voltage and reverse polarity
Option 20-28 VDC:	external pre-stabilization and protecting module STAB95 (used on aircraft installation)
Option 220 VAC	external power supply module VNG95 (not yet available at GFZ)
Temperature range:	Operation -10° C to +50° C Storage -20° C to +60° C
Protection class:	IP64
Aiming device (opt.):	Telescope or red semiconductor-laser beam pointer to be mounted on top of the instrument (not at GFZ)

### Features

- Accurate & dynamic measurement of distance and speed
- Excellent performance and reliability; light weight and stable metal housing
- Short high-energy infrared light pulses provide excellent interference immunity
- Measurements are fast offering update rates as high as 200 Hz / 2 kHz / 12 kHz
- Measurements can be taken through glass windows into sealed containers
- Narrow measurement beam with very low divergence: excellent spatial resolution
- Measurements can be taken to almost any surface regardless of the incident beam angle or surface characteristics
- Measurements are unaffected by the temperature of the material surface and of temperature gradients in the medium between the sensor and the target surface

### Data output

Data interfaces:	RS232 & RS422 (selectable, standard for all types) Baud rate selectable between 150 Baud and 19200 Baud, further 38.4 kBaud and 115.2 kBaud RS422 high speed (available for VHS types only) 115.2 kBaud in "high speed" mode, 19.2 kBaud in "adjust" mode, asynchronous Parallel interface (extended capabilities port)
Available data output: (options not for all types)	Analogue current, 4-20 mA <sup>1</sup> , not galvanically isolated, resolution 16 Bit, linearity 0.05 ‰ of full scale
Switching output	2 x PNP transistor driver <sup>2</sup> built-in thermal and short-circuit protection switching current 250 mA maximum switching voltage = supply voltage

<sup>1</sup> operating range selectable via serial interface

<sup>2</sup> switching points adjustable via serial interface

### *Performance*

Measuring range (depending on the reflection coefficient of the target):	
good, diffusely reflecting targets, reflectivity <sup>3</sup> :	80 up to 500 m <sup>1</sup>
bad, diffusely reflecting targets, reflectivity <sup>3</sup> 10%:	up to 150 m <sup>1)</sup>
reflecting foil <sup>2</sup> or plastic cat's-eye reflectors:	> 1000 m
Minimum distance:	typically 5 - 10 m
Distance measurement accuracy <sup>3</sup> :	typically ±5 cm worst case ±10 cm
Measuring time (ms or s) <sup>4</sup> :	10ms / 20ms / 50ms / 0.1 / 0.2 / 0.5 / 1 / 2
Statistical deviation (cm) <sup>5</sup> :	±10 / ±7 / ±5 / ±3 / ±2 / ±1.5 / ±1 / ±0.7
Resolution <sup>5,6</sup> :	10 / 10 / 5 / 5 / 2 / 2 / 1 / 1
<i>Speed measurement:</i>	
Measuring range:	0 to ±30 m/s
Accuracy:	±0.5 m/s
Measuring time, typically <sup>4</sup> :	0.5 s
Divergence of the infrared measuring beam <sup>7</sup> :	1.8 mrad
Eye safety class:	according to CENELEC EN 60825-1 (1997)

<sup>1</sup> Typical values for average conditions. In bright sunlight, the operational range is considerably shorter than under an overcast sky. At dawn or at night the range is even higher.

<sup>2</sup> Reflecting foil 3M 2000X or equivalent, minimum dimensions 0.45 x 0.45 m<sup>2</sup>.

<sup>3</sup> Standard deviation, plus distance depending error < 20 ppm.

<sup>4</sup> Adjustable via RS232.

<sup>5</sup> Depending on measuring time.

<sup>6</sup> Chosen automatically by the internal microprocessor.

<sup>7</sup> 1 mrad corresponds to 10 cm beam width per 100 m of distance.

### *Survey performance, latest changes and future plans*

The laser performed well over all water surfaces at even more the 800 meters altitude when no fog or clouds were in the way. Problems were detected with the laptop that controlled the laser. It could not handle the vibrations in the aircraft and had to be often rebooted. Another problem occurred with triggering. The laser readings have no internal time stamps. Even when external triggers are applied, these triggers are ignored when a measurement fails due to low signal quality. This apparent bug for our application was fixed by Riegl©. After changing the measurement program please note that is mandatory to choose to trigger period that is bigger (not equal!) to double the measurement cycle time.

## 11.4 Trimble 4000 SSE GPS receiver



Figure 11.4.1: Trimble receiver

### Overview

Physical size:	24.8 cm (9.8") W x 28 cm (11") D x 10.2 cm (4") H
Receiver weight:	3.1 kg (6.8 lbs) 5.5 kg (12 lbs) with battery pack and cables
Power requirements:	9 Watts @ 10.5 to 35 VDC, triple power inputs
Battery:	8 hrs continuously with 4 camcorder batteries
Env. operating temperature:	-20°C to +55°C (-40°F to +131°F)
Storage temperature:	-30°C to +75°C (-40°F to +167°F)
Humidity:	100%, fully sealed, buoyant

### Performance

Static survey modes:	Quick-start, Planned survey, Auto-timed survey
Accuracy:	Horizontal: $\pm 5 \text{ mm} + 1 \text{ ppm} * \text{baseline in km}$ Vertical: $\pm 10 \text{ mm} + 1 \text{ ppm} * \text{baseline in km}$ Azimuth: $\pm 1 \text{ arc second} + 5 / \text{baseline in km}$

### Kinematic survey performance (post-processed) modes

Continuous, stop & go accuracy:	Horizontal: $\pm 2 \text{ cm} + 1 \text{ ppm} * \text{baseline in km}$ Vertical: $\pm 2 \text{ cm} + 1 \text{ ppm} * \text{baseline in km}$
Occupation:	Continuous: 1 sec measurement Stop & go: 2 epochs (min.) with 5 satellites
Fastest continuous data rate:	1Hz
Start-up:	< 2 minutes from power-on to start survey with recent ephemeris
Tracking:	L1 C/A code, L1/L2 full-cycle carrier. Fully operational during P-code encryption.
Number of channels:	Total station: 9
Data-logging:	In internal memory

### Features

- Tracking: 9 channels of L1/L2 P-Code and full cycle carrier phase
- 1 PPS output
- NMEA-0183 output
- 5 to 10 MB Internal memory
- Fully functional, integrated control panel

## 11.5 Novatel OEM4 GPS receiver

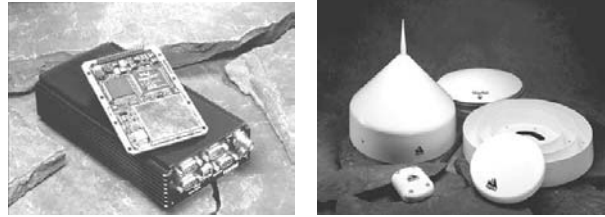


Figure 11.5.1: Novatel OEM-4 receiver, antennae

### Overview

Physical size:	11.1 cm (4.4") W x 20.8 cm (8.2") D x 5.4 cm (2.1") H
Receiver weight:	0.98 kg (2.2 lbs)
Power requirements:	3.3 Watts (typical), 4 Watts (maximum) @ 10 to 36 VDC
Battery:	no internal battery
Env. operating temperature:	-40°C to +75°C (-40°F to +167°F)
Storage temperature:	-45°C to +95°C (-49°F to +203°F)
Humidity:	95%, non-condensing
Interfaces:	RS-232 ports, 2 ports 230 to 300 bps, one port 400 bps
Strobes:	PPS, mark in, mark out, position valid, frequency out
Communication connectors:	2 times DB-9P
Antenna connectors:	female TNC
External oscillator:	male SMB

### Performance

Single point L1:	1.8 m CEP
Single point L1/L2:	1.5 m CEP
DGPS (L1, C/A):	0.45 m CEP
L1, C/A code precision:	6 cm RMS
L2, P-code precision:	25 cm RMS (AS on)
L1 carrier phase precision:	0.75 mm RMS (differential channel)
L2 carrier phase precision:	2 mm RMS (differential channel)
Measurements rates:	20 Hz
Position rates:	20 Hz
L1 signal re-acquisition:	0.5 s (typical)
L2 signal re-acquisition:	6 s (typical)
Time accuracy:	102 ns RMS
Velocity accuracy:	0.03 m/s RMS
Acceleration dynamics:	10 g
Vibration dynamics:	4 g (sustained tracking)
Velocity dynamics:	515 m/s maximum

### Features

The Novatel OEM-4 receivers offer 24-channel performance on the L1/L2 frequencies using the pulse aperture correlator (PAC) technology. It offers a maximum of 20-Hz raw data and position data output. It has no displays or control panels and thus needs a laptop or palmtop for control purposes, switch setting and data storage. Certificated aircraft antennas and choking antennas are available to employ the receivers in airborne and land-based operation.

## 11.6 Riegl laser altimeter

### Overview

Physical size:	13 cm (5") W x 20 cm (8") D x 7.6 cm (3") H
Weight:	approx. 1.5 kg (3.3 lbs)
Power requirement:	approx. 10 Watt @ 11-18 Volts DC protecting circuitry for over-voltage and reverse polarity
Option 20-28 VDC:	external pre-stabilization and protecting module STAB95 (used on aircraft installation)
Option 220 VAC	external power supply module VNG95 (not yet available at GFZ)
Temperature range:	Operation -10° C to +50° C Storage -20° C to +60° C
Protection class:	IP64
Aiming device (opt.):	Telescope or red semiconductor-laser beam pointer to be mounted on top of the instrument (not at GFZ)

### Features

- Accurate & dynamic measurement of distance and speed
- Excellent performance and reliability; light weight and stable metal housing
- Short high-energy infrared light pulses provide excellent interference immunity
- Measurements are fast offering update rates as high as 200 Hz / 2 kHz / 12 kHz
- Measurements can be taken through glass windows into sealed containers
- Narrow measurement beam with very low divergence: excellent spatial resolution
- Measurements can be taken to almost any surface regardless of the incident beam angle or surface characteristics
- Measurements are unaffected by the temperature of the material surface and of temperature gradients in the medium between the sensor and the target surface

### Data output

Data interfaces:	RS232 & RS422 (selectable, standard for all types) Baud rate selectable between 150 Baud and 19200 Baud, further 38.4 kBaud and 115.2 kBaud RS422 high speed (available for VHS types only) 115.2 kBaud in "high speed" mode, 19.2 kBaud in "adjust" mode, asynchronous Parallel interface (extended capabilities port)
Available data output: (options not for all types)	Analogue current, 4-20 mA <sup>1</sup> , not galvanically isolated, resolution 16 Bit, linearity 0.05 ‰ of full scale
Switching output	2 x PNP transistor driver <sup>2</sup> built-in thermal and short-circuit protection switching current 250 mA maximum switching voltage = supply voltage

<sup>1</sup> operating range selectable via serial interface

<sup>2</sup> switching points adjustable via serial interface

*Drawings*

1. 9pole socket for RS232/RS422 data interface
2. LED "POWER ON"
3. 10pole socket for power supply and optional current or voltage output
4. Fuse holder
5. Rubber-armored front and rear panel
6. Mounting plates with 2xM6 threads on both sides of the instrument
7. (a) Mounting for aiming device (optional)  
(b) Telescope (optional)
8. Receiver lens
9. Transmitter

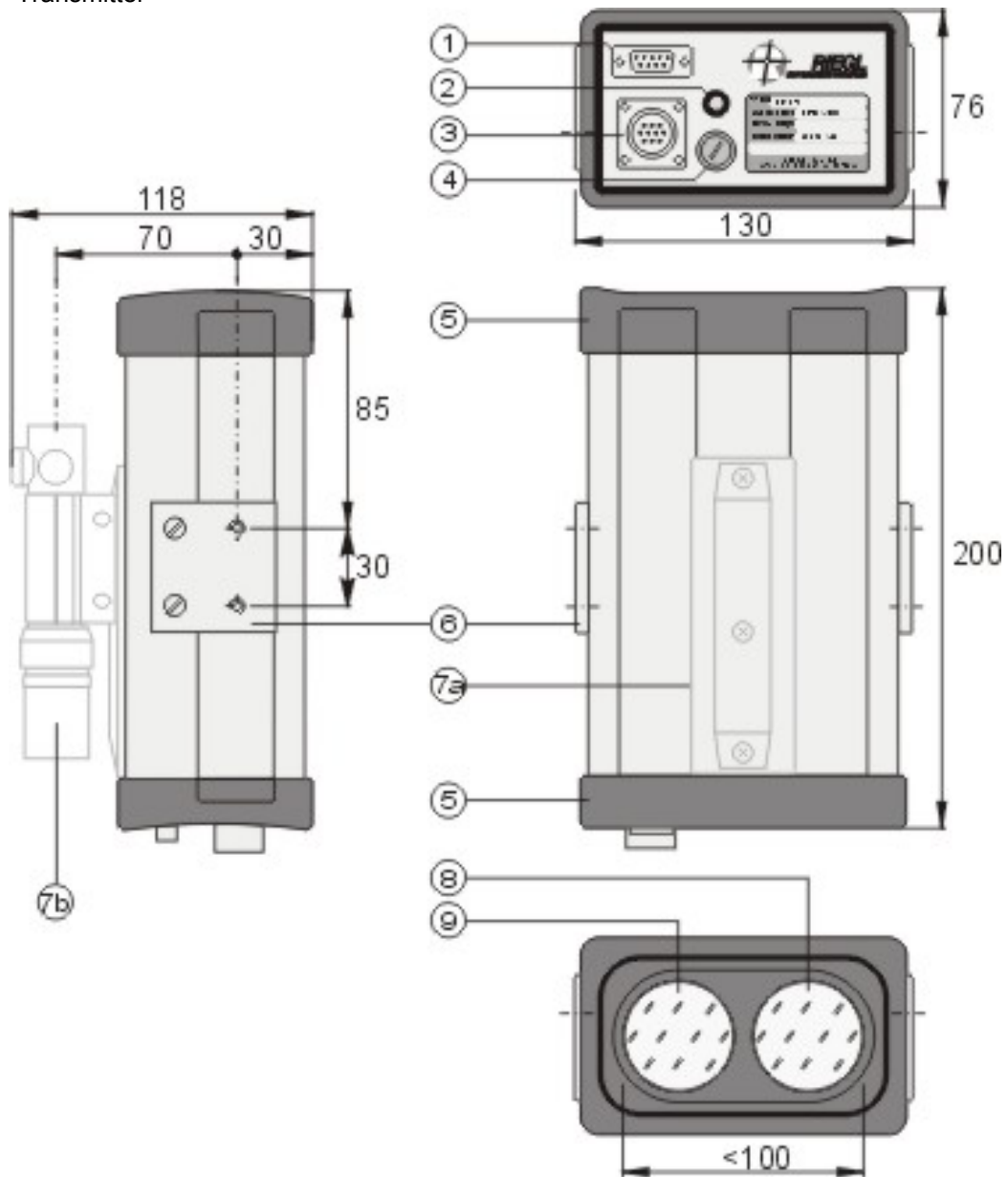


**Figure 11.6.1:** Drawings of LD90-3300HR housing

### *Performance*

Measuring range (depending on the reflection coefficient of the target):	
good, diffusely reflecting targets, reflectivity <sup>3</sup> :	80 up to 500 m <sup>1</sup>
bad, diffusely reflecting targets, reflectivity <sup>3</sup> 10%:	up to 150 m <sup>1)</sup>
reflecting foil <sup>2</sup> or plastic cat's-eye reflectors:	> 1000 m
Minimum distance:	typically 5 - 10 m
Distance measurement accuracy <sup>3</sup> :	typically ±5 cm worst case ±10 cm
Measuring time (ms or s) <sup>4</sup> :	10ms / 20ms / 50ms / 0.1 / 0.2 / 0.5 / 1 / 2
Statistical deviation (cm) <sup>5</sup> :	±10 / ±7 / ±5 / ±3 / ±2 / ±1.5 / ±1 / ±0.7
Resolution <sup>5,6</sup> :	10 / 10 / 5 / 5 / 2 / 2 / 1 / 1
<i>Speed measurement:</i>	
Measuring range:	0 to ±30 m/s
Accuracy:	±0.5 m/s
Measuring time, typically <sup>4</sup> :	0.5 s
Divergence of the infrared measuring beam <sup>7</sup> :	1.8 mrad
Eye safety class:	according to CENELEC EN 60825-1 (1997)

<sup>1</sup> Typical values for average conditions. In bright sunlight, the operational range is considerably shorter than under an overcast sky. At dawn or at night the range is even higher.

<sup>2</sup> Reflecting foil 3M 2000X or equivalent, minimum dimensions 0.45 x 0.45 m<sup>2</sup>.

<sup>3</sup> Standard deviation, plus distance depending error < 20 ppm.

<sup>4</sup> Adjustable via RS232.

<sup>5</sup> Depending on measuring time.

<sup>6</sup> Chosen automatically by the internal microprocessor.

<sup>7</sup> 1 mrad corresponds to 10 cm beam width per 100 m of distance.

## 11.7 Meinberg clock and central trigger

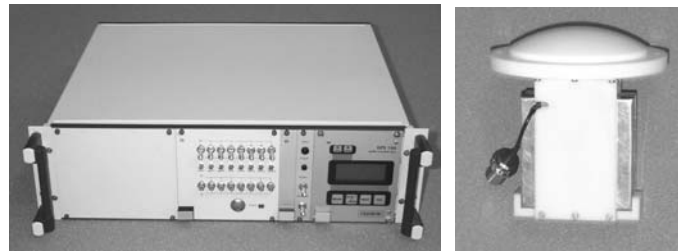


Figure 11.7.1: Trigger system and antenna

### Overview

Physical size:	48,3 cm (19") W x 40 cm (15,7") D x 20 cm (7,8") H
Receiver weight:	8 kg (18 lbs)
Power requirements:	~5 Watts @ 10 to 36 VDC
Battery:	internal battery, bridges ~ 15 minutes power break
Env. Operating temperature:	-10°C to +40°C (14° F to +104° F)
Storage temperature:	-10°C to +40°C (14° F to +104° F)
Interface:	2 times RS-232
Strobes:	PPM, 2 times PPS, 4 Hz, 10 Hz, 20 Hz, 50 Hz, 100 Hz
Continuous signal:	sinus signal, repetition rate 1 Hz
Trigger connectors:	12 times female BNC
Antenna connectors:	female N

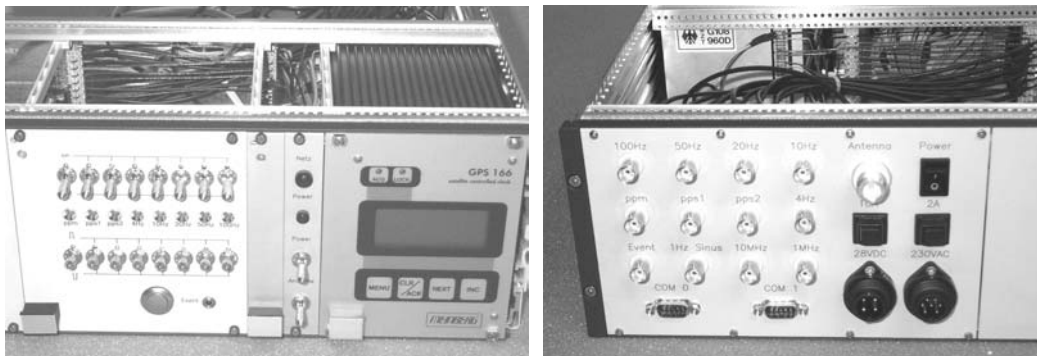


Figure 11.7.2: Front and rear details

### Features

The main instrument is a Meinberg GPS166 clock. It is connected to a GFZ modified antenna system. The Meinberg clock triggers itself on the GPS time signal and then operates on an interior clock system in a stand-alone mode. The main internal clock frequency is used to generate a sinus signal with a period of one second. The phase information of the sinus is accurate enough to determine microsecond timing. Moreover, pulse signals at different frequencies are generated. Their trigger pulse can be switched between positive and negative flanks depending on the instrument to trigger. Beyond the signals and pulses generated by the trigger system, an ASCII time information string is also available. All trigger pulses are enabled at the next full GPS minute for better data handling. The Meinberg antenna and timing system is designed for static, pre-flight use only. For the flight, the antenna is switched off and the time is generated by a highly precise quartz that was synchronized to the GPS timing.

## 11.8 SAGS 2.2

### Overview

Sensor unit physical size:	42 cm (16.5") W x 42 cm (16.5") D x 34 cm (13.4") H
Sensor unit weight:	49.5 kg (109 lbs.) (incl. SINS & VIP)
Sensor power requirements:	60 Watts @ 12 VDC (initial heating) 15 Watts @ 12 VDC (standard operation)
Meinberg clock physical size:	24 cm (9.5") W x 36 cm (14.2") D x 14 cm (5.5") H
Meinberg clock weight:	4.5 kg (9.9 lbs.)
Clock power requirements:	less than 10 Watts @ 12 VDC or 220 VAC
Data logger – notebook:	Type Kontron / Panasonic CF25 or
Data logger physical size:	30 cm (12") W x 30 cm (12") D x 30 cm (12") H
Data logger weight:	4 kg (8.8 lbs.)
Data logger power requirements:	max. 40 Watts @ 220 VAC

### Features

- Orthogonal accelerometer triad of Q-Flex QA3000/30,
- Total range per axis: 25 g, configured recording range  $1g \pm 0.3g$ ,
- Resolution:  $\sim 1\text{mGal}$ , Noise:  $\sim 5\text{mGal}$  for single observation,
- Temperature setting  $\geq$  ambient temperature  $+10^\circ$ ,
- Adjustable analogue low pass filter Bessel type,  $f_c$  (typical) = 10 Hz,
- Time Synchronization: Meinberg Clock or similar (see separate sheet) with GPS time synchronization and time telegram.

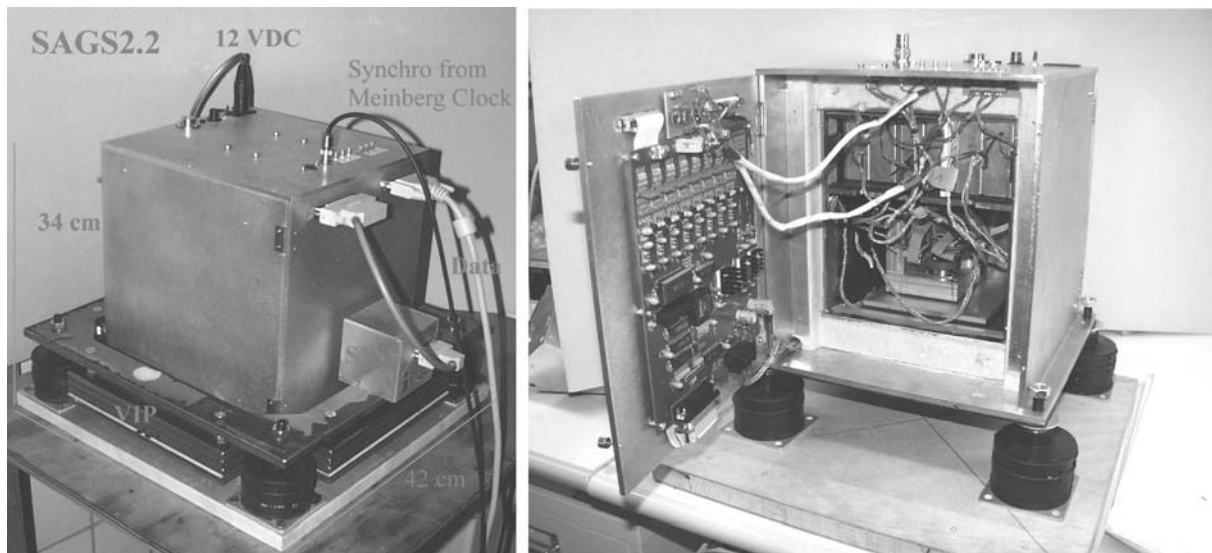


**Figure 11.8.1:** SAGS-2 sensor unit (closed, mounted on vibration damping platform, on the left) and SAGS-2.2 sensor unit (opened, on the right)

*Timing and signal synchronization*

One of the most essential requirements for successful SAGS measurements is exact timing and synchronization. Therefore, a Meinberg GPS clock is used that generates a sinus signal that is detected and sampled within the SAGS data acquisition unit. The sinus signal is repeated every second with its phase exact enough to get time information down to 1/1000 of a second.

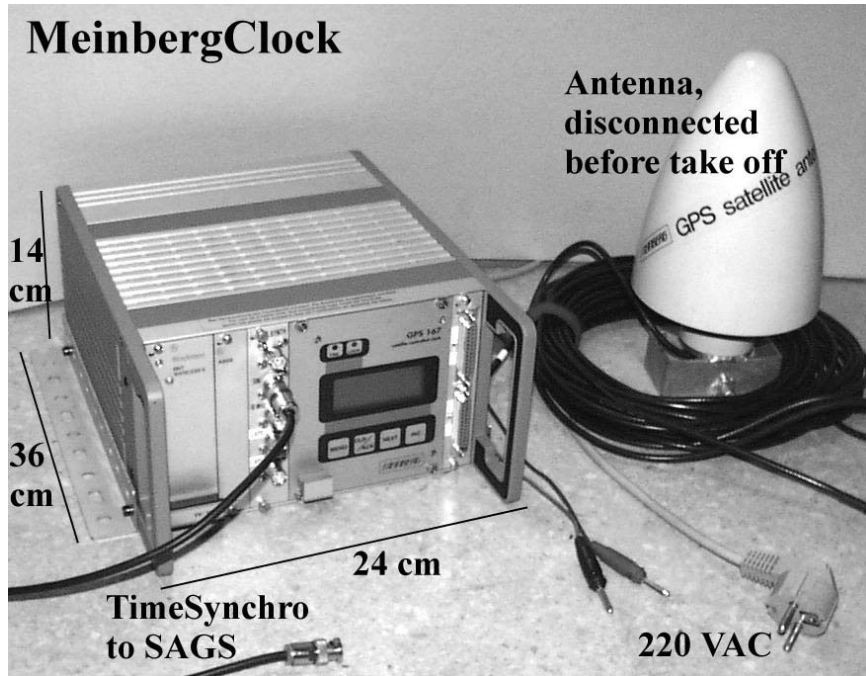


**Figure 11.8.2:** Meinberg clock and antenna

## 11.9 DLR Cessna Grand Caravan

### Size and Performance

Design weight	Span (overall) ..... 52 ft. 1 in.
Maximum ramp weight ..... 8785 lbs.	Area ..... 279.40 sq. ft.
Maximum take-off weight.....8750 lbs.	Sweepback (at 50% chord).... 0 degrees
Maximum landing weight..... 8500 lbs.	Dihedral ..... +3 degrees
Standard empty weight ..... 4237 lbs.	Taper ratio ..... 0.586
Maximum useful load..... 4548 lbs.	Aspect ratio..... 9.555
Maximum weight..... 8550 lbs.	Mean aerodynamic chord ..... 66.474 in.
(Cargo pod installed – flight into icing)	Horizontal tail
Capacities	Span (overall) ..... 20 ft. 6 in.
Maximum fuel .... 335.6 gallon / 2249 lbs.	Area ..... 70.04 sq. ft.
Usable fuel..... 332 gallon / 2224 lbs.	Sweepback..... 0° at elevator hinge line
Oil..... 14 qt.	Aspect ratio..... 6.0
Power plant	Mean aerodynamic chord ..... 41.984 in.
Pratt & Whitney PT6A-114A	Vertical Tail
675 shp @ 1900 rpm	Height (overall) ..... 8 ft. 2 in.
Propeller	Area (including dorsal fin) 39.92 sq. ft.
McCaughey constant speed	Sweepback+9.437° at rudder hinge line
full feathering, reversible	Cabin
3 blades 106 inches diameter	Height (floorboard to headliner)4 ft. 3 in.
Loading	Length – firewall to
Wing ..... 31.3 lbs. / sq.ft.	aft bulkhead (nominal) ..... 21 ft. 4 in.
Power ..... 13.0 lbs. / shp	Width (max.) ..... 5 ft. 2 in.
Approximate dimensions	Landing Gear
Overall height ..... 14 ft. 10 in.	Tread..... 11.66 ft.
Overall length ..... 41 ft. 7 in.	Wheelbase ..... 13.29 ft.
Wing	Tire size – main 8.50 x 10, 8 ply, 55 psi
Speed	Tire size – nose 22 x 8.00-8, 6 ply, 36 psi
Cruise at 10,000 ft ..... 184 kts.	Service ceiling..... 23,700 ft.
Cruise at 20,000 ft. .... 174 kts.	Maximum certified altitude..... 25,000 ft.
Range	Maximum altitude in icing..... 20,000 ft.
(with 2224 pounds usable fuel and fuel allowance for engine start, taxi, takeoff, climb, descent and 45 minutes reserve)	Take-off performance
Max. cruise power at 10,000 ft .... 970 nm	(sea level, 8750 lbs.)
Endurance ..... 5.1 hr.	Ground roll ..... 1365 ft.
Max. cruise power at 18,000 ft... 1109 nm	Total distance Over 50 ft. obstacle 2420 ft.
Endurance ..... 6.6 hr.	Landing performance
Max. range power at 10,000 ft.... 1026 nm	(sea level, 8500 lbs., no reverse)
Endurance ..... 6.6 hr.	Ground roll ..... 950 ft.
Max. range power at 18,000 ft.... 1163 nm	Total distance over 50 ft. obstacle 1795 ft.
Endurance ..... 7.5 hr.	Stall speed
Rate of climb at sea level ..... 975 fpm	Flaps up, idle power ..... 78 kts.
	Flaps down, idle power ..... 61 kts

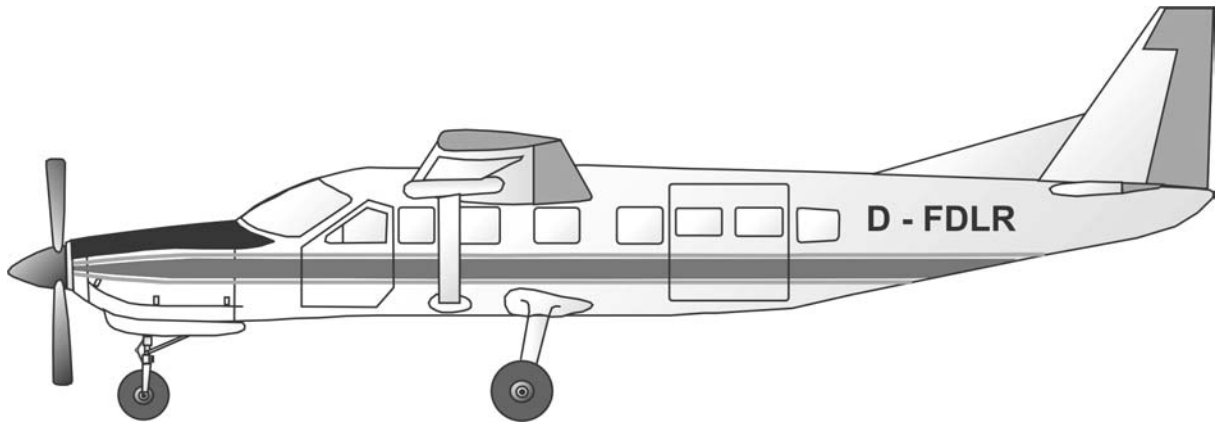


Figure 11.9.1: Cessna Grand Caravan D-FDLR side view (here equipped with wing tips)

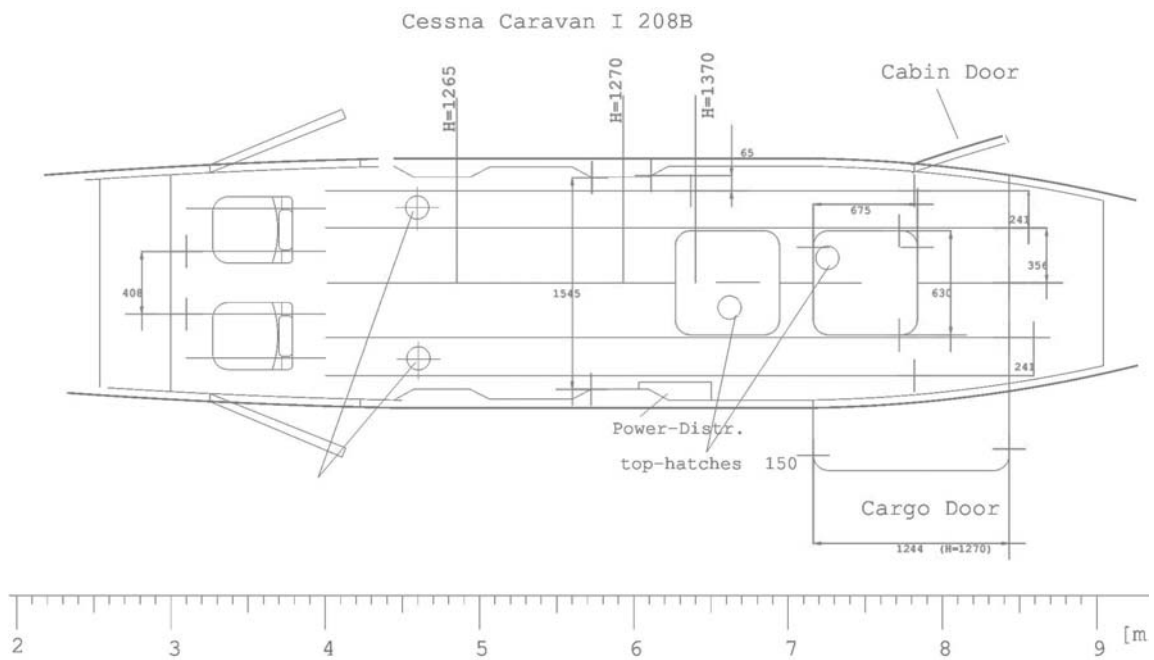


Figure 11.9.2: Cessna Grand Caravan cabin layout

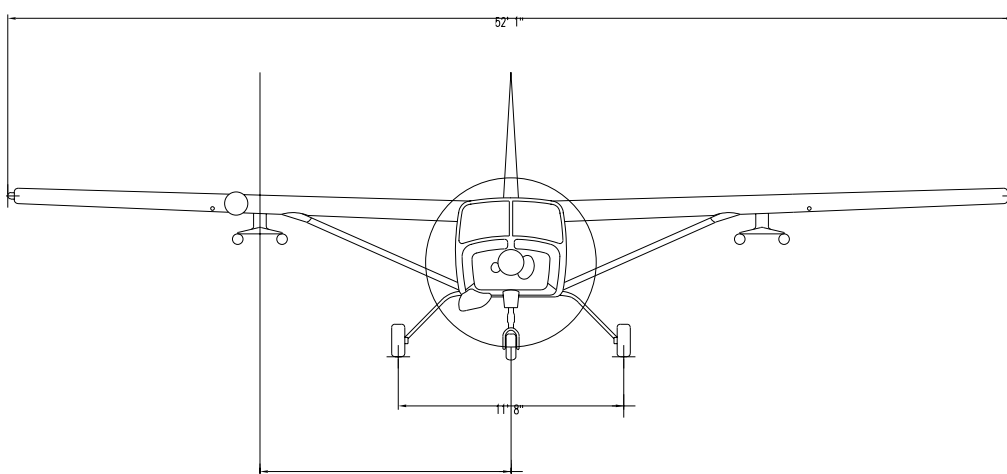


Figure 11.9.3: Cessna Grand Caravan front view (here equipped with wing tips)

### *Computer Controlled Navigation System (CCNS4) and AEROcontrol for aerial surveys*

The system is based on sensor information from GPS/DGPS and aircraft gyro or INS/IMU systems:

- The Standard CCNS4 gives graphic guidance information to the pilot and controls remote sensing sensor systems. Together with the AEROcontrol system, based on DGPS and information from inertial measurement unit (IMU) - it allows real-time or post processing of sensor positions – not GPS antenna positions - for given instants, e.g. aerial camera projection coordinates for the instant of exposure or SAR-antenna phase center position at given instants. The system allows the determination of the elements of exterior orientation ( $\phi/\omega/\kappa$  and  $x/y/h$ ). Heading information with an accuracy of  $1/10^\circ$  and pitch as well as roll information, are being furnished with an accuracy of  $1/100^\circ$ . The AEROcontrol is completely controlled by the standard CCNS4 as may be the remote sensing sensor(s).
- Principal items of the AEROcontrol system:
  - 12 channel parallel L1/L2 RX GPS receiver (modified ASHTECH Z-Surveyor), 1 Hz
  - Dry tuned Gyro with separate sensor head (modified LITEF LCR 88), 50 Hz
- 5-inch Control & Display Unit for both pilot and sensor operator
- Single crew operation for sensor missions is possible.
- The CCNS World Wide Mission Planning software (WWMP) enables the user to make flight plans based on topographic maps of the target country. A digitizer can be used to enter the area that is to be covered. Flight line spacing and waypoint / photo centers are calculated automatically for optimum coverage with minimum models. The flight data to be flown are then transformed into WGS84 coordinates and hand over to the CCNS4 system. The planning software is able to handle all kinds of maps, scales and grid/plain or geographic co-ordinate systems.
- DGPS-data are available via the Fugro OmniSTAR SYSTEM. OmniSTAR uses a network of reference stations to measure the errors included into the GPS signal by the US Department of Defense. The collected data is distributed by one of the three-network control centers worldwide. From there the data are up-linked to one of seven geostationary satellites world wide, which distributes the data over its footprint. The OmniSTAR signal can then be received with an OmniSTAR receiver and is available by subscription. Inside the user receiver-equipment a set of corrections is calculated on the basis of all reference data from all reference stations in a footprint. The correction is optimized for the users location. This technique called virtual base station (VBS) technology guarantees a high and consistent accuracy (sub meter). The corrections are not dependent on any one reference station.



**Figure 11.9.4:** Cessna Grand Caravan D-FDLR in flight operation

## 12 References

- Forsberg, R., Hehl, K., Bastos, L., Gidskehaug, A., Meyer, U., 1996: Development of a geoid mapping system for coastal oceanography (AGMASCO). In: Gravity, Geoid and Marine Geodesy, IAG Symp. Series 117, 163-170, Springer Verlag
- Boebel, T., 2000: Flugzeuggestützte Topographie- und Schweremessung: Messsystem und Anwendung auf die Region Framstraße, Spitzbergen und Nordostgrönland, Berichte zur Polarforschung, 366, Alfred-Wegener-Institut für Polar- und Meeresforschung, Bremerhaven
- Boedecker, G., Leismüller, F., Spohnholtz, T., Cuno, J. and Neumayer, H.K., 1994: Tests Towards Strapdown Airborne Gravimetry, Proceedings, Int. Symp. Kinematic Systems in Geodesy, Geomatics and Navigation. Banff 1994
- Bronstein, I. N. and Semendjajew, K. A., 1981: Taschenbuch der Mathematik, Teubner Verlag Leipzig
- Bruton, A. M., Glennie, C. L., Schwarz, K.-P., 1999: Differentiation for High-Precision GPS Velocity and Acceleration Determination, GPS Solutions, Vol. 2, No. 4, 7 – 21
- Bruton, A. M., Schwarz, K.-P., Ferguson, S., Kern, M., Wie, M., 2002: Deriving Acceleration from DGPS: Toward Higher Resolution Applications of Airborne Gravimetry, GPS Solutions, Vol. 5, No. 3, 1 - 14
- Cramer, M., 2001: Genauigkeitsuntersuchungen zur GPS/INS-Integration in der Aerophotogrammetrie, DGK-Reihe C- H. 537, Bavarian Academy of Sciences and Humanities
- Green, P.E., 1976: Mathematical Tools for Applied Multivariate Analysis, Academic Press
- Gurthner, W., 2000: RINEX: The receiver independent Exchange Format Version2, Astronomical Institute, University of Bern
- Hackney, R. I., Featherstone, W. E., 2003: Geodetic versus Geophysical Perspectives of the ‘Gravity Anomaly’, Geophysical Journal International, in press, 2003
- Harlan, R. B., 1968: Eötvös Corrections for Airborne Gravimetry, JGR, Vol. 73, No. 14, 4675 - 4679
- Jekeli, CH., 2001: Inertial Navigation Systems with Geodetic Applications, deGruyter
- Lawrence, A., 1998: Modern Inertial Technology, Springer, Mechanical Engineering Series
- LaCoste, L. J. B., 1967: Measurement of Gravity at Sea and in the Air, Reviews of Geophysics, Vol.5, No.4, 477 - 526
- LaCoste, L. J. B., Clarkson, N. and Hamilton, G., 1967: LaCoste & Romberg stabilized platform shipboard gravity meter, Geophysics, 32, 99 – 109
- LaCoste, L. J. B., 1973: Cross correlation method for evaluating and correcting shipboard gravity data, Geophysics, Vol. 38, No. 4, 701 - 709
- LaCoste, L. J. B., 1988: The zero-length spring gravity meter, Geophysics, 7, 20 – 21
- Marchenko, A. N., Barthelmes, F., Meyer, U. and Schwintzer, P., 2001: Regional Geoid Determination: An Application to Airborne Gravity Data in the Skagerrak, Scientific Technical Report STR01/07, GeoForschungsZentrum Potsdam
- Peters, M. F. and Brozena, J. M., 1988: Constraint for adjustment of potential field surveys, Geophysics, Vol. 53, No. 12, 1601 - 1604
- Schwarz, K.-P., Lee, Z., 1996: An Introduction to Airborne Gravimetry and its boundary value problem, IAG International Summer School, Como, Italy, May 26<sup>th</sup> – June 7<sup>th</sup>

SPIE Proceedings, Vol. 2837, Fiber Optic Gyros: 20<sup>th</sup> Anniversary Conference, Denver, Colorado, August 1996

Swain, C. J., 1996: Horizontal acceleration corrections in airborne gravimetry, *Geophysics*, Vol. 61, No. 1, 273 - 276

Titterton, D.H. and J.L. Weston, J. L., 1997: Strapdown inertial navigation technology, Peter Peregrinus Ltd.

Valliant, H. D., 1992: LaCoste & Romberg Air/Sea Meters: An Overview, *CRC Handbook of Geophysical Exploration at Sea*, 2<sup>nd</sup> Edition, Hydrocarbons, CRC Press

Van der Marel, H., 1998: Virtual GPS Reference Stations in the Netherlands, *Proceedings of ION GPS 98*, Nashville, 45-58

Xu, G., Schwintzer, P. and Reigber, C., 1998: KSG-Soft (Kinematic/Static GPS Software), Scientific Technical Report STR98/19, GeoForschungsZentrum Potsdam

### **13 Acknowledgements**

We would like to thank the BGI, DGFI and GGA for the ground-truth data necessary for evaluating the airborne measurements. Many thanks to the pilots and technicians who helped us during the installations on the Cessna and the survey and Ron Hackney who corrected large parts of this report for the sake of the English language.